

N70 32868

NASA CR-86395

ASE-2446

AN APPARATUS TO STUDY COLLISIONS OF IONIZED AND NEUTRAL PARTICLES WITH GASES AT METEORIC VELOCITIES

BY RODERICK D. SWIFT

JUNE 1970

CASE FILE
COPY

PREPARED UNDER CONTRACT NO. NAS 12-143 BY



AMERICAN SCIENCE AND ENGINEERING
11 CARLETON STREET CAMBRIDGE, MASSACHUSETTS 02142

ELECTRONIC RESEARCH CENTER
NATIONAL AERONAUTICS AND SPACE ADMINISTRATION

Dr. Martin S. Longmire
Technical Monitor
NAS 12-143
Electronics Research Center
Cambridge, Massachusetts 02139

Requests for copies of this report should be referred to:
NASA Scientific and Technical Information Facility
P.O. Box 33, College Park, Maryland 20740

AN APPARATUS TO STUDY COLLISIONS OF
IONIZED AND NEUTRAL PARTICLES WITH
GASES AT METEORIC VELOCITIES

By Roderick D. Swift

June 1970

Prepared under Contract No. NAS 12-143 by
AMERICAN SCIENCE AND ENGINEERING, INC.
11 Carleton Street
Cambridge, Massachusetts 02142

Electronic Research Center
NATIONAL AERONAUTICS AND SPACE ADMINISTRATION

TABLE OF CONTENTS

| | Page |
|---|------|
| SUMMARY | 1 |
| 1.0 Introduction | 3 |
| 2.0 Apparatus | 6 |
| 2.1 General Support Apparatus | 9 |
| 2.1.1 Vacuum Support Apparatus | 9 |
| 2.1.2 Power Distribution | 10 |
| 2.1.3 Water Distribution | 10 |
| 2.1.4 Gas Handling System | 10 |
| 2.2 Ion Beam Formation and Control | 11 |
| 2.2.1 Ion Source | 11 |
| 2.2.2 Extraction and Focusing Lens | 15 |
| 2.2.3 Sector-Magnet Analyzer | 18 |
| 2.2.4 Retarding Lens | 26 |
| 2.2.5 Control Electronics | 27 |
| 2.2.6 Operational Data | 29 |
| 2.3 Charge Exchange Production of Neutral Beams | 34 |
| 2.3.1 CEX Chamber | 34 |
| 2.3.2 Computation of Neutral Beam Intensity | 37 |
| 2.3.3 Operational Data | 39 |
| 2.4 Measurement of Beam Intensities | 41 |
| 2.4.1 Ion Beams | 41 |
| 2.4.2 Neutral Beams | 42 |
| 2.5 Interaction Regions | 46 |
| 2.5.1 Determination of Slit Sizes | 47 |
| 2.5.2 Second Assembly | 51 |
| 2.5.3 Target gas thickness | 54 |
| 2.6 First Optical/Calibration System | 55 |
| 2.6.1 Fore-Optics | 55 |
| 2.6.2 Monochromator | 58 |
| 2.6.3 Calibration System | 59 |
| 2.7 Second Optical/Calibration System | 68 |
| 2.7.1 Fore-Optics | 68 |

| | | |
|-----|---|------|
| 2.0 | <u>Apparatus (Continued)</u> | Page |
| | 2.7.2 Monochromator | 71 |
| | 2.7.3 Calibration System | 71 |
| 2.8 | Photon Counting | 72 |
| | 2.8.1 Detector | 72 |
| | 2.8.2 Electronic Processing | 73 |
| 2.9 | Modulation and Synchronous Detection | 76 |
| | 2.9.1 Boxcar Integrator | 78 |
| | 2.9.2 Logic Control Unit | 78 |
| | 2.9.3 Beam Chopper | 81 |
| 3.0 | Procedures and Analysis | 85 |
| 3.1 | Operational Procedures | 85 |
| | 3.1.1 Obtain Ion Source Plasma | 85 |
| | 3.1.2 Obtain an Ion Beam at the Faraday Cup | 86 |
| | 3.1.3 Obtain a Neutral Beam | 87 |
| | 3.1.4 Prepare the Counting System | 88 |
| | 3.1.5 Prepare Interaction Region | 88 |
| | 3.1.6 Prepare the Monochromator | 88 |
| | 3.1.7 Record the Necessary Data | 89 |
| | 3.1.8 Calibrate | 89 |
| 3.2 | Evaluation of Cross-Sections | 90 |
| | 3.2.1 Required Data | 90 |
| | 3.2.2 Computations | 91 |
| 4.0 | Experiments | 97 |
| 4.1 | $\text{Fe}^+ + \text{Gas Target Experiments}$ | 97 |
| 4.2 | $\text{Ar}^+ + \text{Ar Experiments}$ | 98 |
| 4.3 | $\text{He}^+ + \text{Ar Experiments}$ | 100 |
| 5.0 | $\text{N}_2^+ + \text{Ca Collisions}$ | 101 |
| | REFERENCES | 105 |

| | |
|--|------|
| <u>TABLE OF CONTENTS (Continued)</u> | Page |
| APPENDIX A: Drawing List | 109 |
| APPENDIX B: Current-Voltage Transducer | 121 |
| APPENDIX C: Logic Control Unit | 123 |
| APPENDIX D: High Voltage Chopper | 127 |
| NEW TECHNOLOGY APPENDIX | 129 |

ILLUSTRATIONS

| <u>Figure</u> | | <u>Page</u> |
|---------------|---|-------------|
| 1 | Atomic Beam Apparatus Schematic Diagram | 8 |
| 2 | Ion Beam Formation and Control | 12 |
| 3 | Plasma Chamber Assembly | 14 |
| 4 | Focusing Calculation Geometry | 20 |
| 5 | Magnetic Analyzer Geometry | 23 |
| 6 | Focusing Conditions for 3" Sector Magnet | 24 |
| 7 | Geometry for Mass Resolution Calculation | 28 |
| 8 | Retarding Lens Assembly and Potential Distribution | 30 |
| 9 | Voltage Divider Chain | 31 |
| 10 | Charge-Exchange Chamber Assembly | 35 |
| 11 | Geometry for Slit Calculations | 48 |
| 12 | 2nd Interaction Region/Detector Assembly | 53 |
| 13 | First Optical/Calibration System | 57 |
| 14 | Calibration Lamp Output | 60 |
| 15 | Object Distance vs Wavelength | 62 |
| 16 | Square of Magnification vs Wavelength | 63 |
| 17 | Two-Lens Transmission Function | 66 |
| 18 | Mirror Reflectance Measurements | 67 |
| 19 | Two-Mirror Reflectance Function | 69 |
| 20 | 2nd Optical/Calibration System | 70 |
| 21 | Detector Electronics Block Diagram | 77 |
| 22 | Timing Logic | 79 |
| 23 | High Voltage Modulator | 82 |
| 24 | $\text{Ar}^+ + \text{Ar}$ Cross-Sections, 4806 Å ⁰ | 99 |
| 25 | $\text{N}_2^+ + \text{Ca}$ Crossed-Beam Experiment | 103 |

TABLES

| | | |
|------------|-------------------------------|---------|
| TABLE I: | Typical Beam Performance Data | Page 33 |
| TABLE II: | Neutral Beam Measurements | Page 40 |
| TABLE III: | Bolometer Specifications | Page 45 |
| TABLE IV: | Slit Geometry | Page 52 |

AN APPARATUS TO STUDY COLLISIONS
OF IONIZED AND NEUTRAL PARTICLES
WITH GASES AT METEORIC VELOCITIES

By Roderick D. Swift

American Science and Engineering, Inc.
Cambridge, Massachusetts

SUMMARY

The study of meteor composition and the physics of meteor flight through the upper atmosphere depends greatly on proper interpretation of observed meteor spectra and ionization trails, both of which may be analyzed for various portions of the meteor path. Detailed quantitative analysis requires knowledge of the pertinent collisions, excitation and ionization cross-sections over the energy range corresponding to meteoric velocities. Such measurements are best made under controlled laboratory conditions. Accurate results could be applied, not only to meteor flight, but to the theory of atomic and molecular interactions as well.

In this report we describe an apparatus built to measure the spectra and the absolute emission cross-sections for light produced in particle collisions at meteoric Velocities. The term "emission" cross-section is used because the observed radiation may be the result of a cascade process as well as direct excitation to the parent level. Both ion-neutral and neutral-neutral collisions can be studied, and the calibrated spectral range is 2500 Å to 8000 Å. Detailed descriptions of the apparatus are given.

In order to check the performance of the apparatus, a number of experiments were done. These included spectral measurements, from which

relative cross-sections may be deduced, for Fe^+ ions impinging on gas targets (N_2 , O_2 , air and Ar). Spectra and cross-sections were also measured for $\text{Ar}^+ + \text{Ar}$ in order to compare results with those published by other research groups. The energy dependence of the cross-sections for emission of the 4610 Å and 4765 Å lines of Ar^+ during $\text{He}^+ + \text{Ar}$ collisions was studied in detail from threshold to 2000 eV ion energy. Finally, a beam of neutral N_2 at 900 eV was produced by a charge-exchange process and its intensity measured. The results of some of the above experiments have been published, and references are given. Computational procedures for cross-section measurements are also described.

1.0 INTRODUCTION

The visible radiation observed when a meteor penetrates the atmosphere consists almost entirely of atomic and molecular spectra, and is apparently produced at some separation from the meteor's surface. The conclusion is that the mechanisms principally responsible for the observed light and ionization trails are various types of collisions between atmospheric gases and particles either evaporated or rebounding from the surface. Depending on the meteor speed (10 - 70 km/sec) and the particle mass, the interaction energies lie in an approximate range 10 eV to 2000 eV. In order to evaluate the relative importance of the various collision processes, it is necessary to know the pertinent cross-sections over the above energy range. Laboratory measurements of these cross-sections would not only enhance our knowledge of meteor dynamics, through proper interpretation of the energy transfer processes responsible to the observed light and ionization, but would also add to our knowledge of the physics of atomic and molecular interactions.

The first radiations seen from a meteor upon entering the earth's atmosphere, while it is still in the regime of free molecular flow, are those characteristic of air emission alone. It is suggested by Cook (Ref. 1) that the air molecules which rebound from the meteor strike the ambient molecules at high relative velocity and excite them. If this is the mechanism, then knowledge of the excitation cross-sections and accommodation coefficients for air molecules in the meteoric energy regime can allow the cross-sectional area of the meteor to be inferred from measurements of the early time spectra. Similarly, while the composition of the meteors can be deduced in general terms by a study of the spectrum of the characteristic

lines emitted by the various elements, excitation cross-sections for the important lines are required to fully understand the physics of meteor flight and to deduce the true composition from the spectral data.

Any laboratory facility intended to measure cross-sections pertinent to meteor dynamics should have the following properties: (1) It should be able to produce beams of both atmospheric and meteoric constituents in either ionic or neutral form. (2) Such beams should be adjustable in energy, with small energy spread, throughout the 10eV to 2000eV meteoric regime. (3) Known target gases must be provided and their pressure controlled. (4) It should be possible to measure the number of slow ions produced by charge-exchange during interactions. (5) Optical radiation produced during interactions should be detected over as broad a wave length range as possible, and the range should include the visible spectrum where most meteoric observations are made. (6) The radiation should be detected with a spectral resolution sufficient to isolate most of the strongest lines. (7) The beam intensity, target gas particle density, and reaction products should all be measureable in a quantitative way so that absolute cross-sections can be computed.

An apparatus built to satisfy the above requirements is described in detail in Section 2 of this report. Section 3 outlines the operational and computational procedures required to obtain values for cross-sections, and the results of several experiments are described briefly in Section 4. The final section gives preliminary design concepts for a collision chamber that would enable the vapors of meteoric materials to be used as the target. Laboratory notebooks produced under the subject contract will be provided with this report, as will copies of all construction drawings and wiring diagrams.

The author takes this opportunity to thank Dr. Lester Sodickson for preparing most of the original proposal for this work, Mr. Orr Shepherd for many helpful discussions on the design of optical and electronic systems, Mr. Kevin Hainsworth for the design and construction of the special electronics required for the apparatus, and the personnel of the AS&E machine shop for their excellent work in fabricating the mechanical assemblies.

2.0 APPARATUS

The principal tasks set forth in the Statement of Work of Contract NAS 12-143 are directed toward the design, construction and testing of a laboratory facility intended to perform measurements of cross-sections for collision processes characteristic of those that occur when a meteor enters the atmosphere. It is imperative that the Final Report include sufficiently detailed descriptions of the apparatus and its operation to permit its use by personnel unfamiliar with its construction. The main body of the Report is therefore contained in this Section.

Two main categories of experiments are to be performed: ion-neutral and neutral-neutral collisions. The useful energy range of the apparatus is approximately 10eV to 3000eV, slightly exceeding the range of energies characteristic of meteoric collisions. The apparatus is primarily intended to measure optical emission cross-sections, but it can also be used to measure cross-sections for charge transfer. Optical calibration facilities are included.

A schematic diagram of the apparatus is shown in Figure 1. It consists of four principal sub-systems, plus support equipment required for their operation. They are (1) facilities for ion beam formation and control, (2) a charge-exchange region to produce neutral beams, (3) a collision chamber where experiments are actually done and (4) an optical system to collect and measure the collision induced light. These sub-systems include the means to determine the necessary quantities: beam energy, beam intensity, collision gas pressure and temperature, light wave length, light intensity, light

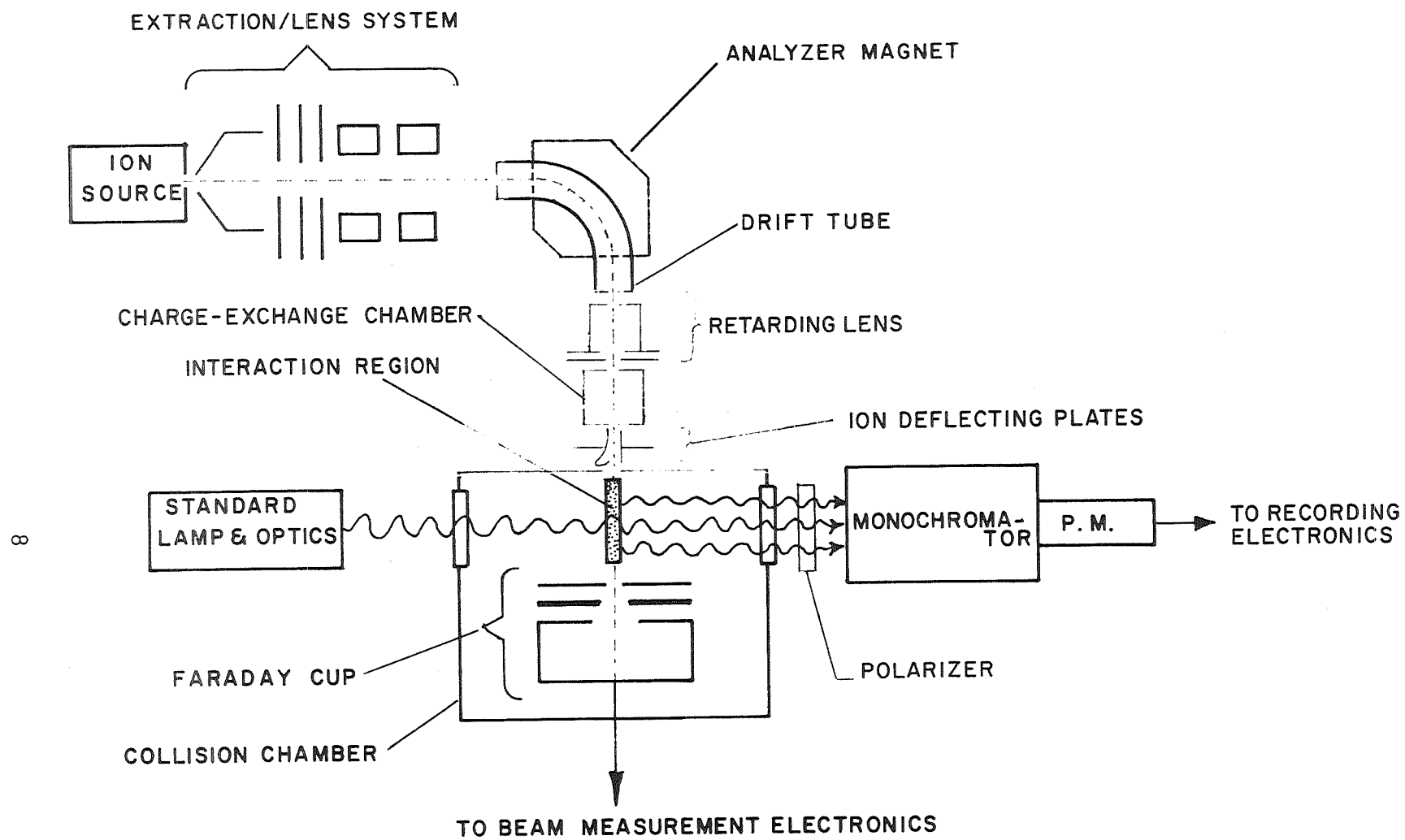


Figure 1. Atomic Beam Apparatus Schematic Diagram

polarization, and net quantum efficiency. Photon counting methods are used to measure the collision light, and standard lock-in detection methods are employed to record spectra.

A set of construction prints is provided with this report. It thoroughly covers the mechanical details of the apparatus, which will not be repeated here. A Drawing List is given in Appendix A. Description of the various components of the apparatus follow.

2.1 General Support Apparatus

This topic covers the support systems - vacuum, power, water and gas handling - that provide the environment and services necessary to operate the basic experimental equipment. Except for the gas handling facility, which is separate, the support systems are an integral part of a 4' x 5' movable table upon which the fundamental parts of the apparatus are mounted.

2.1.1 Vacuum system. - The source chamber, containing the ion source, extraction and focusing lens, and drift tube, is pumped by a 4" oil diffusion pump. The target chamber, which has a higher gas load during experiments, is pumped by a 6" oil diffusion pump. Both pumps utilize water baffled zeolite traps above their inputs and are backed by the same mechanical pump. The fore-line/roughing line also contains a zeolite trap to prevent back-streaming of mechanical pump oil vapors. Both diffusion pumps may be valved off when the system is vented.

The control panel for the pumping system contains a safety interlock that protects the diffusion pumps and ion source in case of water, power or vacuum failure.

2.1.2 Power distribution. - The electrical power input consists of a 120/208 volt, 3 phase line rated at 60 amperes per phase. It is distributed through a 24-circuit breaker box. The distribution plan is as follows:

Diffusion pumps, phase A, 3.0 KVA

Mechanical pumps, phase A, 1.5 KVA

Ion source (except oven), phase C, 7.0 KVA max*

Ion source oven, phase B, 2.0 KVA max -- reserved

Zeolite trap heaters, phase C, 3.0 KVA*

System bakeout heaters, phase C, 5.0 KVA* -- reserved

(assuming 1000 sq. in. at 5 W/in²)

Analyzer magnet, 3 phase, 1.8 KVA max

Charge-exchange oven, phase B, 2.0 KVA (estimated max) - reserved

Utility outputs (electronics), phase B, 3.0 KVA (estimated max)

A power distribution plan is given on Drawing SK-120-3004.

2.1.3 Water distribution. - The water distribution plan is shown in Drawing SK-120-3003. Note that the ion source cooling jacket uses a heat exchanger filled with distilled water and a deionizer. This is to inhibit corrosion and formation of mineral deposits in the cooling jacket, which would prevent its disassembly for cleaning. The pump quick-cooling circuit is tied into the vacuum safety interlock.

2.1.4 Gas handling system. - A gas handling system, including an auxiliary vacuum system, was built to control the gas flow to the ion source, collision chamber and charge exchange chamber. It is shown schematically in

* Note that no two of these items would be drawing power at the same time.

Drawing SK-120-3023. The operation of the system is evident from the drawing. A McLeod gauge is provided to calibrate the capacitance manometer used to measure the collision gas and charge-exchange gas pressures. The McLeod gauge may also be used to measure the pressure in the auxiliary vacuum system.

2.2 Ion Beam Formation and Control

The procedure used to obtain a beam of ions of the desired species, traveling at meteoric velocities, may be considered as four separate processes: (1) formation of a plasma of partially ionized gas from which ions may be electrostatically extracted, (2) extraction and focusing of the ions to form a well-defined, controllable beam, (3) selection of ions of the desired species, and (4) adjustment to the desired energy. The equipment needed to perform the above functions, and operational data which indicate the degree of success, are the subjects of this topic. Figure 2 schematically illustrates the ion beam formation and control apparatus.

2.2.1 Ion source. - The ion source is a commercially available source (Danfysik Model 910) of the so-called Danish or Nielsen type, selected because of its ability to be operated with low vapor-pressure materials. It is adequately described in the published literature (Refs. 2 to 4), so only a brief description will be given in this report.

The heart of the ion source is a cylindrical cavity in which a plasma of partially ionized gas of the desired beam material, or a compound containing it, is formed by electron bombardment. The charged particles are magnetically contained by an axial magnetic field; the electrons are concentrated

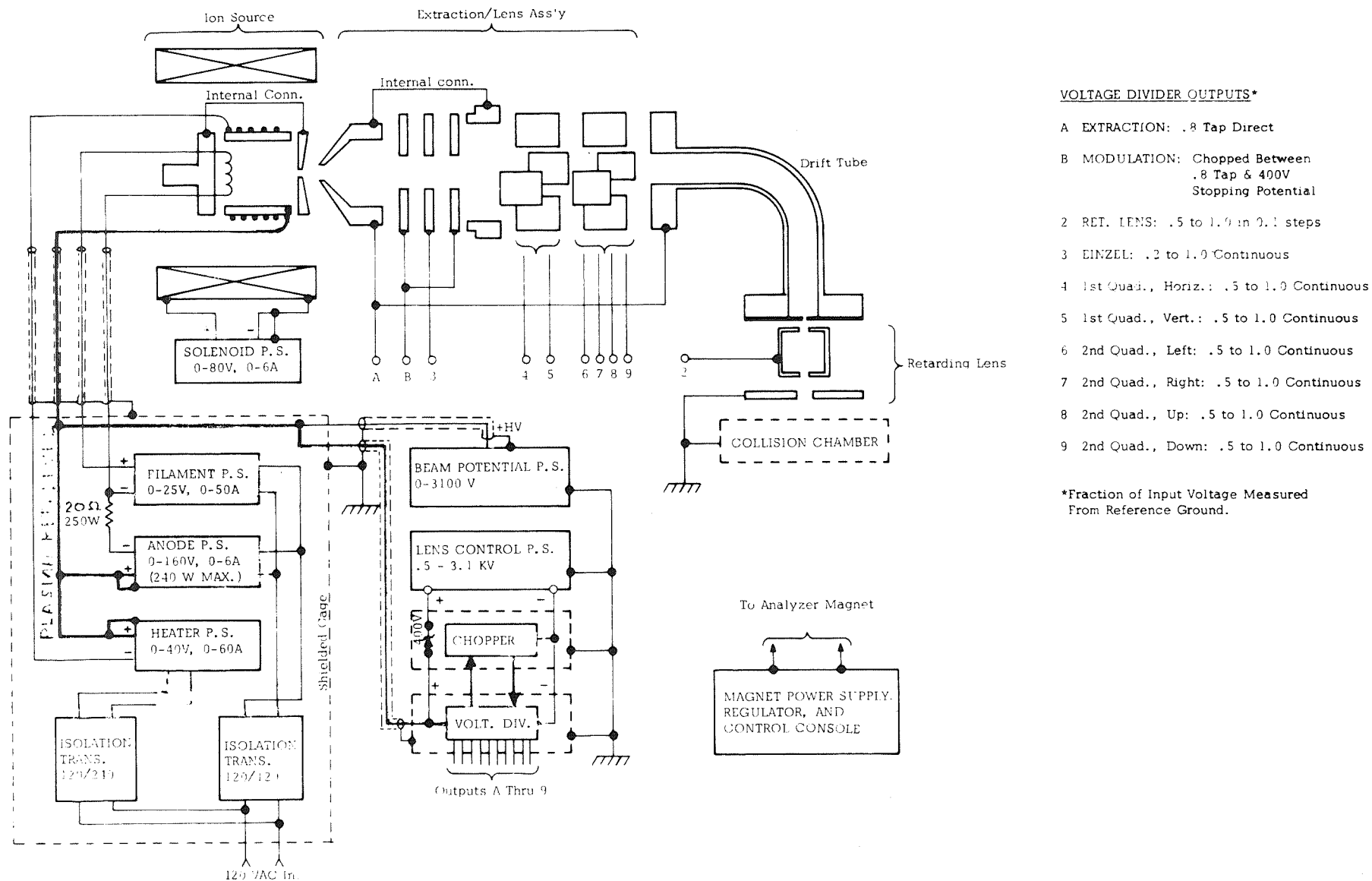


Figure 2. Ion Beam Formation And Control

near the center of the cavity by maintaining both end caps at cathode potential while the cylindrical wall acts as an anode. When proper conditions of magnetic field, electron emission, anode potential and pressure are achieved, a nearly self-sustaining plasma is created, from which an ion beam may be extracted.

The ion source, as originally obtained, was capable of producing temperatures to about 1200°C. Since pressures in the range of 10^{-4} to 10^{-3} torr are required to sustain a plasma, even higher temperatures must be attained to operate the ion source directly on the vapors of iron, nickel and silicon, all important meteoric constituents. In addition, the final ion energy depends on the potential difference between the grounded collision chamber and the plasma. Consequently, the plasma chamber was redesigned for operation at temperatures up to 1500°C and at potentials to -3kV relative to its grounded vacuum housing.

A cross-sectional view of the new plasma chamber is shown in Figure 3. The design minimizes thermal stresses, and all parts subjected to a high temperature environment are made from refractory materials: grade HP boron-nitride insulators, graphite or molybdenum electrodes, tungsten filaments, and molybdenum heater and radiation shields. The charge material may either be inserted in solid form (as shown), leaked in as a gas, or retained in a suitable crucible. The plasma is initiated and sustained by electron emission from the small filament, while extra power to control the temperature is provided by the heater coil. The heat shields substantially reduce the power required to obtain high temperatures. To run a Fe^+ beam, a total power of about 350 watts is required, of which about 200 watts are supplied by the

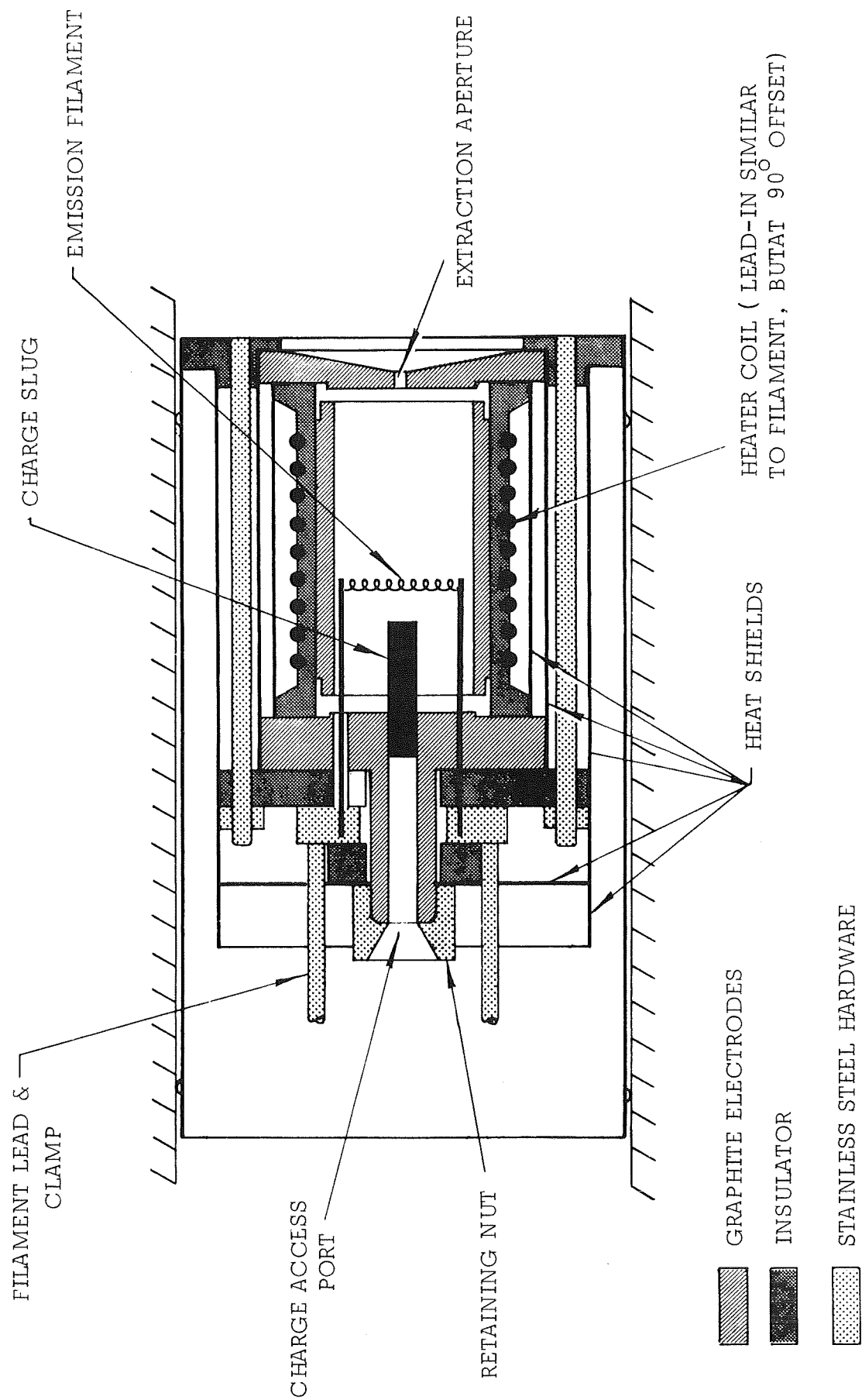


Figure 3. Plasma Chamber Assembly

heater, 150 by the filament.

The ion source is mounted on a bellows-sealed positioning platform that enables the plasma chamber axis to be properly aligned with the rest of the ion-optics system. It incorporates two, orthogonal, micrometer-drive mechanisms for transverse motion, and four jackscrews which are used to adjust the extraction gap.

2.2.2 Extraction and focusing lens. - The extraction electrode and lens assembly consists of three fundamental parts: an electrode to pull ions from the plasma, an einzel lens to form the extracted current into a parallel cylindrical beam, and a quadrupole lens pair to shape the beam and focus it onto the entrance slit of the magnetic analyzer.

The shape of the electrodes at the extraction gap is a geometry frequently shown in the literature (Refs. 3, 5), and represents an empirical deviation from the electrode shape used in the so-called Pierce gun (Ref. 6). Pierce's calculations determine the form of the equipotential surfaces required to form a parallel beam of electrons (or other charged particles) from a planar cathode. In particular, the zero potential electrode (i.e., the cathode electrode, whose aperture determines the cross-section of the parallel beam) meets the plane of the emitter at an angle of 67.5° , and more distant equipotential surfaces approach an angle of 90° at the edge of the beam. One of the latter, depending on its distance from the cathode, determines the shape of the accelerating (extration) electrode. The shape of the emitting boundary of the plasma is difficult to define, however, and is not likely to be planar (Ref. 7), so Pierce's formulation is not strictly valid and the empirical approach is used.

In order to form a parallel beam at the input of the quadrupole lens (see below), a three-aperture einzel lens was built with the extraction electrode aperture at its focus. The equations used for the design of the lens were taken from Pierce:

$$\frac{1}{f} = \frac{3}{8L} \left(\frac{V_2}{V_1} - 1 \right) \left[4 - \left(\frac{V_2}{V_1} \right)^{1/2} - 3 \left(\frac{V_1}{V_2} \right)^{1/2} \right] \quad (1)$$

$$D = \frac{4L}{\left[3 - \left(\frac{V_2}{V_1} \right)^{1/2} \right] \left[\left(\frac{V_2}{V_1} \right)^{1/2} + 1 \right]} - L \quad (2)$$

where

L is the space between the elements

f is the focal length (from the lens center)

D is the distance of the principal plane from the center

V_1 is the potential of the outer elements

V_2 is the potential of the center element

Plots of L/f and D/L are given in Reference 6. Since the equations leave a great deal of choice open for the particular application, the following conditions were applied: (1) The beam cross-section for input into the quadrupole lens should be about $\frac{1}{2}$ " diameter. This was chosen as the aperture size. (2) While the aperture diameter does not enter into Pierce's formulation, it was felt that the plate separation L should be somewhat greater than the diameter, so $L=3/4$ " was chosen. (3) The focal length

should be short enough so that the lens acceptance angle is reasonably large. (4) The total length of the lens, from extraction electrode to quadrupole focus, should be about 9" to allow room for pumping the source chamber through the lens housing. Conditions (3) and (4) were used to select a compromise value for the voltage ratio V_2/V_1 , which determines the focal length for a given geometry. The values chosen were:

$$V_2/V_1 \approx 2.5$$

$$f \approx 2.625"$$

Fine adjustment can be made by changing V_2 , the voltage on the middle element of the einzel lens.

For maximum transmission through a sector type magnetic analyzer, the ion beam should be strongly converging in the plane perpendicular to the field, reaching a crossover at the analyzer entrance slit, and slightly converging in the plane parallel to the field to compensate for the fringing fields. This focusing situation can be achieved by the use of an electrostatic quadrupole pair. The first set of electrodes causes convergence in one plane and divergence in the other, while the second set interchanges the planes and is less strongly focusing. Just such a lens is described by Giese (Ref. 8). His design was directly adaptable to the present effort using his published dimensions. The focusing properties can be adjusted by varying the potentials, and a small amount of beam steering introduced by using slightly different potentials on opposite electrodes of each pair.

The additional provision is made for rotation of the lens about its axis. This enables the ribbon shaped quadrupole output to be precisely aligned with the mass analyzer slits. It has been found to be an important

adjustment for best beam intensity.

A lens system very similar to that described here was previously used by Kistemaker, et al. (Ref. 9).

2.2.3 Sector-magnet analyzer. - An ion source of the type selected for this apparatus produces electron energies well in excess of the second ionization potentials of the charge materials. For that reason, the ion beam can be expected to have a large number of multiply charged ions which it is desirable to eliminate. It is also desirable, of course, to eliminate contaminants of different species. This is particularly important when very high temperatures or buffer gases are used in the ion source. A magnetic analyzer of the sector type most easily accomplishes these tasks.

Let us briefly consider the operating principles of sector magnet analyzers. For a detailed treatment, refer to one of the standard texts on charged particle dynamics (e.g., Ref. 10).

A charged particle moving perpendicular to a magnetic field undergoes a displacing force of magnitude

$$F = \frac{q}{c} e v B = \frac{Mv^2}{R} \quad (3)$$

where q is the number of charges carried. If we replaced the velocity v by its non-relativistic equivalent

$$v = \sqrt{\frac{2E}{M}} \quad (4)$$

and write E in electron volts, with the necessary conversions of units, we get

$$R = 4.61 \sqrt{\frac{MV}{q B^2}} \quad (5)$$

where

R is the radius of curvature in cm,

q is the number of elementary charges carried,

B is the magnetic field in kilogauss

M is the particle mass in AMU,

V is accelerating voltage in kilovolts.

Consequently, for a given V and B , particles with a different ratio M/q will follow different trajectories. A sector magnet is therefore ideal to separate singly and multiply charged ions of the same species and to eliminate most impurity materials.

A simple geometric proof shows that particles of equal M/q emerging from a slit with a small angular spread will be refocused by a sector magnet, the focus lying on the extended line between the emitting slit and the center of curvature. We consider the case where the beam axis enters and leaves the field at right angles to the field boundary; fringing fields are neglected. Figure 4 illustrates the geometry. Referring to part (a) of the drawing, we see that T_0 enters the field at H , follows a circular arc C of radius R , and emerges at J where it continues in the direction z . Now consider another ray T' , parallel to T_0 but displaced by a small distance HH' . The center of curvature for this ray is displaced to K' , however, so it emerges from the magnetic field sector (shaded portion) at J' after following a slightly shorter (for the case illustrated) circular arc C of radius R .

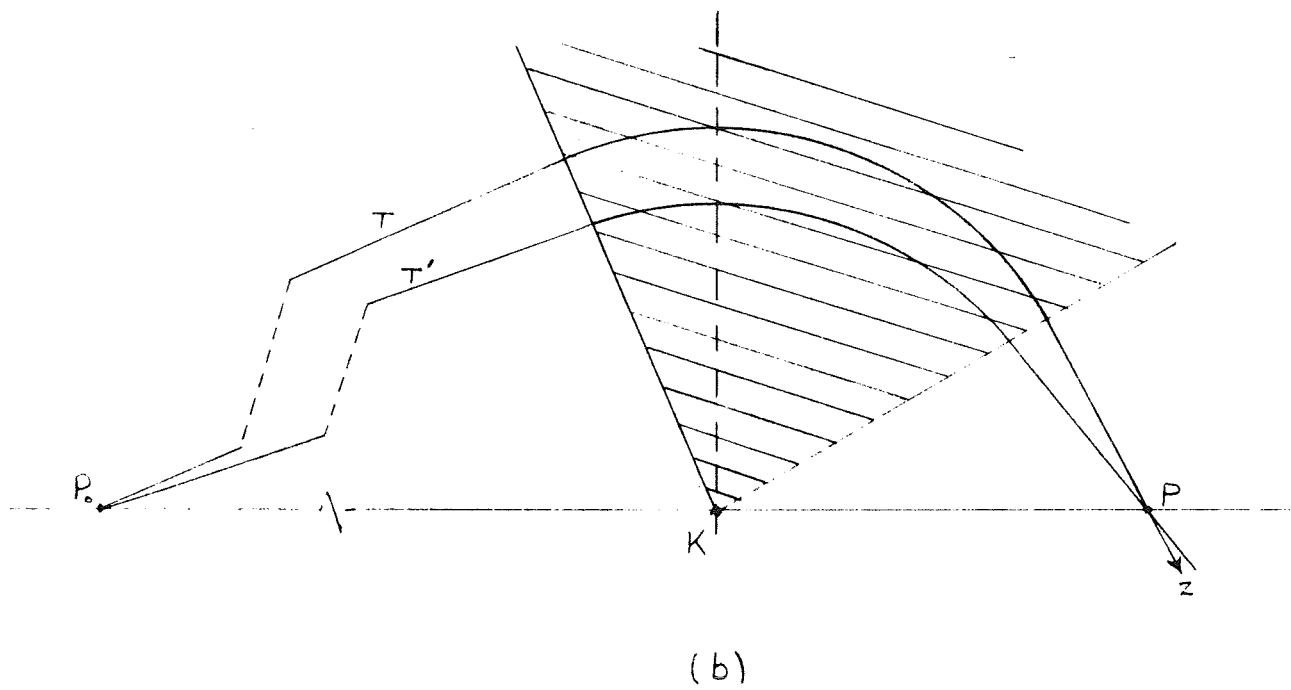
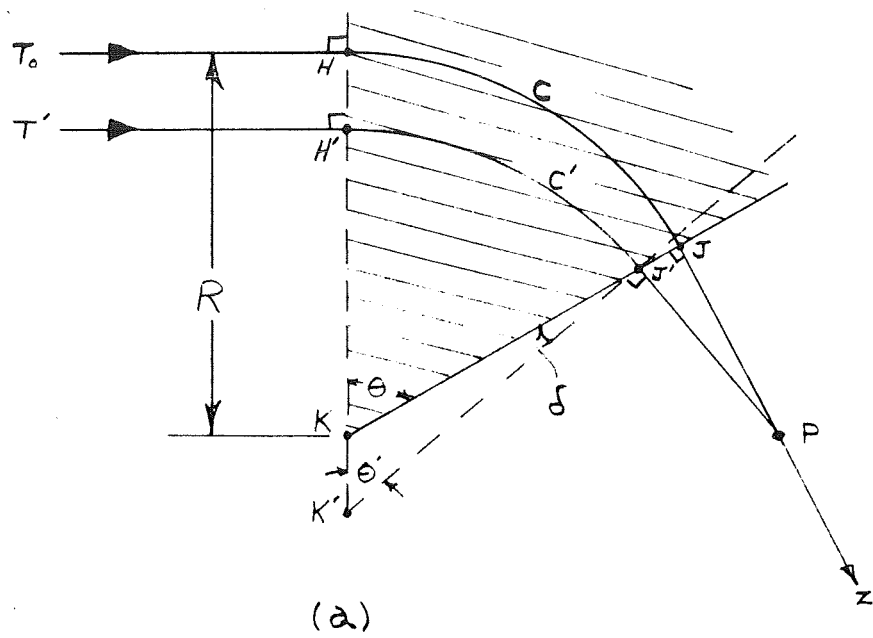


Figure 4. Focusing Calculation Geometry

Ray T' therefore approaches ray T_o at a small angle δ , and eventually the two intersect at some image point P , which is characteristic of a focusing system. We wish to determine the location of P and show that it is the same (to a small angle approximation) for all similar rays. Referring to the figure, we have

$$JJ' = JP \tan \delta \quad (6)$$

where

$$\delta = \angle JPJ' = \angle KJ'K = \theta - \theta'.$$

According to the restriction that HH' is small, $\theta \approx \theta'$ and δ is a small angle. Therefore $\tan \delta \approx \sin \delta$, and $JJ' \approx HH' \cos \theta$. Substituting, we have

$$HH' \cos \theta = JP \sin \delta \quad (7)$$

or

$$\frac{HH'}{\sin \delta} = \frac{JP}{\cos \theta} \quad (8)$$

Now consider the triangle $KJ'K$. From the law of sines, we have

$$\frac{K'J'}{\sin (180^\circ - \theta)} = \frac{KK'}{\sin \delta} \quad (9)$$

But $KK' = HH'$ and $KJ' = R$; therefore we have from equation (8):

$$\frac{R}{\sin (180^\circ - \theta)} = \frac{R}{\sin \theta} = \frac{JP}{\cos \theta} \quad (10)$$

or

$$\frac{R}{JP} = \tan \theta = \frac{KJ}{JP} \quad (11)$$

Since the angle $\angle KJP = 90^\circ$, equation (11) leads to the conclusion that P lies at the intersection of the optical axis (line Jz) and a line through the center of curvature K parallel to the incident rays, such that

$\angle JPK = \theta$. In addition, we see that this position is independent of any coordinates except those of the optical axis, so it is the same for all rays T.

If we now add another sector (fig. 4(b)), and apply the above arguments in reverse, we see that the rays again converge to a point P_0 , the object point, which is collinear with K and P. In the case shown, the two parts of the sector field are not equal and we have a condition of reduced image size (magnification < 1). Usually the sector is symmetrically oriented, giving $m = 1$. It may also be shown that the shortest path length from source slit to image occurs when they are symmetrically located. We note that this type sector is focusing only in the plane shown, and not in the vertical plane.

Space restrictions and the requirement of minimizing beam path length (to minimize $1/r^2$ losses) led to the choice of a 3" curvature, 90° sector magnet of the configuration shown in Figure 5. Focusing conditions for a 3" curvature magnet are given in Figure 6. The magnet is specified to provide at least 10 kilogauss with a $5/8$ " pole-gap spacing. The mechanical configuration was basically determined by the overall layout of the apparatus. The power supply provides up to 50 amps at 25 volts with .01% long-term regulation.

It is also of interest to compute the approximate mass resolution we would expect such a magnet to have. As in an optical spectrometer, this will depend on the image size, or slit width; we assume $l_{mm} = .04$ " slits. In order to be resolved, an adjacent mass image must be shifted at least

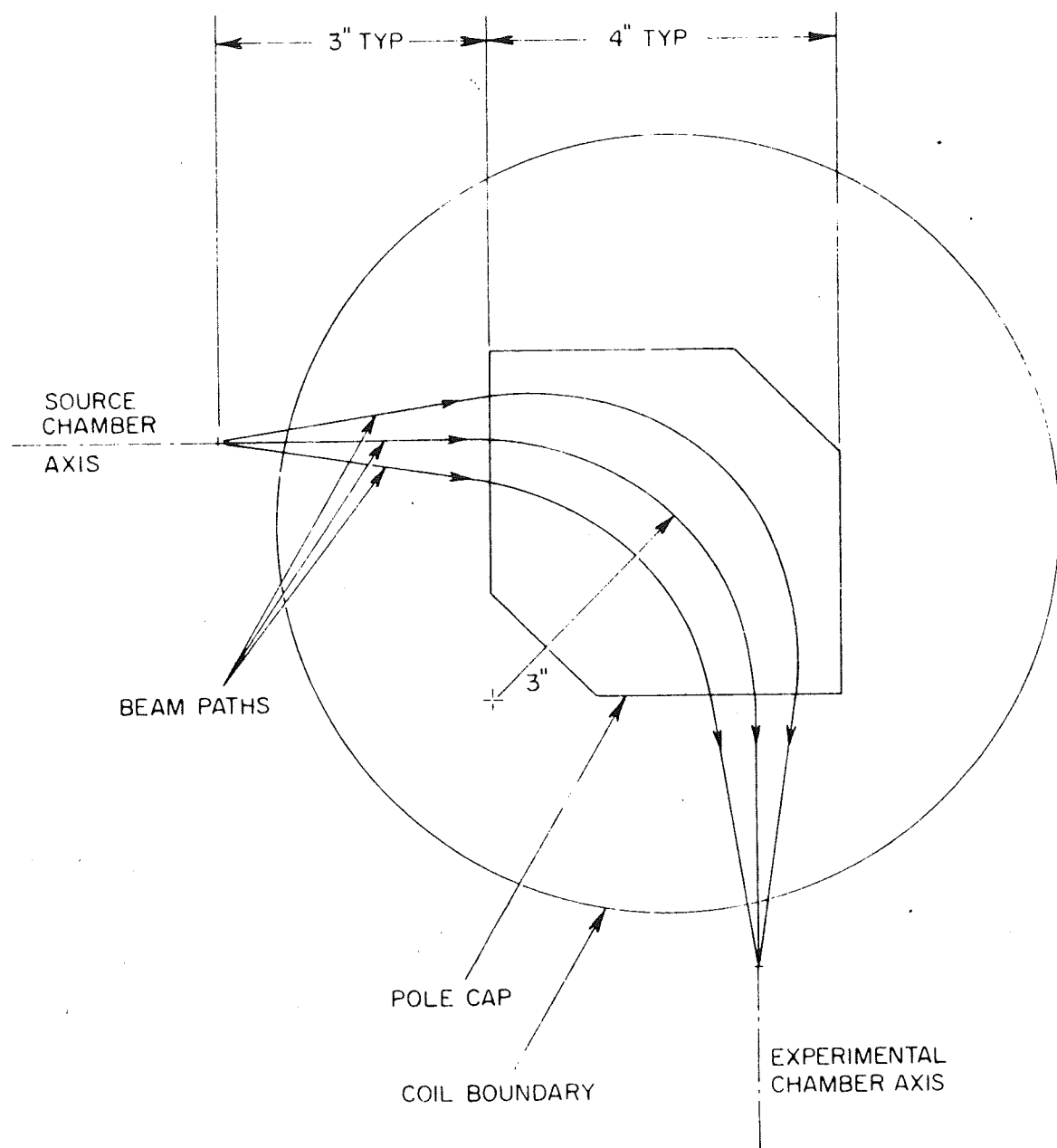


Figure 5. Magnetic Analyzer Geometry

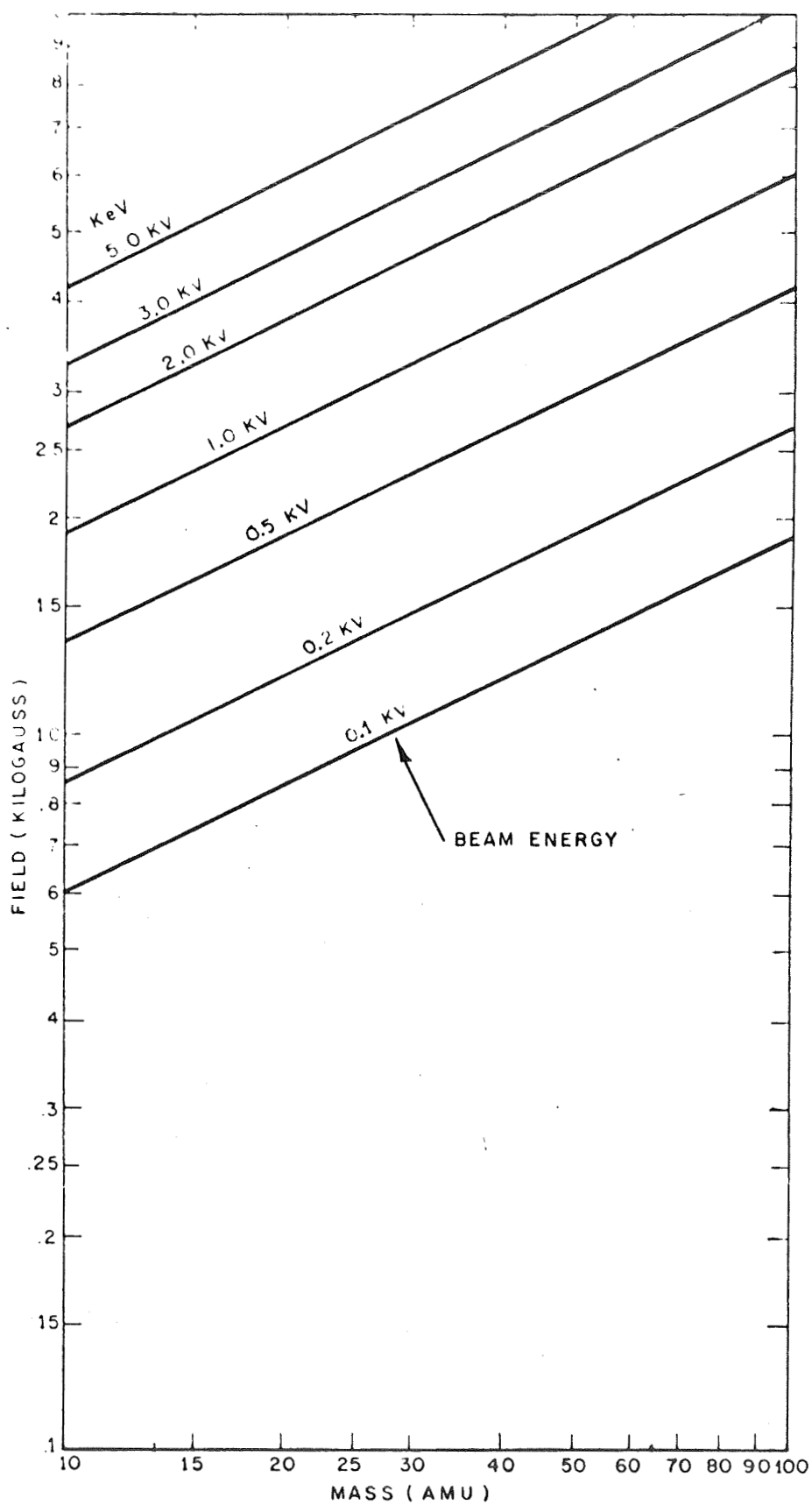


Figure 6. Focusing Conditions for 3" Sector Magnet

1 slit width in the plane of the slit. The displacement D of the mass depends on its change in radius of curvature, and according to the simple geometry of Figure 7 is shown to be approximately $2 \Delta R$. In order to be resolved, an adjacent mass image must be shifted at least 1 slit width in the plane of the slit; i.e., we require $D = 2 \Delta R = .04''$. Differentiating equation (5), we have (for singly charged particles, $q = 1$):

$$\frac{dR}{dM} = \frac{1}{2} \times 4.61 \sqrt{\frac{V}{B^2 M}} = \frac{R}{2M} . \quad (12)$$

Writing in terms of increments, we have

$$\frac{M}{\Delta M} = \frac{R}{2\Delta R} = \frac{R}{D} = \frac{3''}{.04''} = 75 . \quad (13)$$

The quantity $M/\Delta M$ is commonly called the mass resolution.

The magnet is mounted on a specially designed platform that enables it to be precisely located to provide optimum focusing conditions (in that way compensating for fringing field effects) and to be rolled back for access to the drift tube and vacuum housing. Magnetic shields (sandwiched Netic and Conetic sheets) are installed to reduce the range of fringing fields. They also create a physical barrier to prevent personnel from coming in contact with the drift-tube, which operates at a high voltage.

In order to provide an evacuated path for the beam through the magnet pole gap, a drift-tube was fabricated by electroforming copper on an aluminum mandrel, which was subsequently etched out. It is pumped through both end flanges, and has sight ports in line with both entrance and exit axes. An adjustable beam stop limits the acceptance angle of the analyzer to approximately 0.12 radians (0.06 radian half-angle). The drift-tube normally

operates at an elevated potential, so both flanges have teflon insulators, and teflon sheets prevent contact with the magnet pole pieces.

2.2.4 Retarding lens. - The final ion energy is determined by the net potential drop between the plasma in which the ions are formed and the grounded collision chamber. The potential distribution in a plasma discharge is such that the plasma boundary is within a few volts of the anode potential, the difference being called the "anode fall" (Refs. 11, 12). Positive ions extracted from the plasma may therefore be assumed to originate essentially at anode potential. Referring to Figure 2, we see that this is established by the Beam Potential Power Supply, the output of which is a common reference potential for all other ion source and lens voltages. This will be discussed more fully in a following sub-section.

The function of the retarding lens is to provide some means of control over the beam trajectory as it is decelerated between the exit apertures of the drift-tube, where it has the energy imparted to it by the extraction electrode, and the entrance to the grounded charge exchange or collision region. The geometry used is shown in Figure 8. Deceleration takes place in two stages: the first is between the drift-tube exit slit and the entrance of a field free cylinder, the second between the cylinder and an aperture plate at ground potential. The potential of the field-free region is set by one of the outputs of the voltage divider, also discussed later. It is adjusted for best focusing and collimation of the beam as measured by a Faraday collector in the collision region. The action of this retarding lens is very similar in principal to that described by Neff (Ref. 13) except that his field-free region was maintained at the final beam potential,

and served as the first element of an einzel-lens array for the beam focusing (see Figure 8).

2.2.5 Control electronics. - The electronic requirements of the ion source and ion optics system are primarily for power supplies, if we include in this category the voltage divider which provides adjustable bias voltages for the various lens elements. The relationship between the individual parts requires some explanation, however, if we are to understand the operation of the system as a whole. Reference to Figure 2 will be helpful.

We previously mentioned that the final ion energy is determined by the potential difference between the plasma and ground. The plasma potential, therefore, plays a critical role and is used as reference level relative to which all other ion source and lens voltages are established. (Actually, the anode potential is our reference, but this is nearly the plasma potential as we have noted - see 2.2.4). Thus, the extraction and analysis energy remains fixed, and the only lens element requiring substantial readjustment for different plasma potentials is the retarding lens cylinder itself.

Except for the analyzer magnet power supply, all the control electronics are mounted in an enclosed relay rack to which ac power is provided through a safety interlock. Power supplies for the ion source filament, heater, and anode-cathode potential are contained inside a plexiglass and wood box built into the rack. They receive their ac power through isolation transformers, and their cases are connected to the plasma reference potential. Parts of the beam chopper (to be discussed in Section 2.9), lens control power supply and voltage divider also float at voltages to ± 3100 V relative to earth

ASSUMPTION: $\Delta R \ll R$

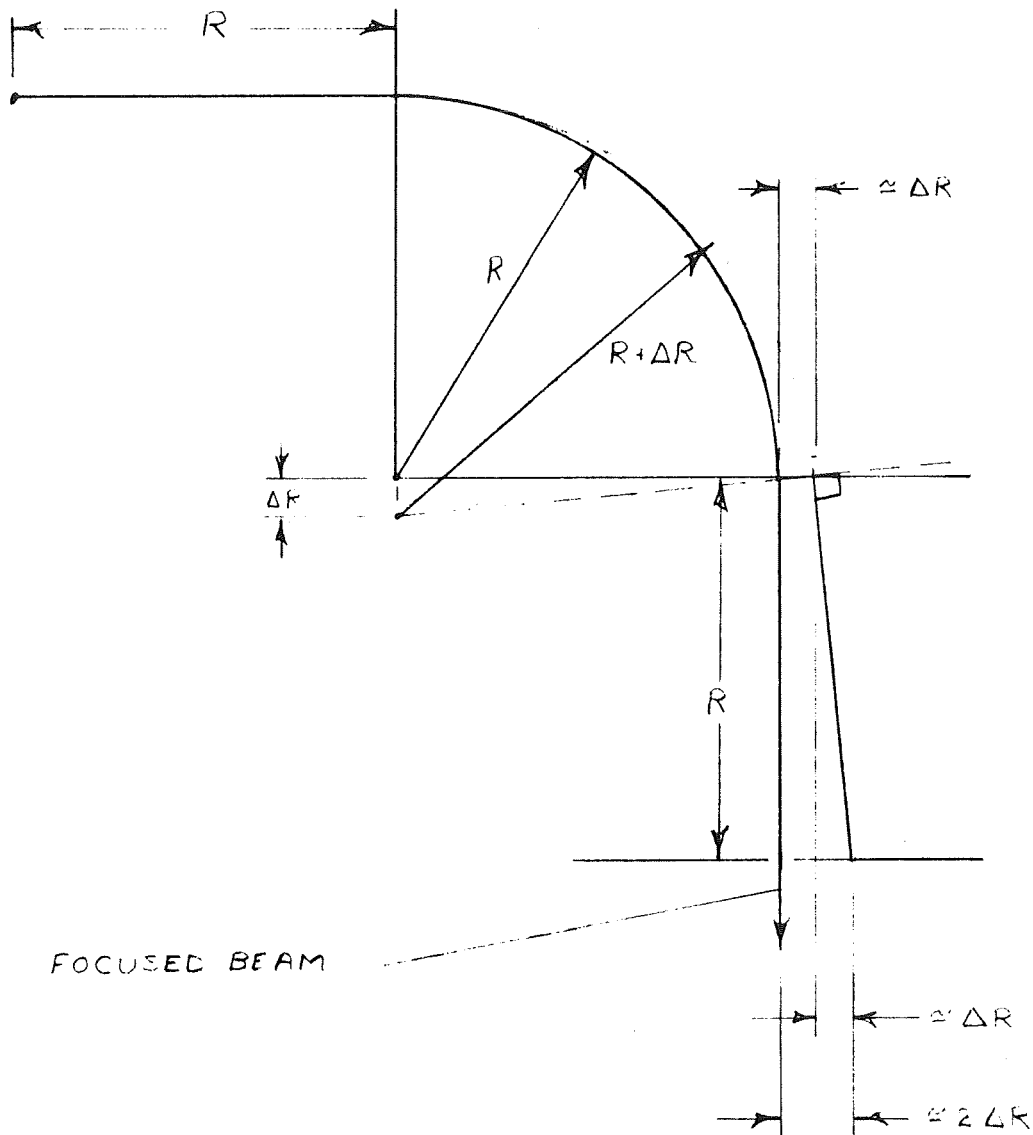


Figure 7. Geometry for Mass. Resolution Calculation

ground, but they are well insulated from their cases and are mounted directly on the front of the cabinet. The plasma potential is established by setting of a Fluke Model 405B, which can be set at any voltage from 0 V to +3100 V.

The voltage divider requires some further comment. It was desired to obtain the lens potentials from a single power supply by means of a voltage divider network. A ten-stage, transistorized Kelvin-Varley divider chain was designed and built expressly for this purpose by Northeast Scientific Corporation. Figure 9 illustrates the basic stage of the divider chain and indicates how the outputs are obtained. The advantage of a transistor voltage divider over a purely resistive one is that it can provide a number of independent outputs from a single, regulated chain, thus giving better stability with lower power dissipation. Unfortunately, despite the addition of protective circuits, this prototype unit was susceptible to damage by accidental high voltage transients and arcs. For this reason, the portion indicated by the left-hand bracket on Figure 9 was replaced by a chain of ten 7500 Ω resistors. Since that time, however, high voltage breakdown has been greatly reduced, and it may be worth trying the transistor chain again.

2.2.6 Operational data. - The operational tests and data for the ion beam formation and control portion of the apparatus are contained in the laboratory notebooks provided with this report, and were thoroughly discussed in Ref. 14. Only a brief review will be given here.

The basic parameters affecting the ion source and lens operation are

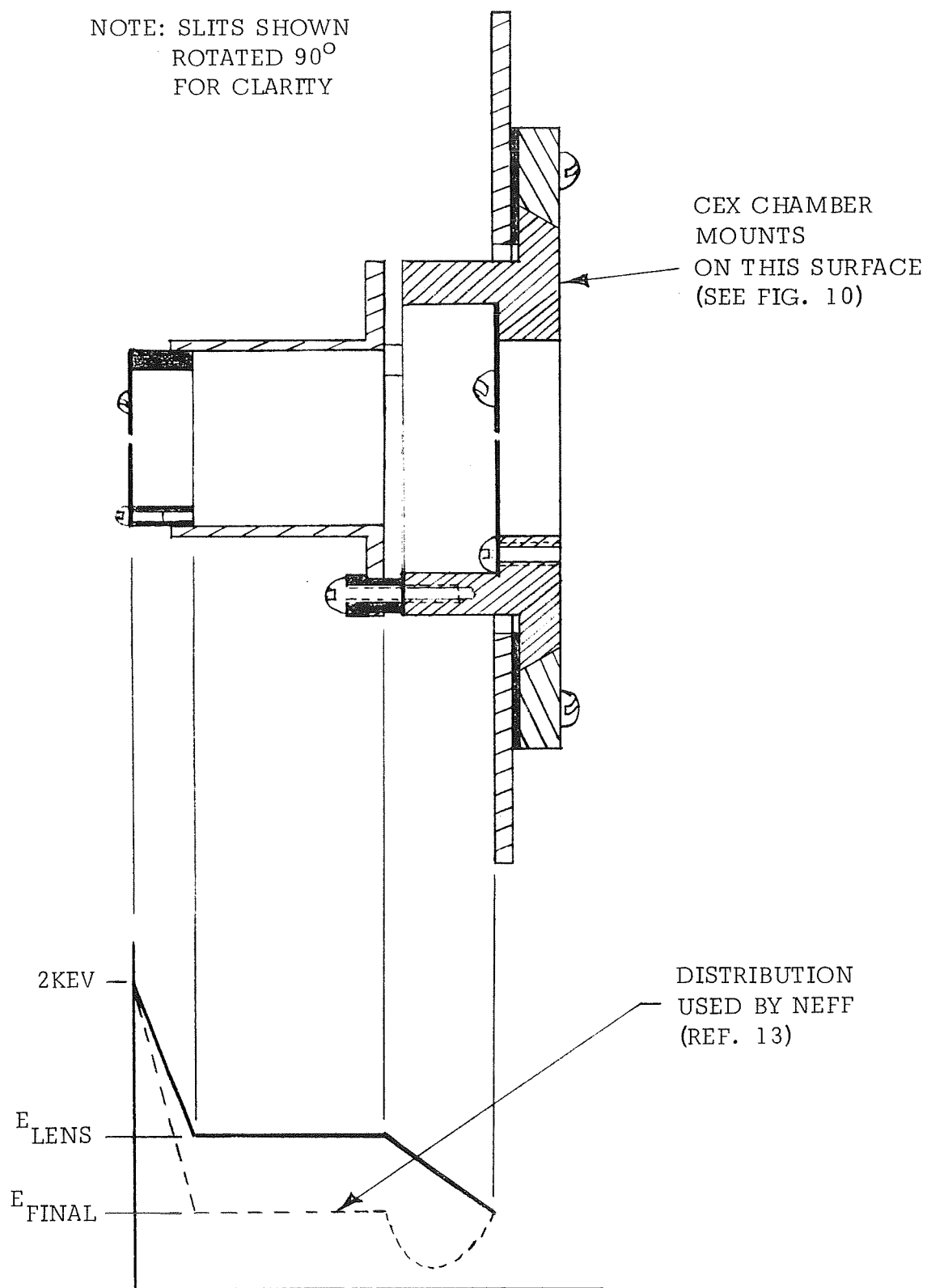
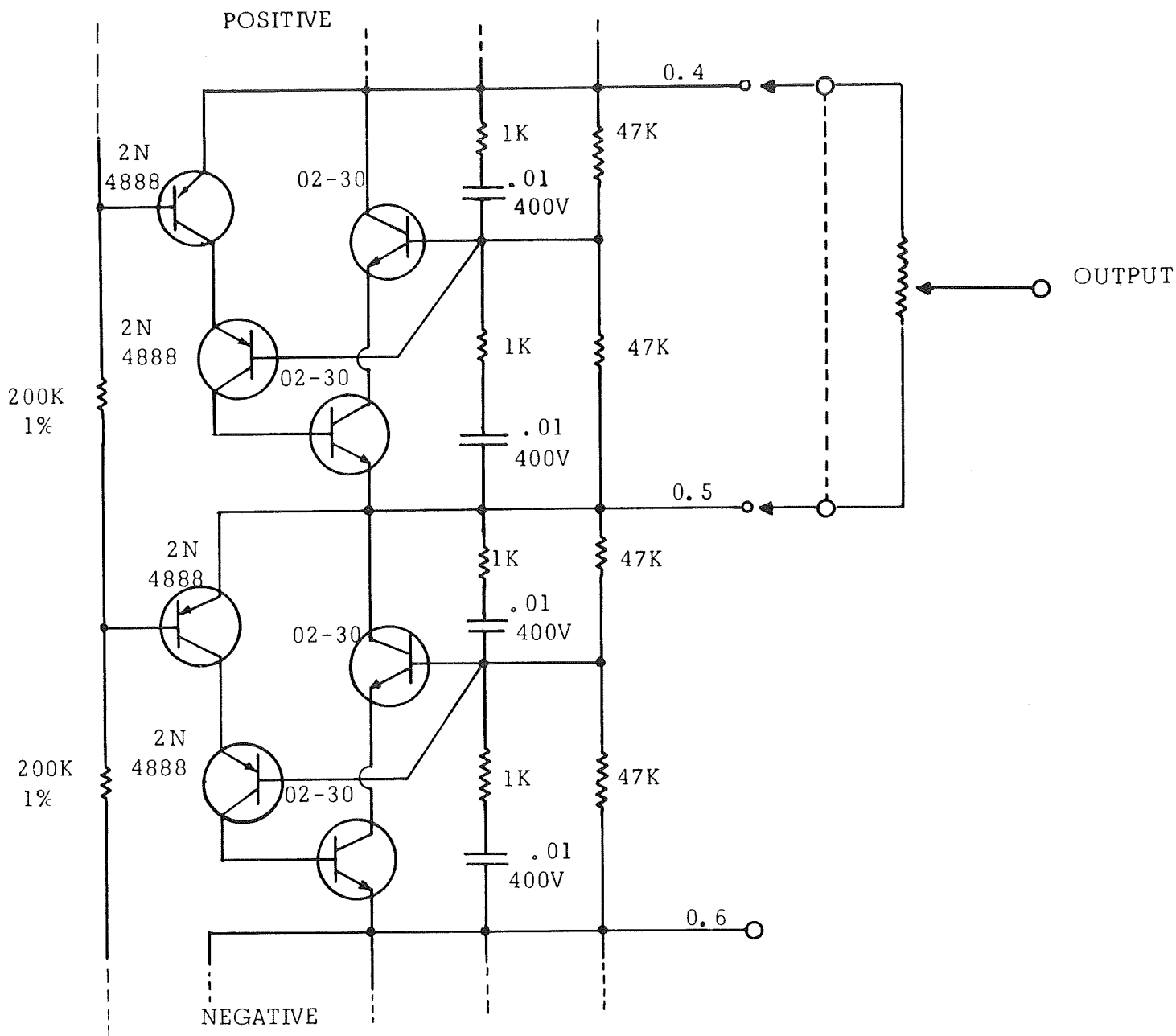


Figure 8. Retarding Lens Assembly and Potential Distribution.



Ten Stages to divide overall applied voltage into ten increments

Multi-position switch & fine-control potentiometer for each output.

Figure 9. Voltage Divider Chain

filament emission, anode voltage, axial magnetic field, discharge pressure in the plasma (determined by the chamber temperature or the leak valve setting, depending on the beam material), extraction gap, extraction voltage, and lens electrode potentials. The angular orientation of the lens is also important for efficient injection of the beam into the analyzing field. All the operating parameters, magnetic field included, are observed to be greatly interdependent, so an iterative adjustment technique most successfully maximizes the beam throughput. It should be noted that the focused beam current is not maximum at the settings which give the most plasma current. In particular, the former generally peaks at the minimum solenoid field and plasma pressure for which a plasma can be maintained. Conditions do not change greatly from one charge material to another, however.

Typical beam current data for an Ar^+ beam extracted and analyzed at 2keV are given in Table 1. No slits were used on the magnetic analyzer for these measurements, except where noted. Some of the data were taken with a specially constructed detector array described in Ref. 14.

The data were, of course, taken at different times because the setup had to be changed when the analyzer was installed and when the slits were changed. Nevertheless, it is remarkable how small the losses are in the magnetic analyzer.

Mass scans were used to estimate the resolution of the mass analyzer. When a temporary 2mm wide slit was in place, it was possible to separate Ar^{36} from Ar^{40} . The natural abundances of these isotopes are in the ratio of 1:320, indicating a resolution certainly greater than 10. After the 1

TABLE I

Typical Beam Performance Data

1. Charge material: Argon gas
2. Flow rate setting (Granville-Phillips valve): 133 (near min. required to sustain a plasma discharge)
3. Anode voltage: 76V
4. Anode current: 1.0A
5. Solenoid current: 1.0A
6. Extraction/analysis voltage: 2kV
7. Analyzer field: 5.3 kilogauss
8. Extraction/focusing lens: set for maximum
9. Total extracted current: $\approx 25 \mu\text{A}$
10. Current through 10 mm x 2 mm slit at focus of lens:
 $\approx 4 - 8 \mu\text{A}$
11. Current (Ar^+) through 10 mm x 2 mm slit at exit of analyzer:
 $\approx 7 \mu\text{A}$
12. Fraction of above (#11) within .05 radian half-angle of divergence: $\approx 60\%$
13. Current (Ar^+) through 1 mm wide slit at exit of aperture:
 $\approx 2 - 3 \mu\text{A}$

mm wide exit slit was installed, it was easy to resolve masses at 56AMU and 58AMU (the principal isotopes of iron and nickel). This gives a resolution $R \geq 28$.

The special detector array, referred to above, was also used to investigate the properties of the retarding lens. The beam could be slowed from 2keV to about 100 eV with little or no loss of intensity. The beam divergence was somewhat affected, however, and depended strongly on the retarding lens setting. For any given energy it was possible to make the beam practically parallel but accompanied by some loss of intensity. The retarding lens must be set empirically.

2.3 Charge Exchange Production of Neutral Beams

A simple charge-exchange process is used to neutralize the fast ion beam, thereby forming a beam of fast neutral atoms or molecules. The ion beam is passed through a chamber containing a neutral gas or vapor of the same species, for which the cross-section for electron exchange is high. The exchange process involves little momentum transfer (Ref. 15), so the neutral beam thus produced has the same energy and direction as the original ion beam. Residual ions are swept out by electrostatic deflecting plates. The chamber and analysis is based on those described by Utterback and Miller (Ref. 16).

2.3.1 CEX chamber. - A horizontal cross-sectional view of the charge-exchange (CEX) chamber is shown in Figure 10. It mounts on a dovetail slide as part of a pre-aligned assembly which also includes the retarding lens and the mass analyzer exit slit. The entire assembly may be translated in a

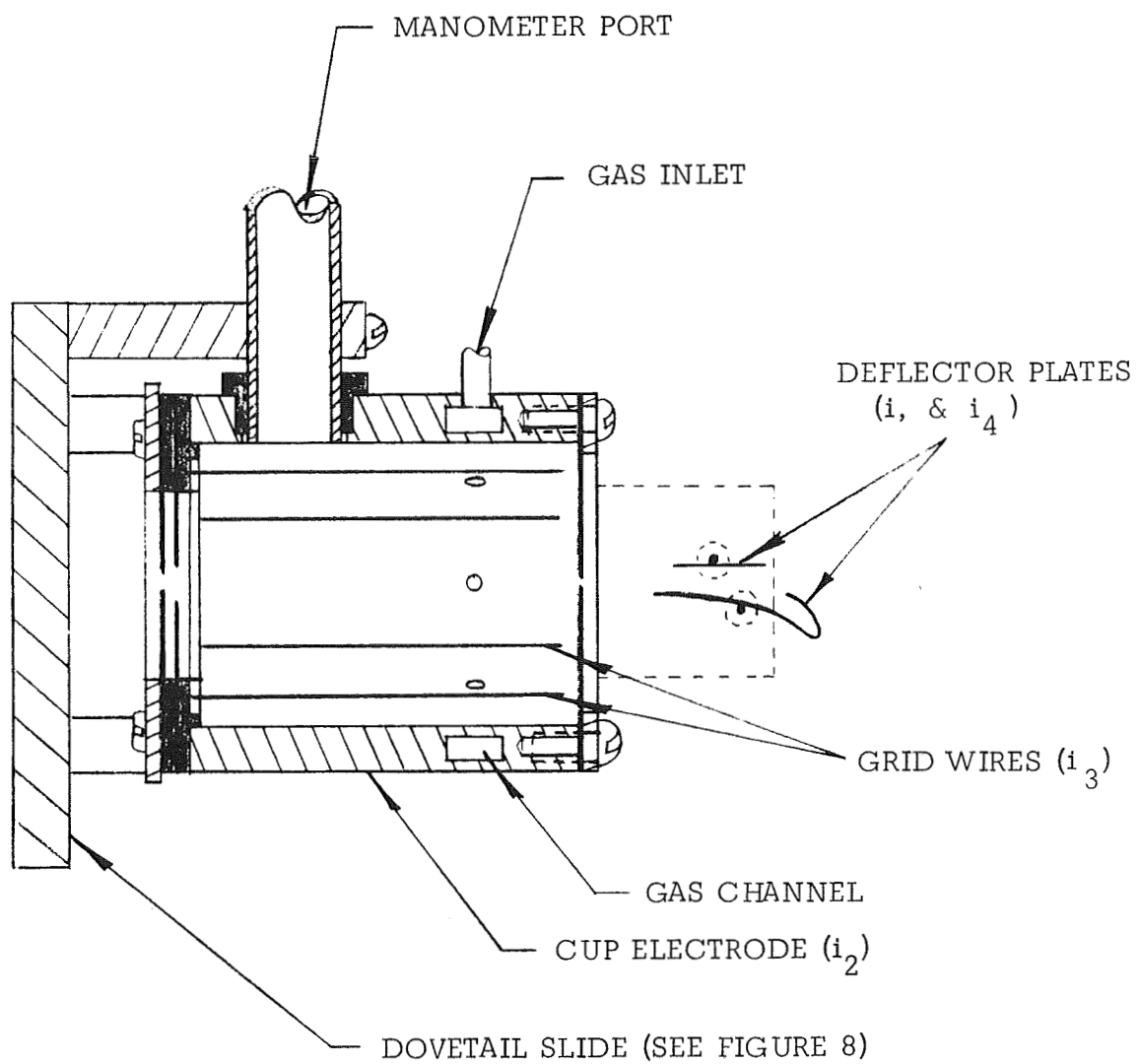


Figure 10. Charge-Exchange Chamber Assembly

horizontal direction from outside the vacuum system.

The beam apertures must be kept as small as possible to prevent too much gas flow for the pumps to handle, but not so small as to severely limit the beam current. The entrance and exit slit dimensions are 2.1 mm x 10 mm and 1.3 mm x 8.1 mm respectively. The entrance slit serves as one of the collimating slits for the beam through the collision region. This is discussed fully in 2.5.1.

The deflecting plates are designed to collect the total ion current emerging from the CEX chamber exit slit. The beam displacement is given by

$$d = \frac{q \cdot \frac{V}{h} \cdot L^2}{4E} \quad (14)$$

where

d = displacement from initial axis while within length L

L = length of deflecting field

V = deflecting voltage

h = distance between deflecting plates

q = ion charge (in units of e)

E = ion energy (in eV)

Note that this is independent of the ion mass. The existing geometry has $L = 1.5$ cm, $h \approx 0.25$ cm, and the required minimum displacement is $h/2$. The deflecting voltage required to collect a singly charged beam at 2000 eV is then

$$V > \frac{2Eh^2}{q L^2} = 111 \text{ volts .}$$

For higher energies a proportionately higher deflecting voltage would be required. In the present setup, $V = 126$ volts as provided by three 42 volt batteries in series.

The drawing shows the arrangement for supplying the exchange gas and for measuring its pressure with a capacitance manometer.

2.3.2 Computation of neutral beam intensity. - We wish to derive a formula giving, in terms of measurable quantities, the neutral beam intensity passing through the collision region during the experiment. The method is based on that of Utterback and Miller (Ref. 16). We make the assumptions that charge transfer and scattering are unrelated processes, and that the scattering of fast neutrals and fast ions is essentially the same.

Let β represent the fraction of entering ions which undergo charge-exchange and i_0 equal the emerging ion beam current if no exchange had occurred (i.e., if $\beta = 0$). Then the emerging neutral beam intensity (equivalent current, corresponding to 0.624×10^{19} particles per ampere) is

$$B = \beta i_0 . \quad (15)$$

We must calculate β and i_0 in terms of measurable quantities. Three current measurements are required:

1. i_1 = ion collector current, due to ions passing through the exchange chamber.
2. i_2 = outer cup current, due to ions undergoing elastic scattering without exchange and ions not well enough collimated to pass through the exit slit. The cup is biased a few volts positive to

prevent the thermal velocity ions produced by charge-exchange from being collected there. The electrode behind the entrance slit is also maintained at the cup potential, but not connected to it, to prevent slow ions from migrating to the entrance slit.

3. i_3 = grid current, corresponding to all slow ions produced by exchange in the CEX chamber. Fast ions collected by the grid are negligible because of its small solid angle.

The total current entering the exchange chamber is the sum $i_1 + i_2 + i_3$, and β is evidently

$$\beta = \frac{i_3}{i_1 + i_2 + i_3} \quad (16)$$

We can now relate i_0 to the emerging current i_1 :

$$i_1 = i_0 - \beta i_0,$$

or

$$i_0 = \frac{i_1}{1 - \beta} \quad (17)$$

Therefore, substituting (16) and (17) into equation (15),

$$B = \frac{\beta i_1}{1 - \beta} = i_3 \left(\frac{1}{1 + i_2/i_1} \right). \quad (18)$$

One more manipulation is necessary to get the neutral beam intensity passing through the collision chamber where experiments are performed. The quantity B represents the neutral particles emerging from the CEX chamber. Many of these are lost on the entrance slit of the collision region, which is the second collimating aperture. Since the distribution of emerging fast neutral particles and ions is the same (a consequence of having negligible momentum transfer during exchange), the fraction of B retained is the

same as the fraction of ions retained when they are allowed to pass undeflected into the collision region when no exchange gas is present. Therefore we have a neutral beam intensity given by

$$N = 0.624 \times 10^{19} \times \frac{B i_F}{i_T} \quad \frac{\text{particles/sec}}{\text{ampere}}$$

where i_F is the current measured at the collision region Faraday cup, and i_T is the total current emerging from the CEX chamber.

2.3.3 Operational data. - Data taken to check the performance of the charge-exchange chamber and measurement equipment are contained in the laboratory notebooks provided with this report. Typical data, from which we may compute the neutral beam intensity and exchange efficiency are given in Table II.

We use equations (18) and (19) to compute the equivalent neutral beam current from the data of Table II (current i_1 must be corrected for secondary electron current given as i_4 in the table - see Section 2.4.2):

$$\begin{aligned} \text{Neutral beam intensity} &= 160 \left(\frac{1}{1 + 250/220} \right) \times \frac{210}{470} \text{ nA} \\ &= 33.5 \text{ nA} . \end{aligned}$$

For comparison, we can use the bolometer signal and its calibrated responsivity to compute the incident current. We assume an accommodation coefficient of 1. The bolometer responsivity (in a bridge circuit) is approximately 162 volts/watt. We therefore compute an input power:

$$\text{incident power} = 4.4 \text{ mV} : 165 \text{ volts/watt} = 27 \text{ } \mu \text{ watts}.$$

The power is provided by particles having 900 eV energy, so their equivalent

TABLE II

Neutral Beam Measurements

1. System: N_2^+ (900 eV) + $N_2 \rightarrow N_2$ (900 eV) + N_2^+
2. Current through CEX chamber (no collision gas): 470 nA
3. Current into Faraday cup (no collision gas): 210 nA
4. Exchange gas pressure: 1.1 μ Hg
5. Bolometer bias voltage: 550 V
6. Bolometer output (corrected for amplifier gains): 4.4 mV
7. $i_1 = 310$ nA
8. $i_2 = 250$ nA
9. $i_3 = 160$ nA
10. $i_4 = -90$ nA

current is

$$27 \mu \text{ watts} / 900 \text{ V} = 29.6 \text{ nA},$$

which is in satisfactory agreement with the current calculated from CEX electrode currents since the bolometer does not subtend the whole beam.

The bolometer output was also plotted as a function of exchange gas pressure, and shown to reach a saturation value at about $1.5 \mu \text{ Hg}$. At pressures substantially higher than this ($\sim 3 \mu \text{ Hg}$), the bolometer output falls off, presumably because the beam is attenuated by scattering outside the CEX chamber.

2.4 Measurement of Beam Intensities

This section covers the signal detection and processing equipment used to measure and monitor the absolute intensities of the ion and neutral beams. Particular attention will be paid to the special electronic equipment built to accomplish these tasks.

2.4.1 Ion beams. - The primary ion current through the collision region is collected by a Faraday cup. Secondary electrons are prevented from leaving the cup by an entrance aperture biased a few volts ($\sim 15\text{V}$) negative. The collected ion current must eventually complete a circuit to its source, and care is taken to see that this is done through a special return line -- a high-quality ground. Signal processing is done as follows.

The cup current, and also the currents from 6 other collision chamber electrodes, are carried through a shielded cable to a specially designed NIM-bin module that performs two basic functions: (1) First, it serves as a

junction box for all the currents, enabling any combination of them to be shunted directly to the high-quality ground, grounded through bias voltage supplies, shunted through a pair of monitor terminals (connected to an electrometer, for example) or applied to the input of an amplifier that constitutes its second function. (2) It incorporates an operational amplifier system, used as a dc-coupled current-to-voltage transducer, that provides an output suitable to drive a Princeton Applied Research model CW-1 Boxcar Integrator, where the currents are monitored and recorded.

The amplifier has calibrated gain ranges from 10^{-1} to 10^4 mV/nA in decade steps, and a range multiplier with x1, x10, x100, and x1000 positions. The range multiplier is not necessary, and is normally used in the x1 position. Higher multiplication factors affect the rise-time and thermal stability adversely. In the x1 position, the equivalent noise current at the input is $\approx 10^{-12}$ A. At the highest gain normally used, 10^4 mV/nA x 1, a 10^{-12} A signal would give 5% of full scale deflection on the most sensitive scale of the Boxcar Integrator. Drawing SK-120-3327 is a logic diagram of this unit, and its wiring layout is given in SK-120-3326. A detailed description of its operation is given in Appendix B.

2.4.2 Neutral Beams. - Neutral beam intensity can be measured or monitored in two ways - (a) by measuring CEX currents and using equation (18), or (b) by a bolometer system which directly detects the kinetic energy of the neutral beam.

(a) Current measurements:

Drawing SK-120-3329 is a schematic diagram of the system built to measure the currents from the CEX electrodes and to

provide the required bias voltages. It is a self-contained, battery powered unit. Four identical, FET input, operational amplifier channels measure the currents i_1 , i_2 , i_3 and the secondary electron current picked up by the positive deflector plate. The last is not really necessary, since its input could be added to the channel 1 (current i_1) input, thereby precisely cancelling the secondary electron contribution.

Each channel consists of a Fairchild Controls model ADO-39 operational amplifier with a precision 1 Meg feedback resistor giving a gain conversion factor of $1\text{V}/\mu\text{A}$. A $.01\ \mu\text{f}$ bypass capacitor limits the high frequency response and stops a tendency to oscillate. The input is coupled through a 1K current-limiting resistor, and back-to-back diodes across the input give protection against high voltage transients. Each channel is decoupled from the $\pm 10.7\text{V}$ battery supplies by an RC circuit, to prevent power line cross-coupling between channels.

Bias voltages for the outer cup and slit electrodes are provided by identical, potentiometer tapped 42V batteries; the deflecting voltage is supplied by a fixed 126V battery pack. Bias voltages are at ground potential when their switches are in the "off" positions.

The amplifier outputs may be observed on an oscilloscope or applied to the boxcar integrator input after additional amplification to increase the voltage signal to 0.1V or higher.

(b) Bolometer measurements:

The use of a bolometer to detect molecular beams was first described by Jordan and Amdur (Ref. 17). The bolometer consists of two matched thermistor flakes carefully mounted on sapphire blocks in a common housing. One serves as the detector, or active, flake and the other is shielded and serves as a compensator. They are normally used as IR radiation detectors, but since their mode of response is a thermally induced resistance change, they can be used to detect any process that causes sufficient power to be deposited in the active flake.

Two such bolometers were ordered: one from Barnes Engineering Company and one from Servo Corporation of America. The Barnes bolometer was burned out in an early test. The Servo bolometer is now installed. Its basic specifications are given in Table III.

Complete descriptive information and specifications can be obtained from the manufacturer.

If other sources of noise and interference are kept small (a low noise bias supply and signal amplifier are required), it should be possible to detect signals of the size of the N.E.P., say 10^{-9} watts. This corresponds to a beam of 0.1 nA at 10eV incident on the 2.5 mm^2 active flake. The data given in 2.3.3 indicate that we indeed approach this sensitivity. Such a small signal would give a response at the amplifier input of about 0.1 μ V. High gain is therefore required to produce a recordable output.

The bolometer system electronics are shown in drawing

TABLE III

Bolometer Specifications

1. Flake size = 1 mm x 2.5 mm
2. Flake resistance (across 1 mm dimension) = 1.2 Med ohm
3. Time constant = 4.0 millisec.
4. Operating bias = 275 volts/flake, max.
5. N.E.P. = 6×10^{-10} watts (1 Hz bandwidth at 15 Hz chopping rate).*
6. Responsivity = 325 volts/watt.*

* N.E.P. and responsivity are half these values in a bridge circuit.

SK-120-3330. A low-noise, high gain (40 db) amplifier is mounted inside the vacuum system as close as possible to the bolometer. An external control box contains a 10.7 V battery supply for the amplifier and an RC ripple filter for the bias supply. It also serves as a junction box for the signals, including the Faraday cup output. Separate power and signal return leads are used to prevent power line drops in the cable from appearing on the signal channel. Bias must be provided by a well-filtered, stable supply (Fluke model 412B or equivalent). Caution must be exercised when applying the bias voltage: Polarity must be observed and power applied in increments not exceeding 100V, or the amplifier may be damaged. Maximum bias voltage for the Servo bolometer is -550V.

The amplifier output may be observed on an oscilloscope or, after further amplification, recorded by the boxcar integrator or, preferably, a lock-in amplifier.

2.5 Interaction Regions

Two interaction regions were built, the first having been designed for ion-gas collisions, the second for ion-and neutral-gas collisions. They are much the same, except the second one can be aligned with the beam from outside the vacuum system and has interchangeable detectors - either a Faraday cup or the bolometer may be used. It also has easier access for optical alignment purposes. Only the second system will be discussed in this section, and the major differences will be pointed out.

2.5.1. Determination of slit sizes. - Reasons for selecting the various slit sizes are given in detail in the laboratory notebooks provided with this report. We only summarize the calculation and results here.

The geometry for the final stages of beam trajectory is indicated in Figure 11 (we consider spreading only in the plane perpendicular to the narrow slit dimension). We desire to collimate the beam such that all particles entering the collision region through w_2 also pass through w_3 , and to do this in such a way that the beam is maximum. A collimating slit upstream from w_2 is required. We select the entrance slit of the CEX chamber, w_1 , to serve this purpose since it must be small, anyway, to restrict gas flow. Beam trajectories are considered to be straight lines after emerging from w_R , the exit slit of the retarding lens. We assume that the retarding lens forms an image of w_0 on w_1 , where w_0 is the exit slit (focus) of the analyzer field, from which the beam emerges at energy E_0 with divergence θ_0 . The image width w_i depends on the properties of the retarding lens. The energy after retardation is E_1 , the divergence θ_1 .

The maximum beam is obtained if we collect the entire object, width w_0 , over its entire field θ_0 , or equivalently, w_1 over its field θ_1 . We can write the following expressions for the fraction of the ions collected (recall that we treat spreading in one plane only):

$$\text{Fraction of image transmitted} \approx \frac{w_1}{w_i}, \text{ but not greater than 1.}$$

$$\text{Fraction of angle collected} \approx \frac{w_2/L_1}{\theta_1}.$$

$$\text{Fraction of total current collected} \equiv F \approx \frac{w_1}{w_i} \times \frac{w_2}{L_1 \theta_1} \quad (20)$$

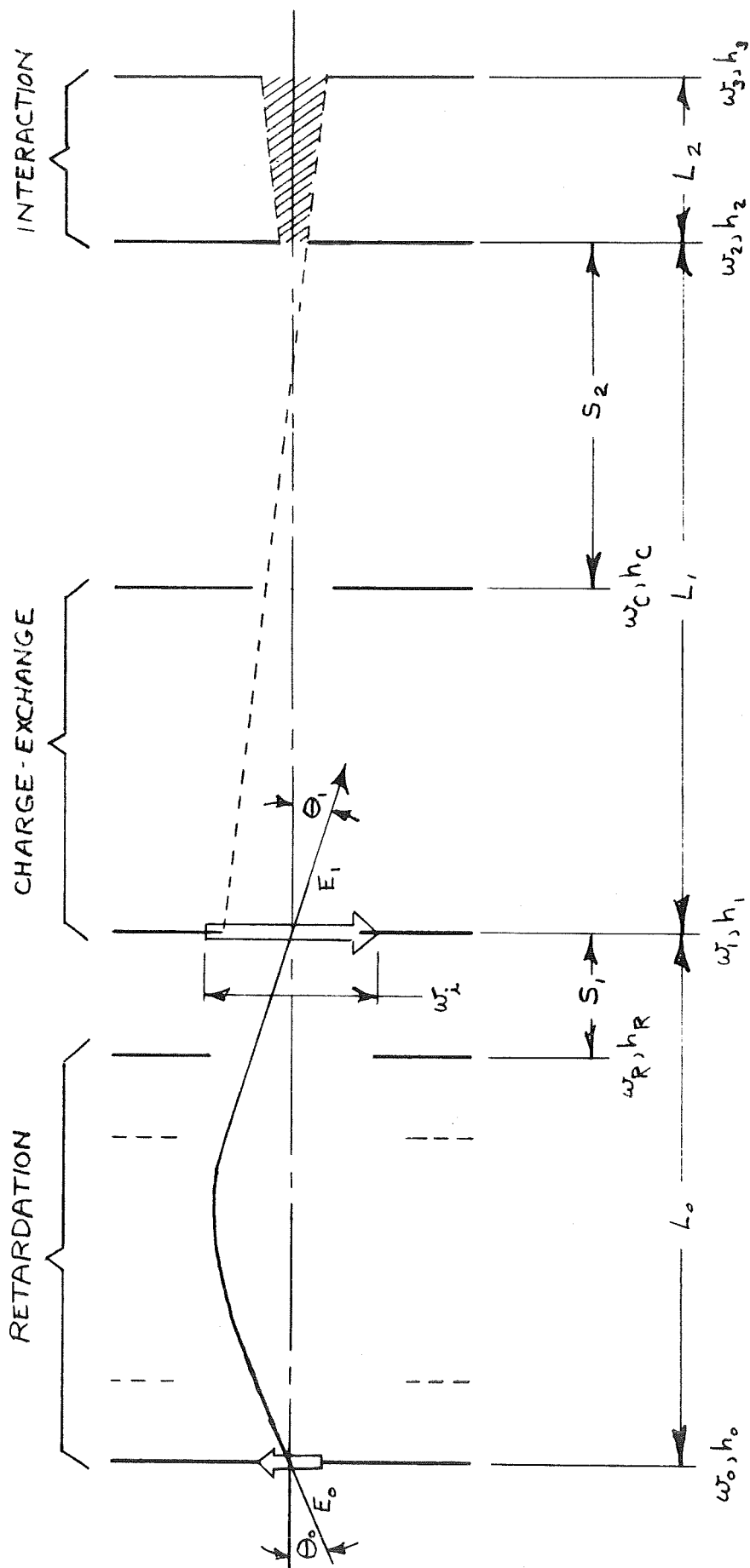


Figure 11. Geometry for Slit Calculations

In ion optics the beam velocity, or \sqrt{E} is analogous to the refractive index in light optics. Therefore the Abbe sine condition for ion optics is:

$$w_o E_o^{1/2} \sin \theta_o = w_i E_i^{1/2} \sin \theta_i . \quad (21)$$

Using small angle approximations, we now have

$$F \approx \frac{w_1 w_2}{w_o \theta_o L_1} \left(\frac{E_1}{E_o} \right)^{1/2} , \quad (22)$$

which is to be maximized.

It is readily seen, from similar triangles (Figure 11), that collimation is just attained when

$$\frac{w_3 - w_2}{L_2} = \frac{w_1 + w_3}{L_1 + L_2} ,$$

or

$$w_1 = \left(\frac{L_1 + L_2}{L_2} \right) (w_3 - w_2) - w_3 . \quad (23)$$

If we substitute (23) into (22), and also let the parameter a be defined by

$$L_1 = aL_2 , \quad (24)$$

$$\text{we get } F = \left[\frac{w_2 w_3}{L_2} - \frac{w_2^2}{aL_2} - \frac{w_2^2}{L_2} \right] \times \frac{(E_1/E_o)^{1/2}}{w_o \theta_o} , \quad (25)$$

which is to be maximized.

It is now necessary to make some observations about the quantities appearing in equation (25). The energies E_1 and E_o are determined by the experiment being done at any particular time, and are not available for adjustment

to maximize F. Similarly, w_0 and θ_0 were previously determined by the mass analyzer requirements. For reasons not yet discussed (see Section 2.6), the length L_2 and maximum width w_3 of the interaction region are restricted, and we take

$$w_3 = 1 \text{ mm}$$

$$L_2 = 25 \text{ mm.}$$

We have left only the parameter a and width w_2 to adjust for maximized beam.

We therefore have

$$\frac{\partial F}{\partial a} = 0 \rightarrow \frac{w_2^2}{a^2} = 0 \quad (26)$$

and

$$\frac{\partial F}{\partial w_2} = 0 \rightarrow w_3 - \frac{2w_2}{a} - 2w_2 = 0 \quad (27)$$

Equation (27) gives the result

$$w_2 = \frac{a}{2(1+a)} w_3 \quad (28)$$

Substituting (28) in (23) gives

$$w_1 = \frac{a}{2} w_3, \quad (29)$$

and of course we had equation (24) giving $L_1 = aL_2$. We have therefore expressed our three undetermined collimation dimensions in terms of the parameter a . If we substitute (28) in (26), we find that we would like to have $a = \infty$. We must therefore be satisfied with the largest value of a that leads to acceptable dimensions from other viewpoints. We do not lose strongly for values as low as $a = 2$, and the maximization is not valid, anyway, if $w_i < w_1$.

Again, referring to Figure 11, we see that $L_1 = 4 \frac{1}{4}"$ leaves adequate room for a CEX chamber and gives $a = 4.25$. This dimension is compatible with other mechanical design criteria not covered in this report.

Similar considerations are used to evaluate the slit heights, but in this case straight-line trajectories are assumed and the problem reduces to one of geometrical collimation, where the heights h_0 , h_1 , and h_3 are all arbitrarily selected as 1 cm, which is slightly larger than the vertical height of the drift-tube opening. Widths w_R and w_C are selected to be just large enough to pass the beam, assuming straight-line trajectories. The final dimensions are given in Table IV.

2.5.2 Second assembly. - A cross-section (viewed from above) of the principal parts of the second collision chamber is shown in Figure 12. The assembly of interaction region electrodes is mounted in a dovetail arrangement on the partition that confines the collision gas. It can be moved from outside the vacuum via a bellows-sealed feedthrough. The entrance and exit slits are w_2 and w_3 , respectively, of the preceeding sub-section. We recall that the collimation is done such that all particles pass completely through both slits (in the absence of target gas).

The electrode numbers are for reference, and correspond to the pin numbers of the octal feedthrough and the channel number of the current amplifier previously described. Electrode #1 is normally biased a few volts positive to collect secondary electrons ejected from the front of the slit, and #6 is biased negative to prevent election loss from the Faraday cup. The side electrodes, #3 and #4, may be biased to collect slow ions and electrons produced within the interaction volume.

TABLE IV

Slit Geometry

(Refer to Figure 11)

| | | | |
|----|---|-----|-------------------------|
| 1. | $L_0 = 3 \frac{1}{4}" = 83\text{mm}$ | 10. | $w_1 = 2.12 \text{ mm}$ |
| 2. | $L_1 = 4 \frac{1}{4}" = 108 \text{ mm}$ | 11. | $h_1 = 10 \text{ mm}$ |
| 3. | $L_2 = 1" = 25 \text{ mm}$ | 12. | $w_C = 1.27 \text{ mm}$ |
| 4. | $S_1 = 3/4" = 19 \text{ mm}$ | 13. | $h_C = 8.13 \text{ mm}$ |
| 5. | $S_2 = 2 \frac{1}{8}" = 54 \text{ mm}$ | 14. | $w_2 = 0.40 \text{ mm}$ |
| 6. | $w_O = 1.0 \text{ mm}$ | 15. | $h_2 = 6.25 \text{ mm}$ |
| 7. | $h_O = 10 \text{ mm}$ | 16. | $w_3 = 1.0 \text{ mm}$ |
| 8. | $w_R = 2.57 \text{ mm}$ | 17. | $h_3 = 10 \text{ mm}$ |
| 9. | $h_R = 12.9 \text{ mm}$ | | |

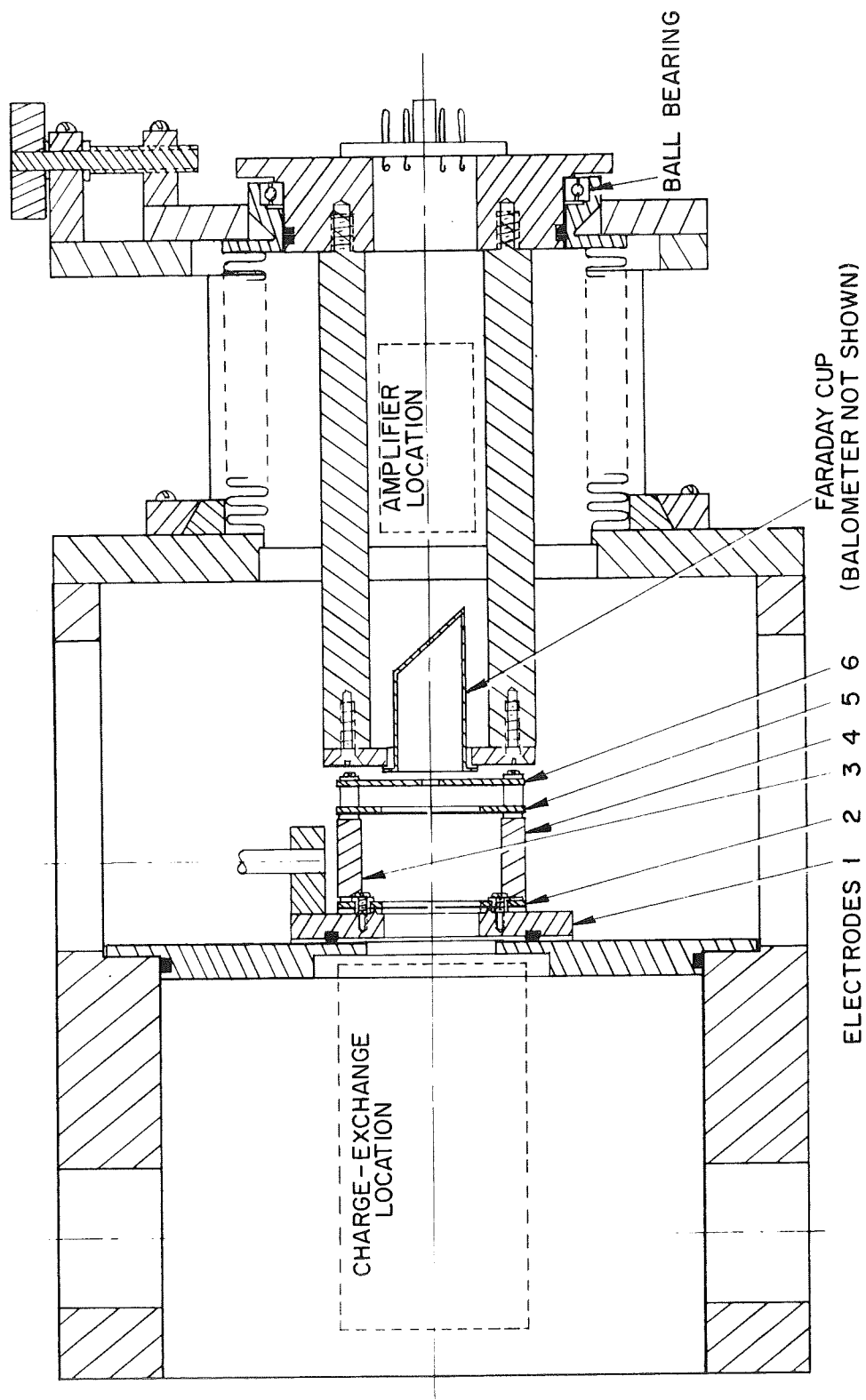


Figure 12. 2nd Interaction Region/Detector Assembly.

The detector assembly is also shown in Figure 12. The bolometer and Faraday cup can be interchanged by 180° rotation about the holder axis, which is parallel to but $\frac{1}{2}$ " above the beam axis. The bearing facilitates rotation. The whole assembly can be translated horizontally and vertically for alignment. This will also allow scans of the beam distribution to be made.

The first collision region has a much different vacuum housing arrangement, as can be seen by inspection of the pertinent construction drawings, but was in principle the same. It could be aligned only when the vacuum chamber was open, however, and the Faraday cup was an integral part of the interaction region electrode assembly. It also had a mirror mounted on it as part of its corresponding optical system.

2.5.3 Target gas thickness. - To perform absolute cross-section measurements, it is necessary to know the target gas thickness, or number of targets per cm^2 presented to the incident beam. This is simply the target particle density (number/ cm^3) times L_2 (in cm), and the density is found from the perfect gas law if we know the pressure and temperature (see Section 3.2).

Pressure is measured, in both collision regions, by a calibrated capacitance manometer which may be checked against the McLeod gauge. Calibrated thermistors are used to determine T , but this is nearly room temperature ($\approx 300^\circ \text{K}$) and is not critical for measurements with a few percent uncertainty.

2.6 First Optical/Calibration System

Each of the collision regions has a corresponding optical system whose functions are (1) to collect light energy released during the collision processes, (2) to determine the wavelengths of emitted radiation, with the goal of evaluating what excitation mechanism is responsible, and (3) to measure the rate of photon production at any wavelength (between 2500 \AA and 8000 \AA) so absolute cross-sections can be computed. These three functions are performed or assisted by the fore-optics, monochromator and calibration system, respectively.

2.6.1 Fore-optics. - We recall that the primary beam is restricted to the volume bounded by the maximum slit dimensions, as indicated by the shaded area in Figure 11. Under the assumption of single collision processes (which can be achieved by using low enough gas pressure, provided the cross-section for primary excitations is at least comparable in size to the cross-sections for secondary processes), the light we wish to detect also originates in the indicated volume. The dimensions of the emitting volume therefore depend somewhat on the optical system: the maximum width w_3 affects the spectral resolution, as we shall see, and the length L_2 is based on the limits of the optical field. (Since the light produced by the beam is nearly proportional to its interaction length, we are not interested in minimizing L_2 to maximize F in equation (25). For absolute cross-section measurements, we must collect the emitted light with known and equal sensitivities for every point within the volume.

The design of the optical system to collect and process this light is based on the principles set forth in Refs. 18 and 19. In particular, ne-

glecting transmission losses, any optical system which fills both the entrance slit and the field-of-view of a spectrometer achieves the maximum possible collection efficiency. The only ways to obtain a higher energy throughput are to increase the brightness of the source itself or to increase the field and/or slit size of the spectrometer. The monochromator selected to do the spectral analysis has an $f/5.3$ maximum field, and a dispersion of 26 \AA/mm , with the slit adjustable up to 2 mm in width and 2 cm in height.

For a diffuse source such as the interaction volume, it is apparent that the maximum brightness is obtained by looking through the longest dimension. In this case, the vertical axis must be used since the beam axis is excluded from use by the beam detector. We could do no better, therefore, than to place the monochromator above the interaction region, its entrance axis vertical, such that the entrance slit is adjacent to the radiating volume and the slit width is set for adequate resolution. We take the latter to be 13 \AA for design purposes, requiring 0.5 mm slits. But such a monochromator location is impractical, so an optical system was built to accomplish the same thing in accordance with the principle underlined above.

One aspect of the design must be emphasized. If absolute measurements are to be made, it is important that the entire image of the interaction region be focused through the entrance slit. Otherwise, it would not be possible to relate the beam current through the whole interaction region to the photons from only part of it.

Details of the design are given in the laboratory notebooks. The final optical configuration is indicated in Figure 13. A 45° mirror is employed

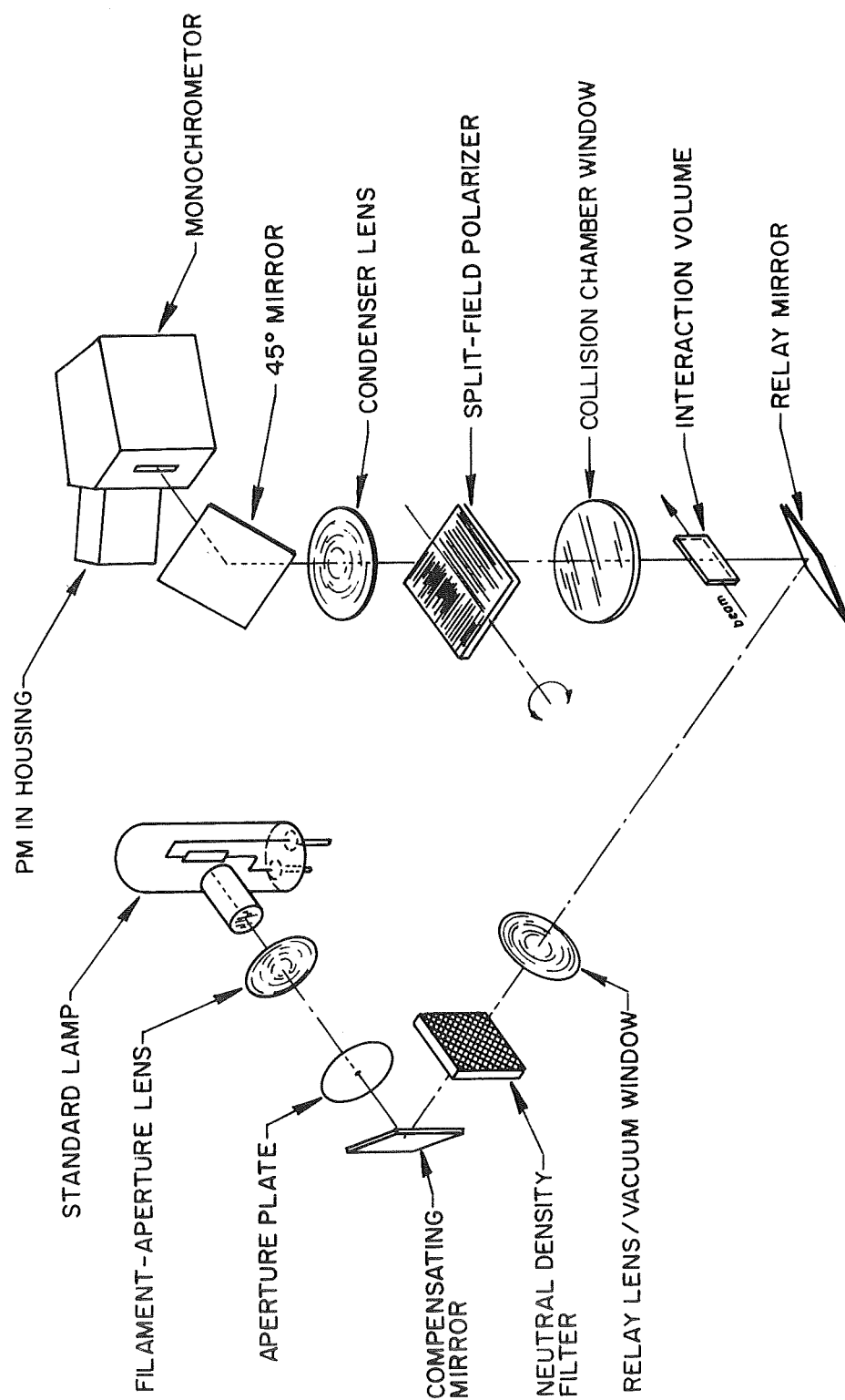


Figure 13. First Optical/Calibration System

so the monochromator can be mounted in a base-down position. The condensor lens produces an image of approximately half the true linear dimensions. Thus, for $\frac{1}{2}$ mm slits, the beam width must not exceed 1 mm, and the slit height must be at least 12.5 mm for a 25 mm interaction length. The actual focal length and magnification are, of course, wavelength dependent, so the image is not in focus on the entrance slit at all wavelengths. More will be said about this when the calibration optics are discussed.

Both the mirror and the lens were chosen to fill the field of the monochromator at their respective locations in the optical path. (Actually, the lens is marginal in size and the signal should be increased by 1.25% to compensate for a slight loss - this applies to the beam signal only, and not to calibration.) A split-field polarizer is also installed to permit polarization analysis of the emitted light. Polarization vectors parallel to or perpendicular to the beam axis may be selected by 180° rotation of the holder shaft. The polarizer holder partially blocks the optical path when it is in the intermediate (90°) position.

If we assume isotropic radiation, this optical system collects (geometrically) about $1/2330$ th of the total light output, whereas the f/5.3 monochromator located at the interaction region would collect $1/450$ th. The difference is the price paid for better resolution.

2.6.2 Monochromator. - Aside from certain mechanical features and cost restrictions, it was desired to choose a spectrum analyzer with the greatest possible wavelength range, optical efficiency, and field-of-view. The unit chosen was the McPherson Model 218, which is a high-efficiency, grating

monochromator with an $f/5.3$ optical system and a scan range of 1050 \AA to 1μ with its standard grating. It also has the useful features of automatic scan, adjustable slits, and evacuable housing. The observable wavelengths are not limited by the monochromator, but by quartz optics and photomultiplier cathode response, which cut off at 1800 \AA lower limit and 8000 \AA upper limit, respectively. As mentioned previously, the slit height can be set up to 2 cm, and the width to 2 mm; only the width is continuously adjustable from outside the vacuum system.

2.6.3 Calibration system. - the calibration system used with the first collision chamber is also shown in Figure 13. Its purpose is to provide a source of light of known spectral output, radiating from the interaction region into the fore-optics and monochromator system with the same geometric efficiency as applies to an average point of the emitting volume.

The light source is a tungsten-ribbon filament lamp of a known spectral radiance ($\mu \text{ watts/mm}^2 \cdot \text{\AA} \cdot \text{ster}$), as calibrated by Eppley Laboratory and traceable to the National Bureau of Standards. The lamp output is plotted in Figure 14. If we temporarily neglect transfer losses in the optical system, any image of the filament has the same spectral radiance as the filament itself. We therefore form a filament image on an aperture plate of known area, and in turn focus the aperture on the interaction region. Two mirrors complete the optical relay system: one below the interaction region is required for mechanical reasons, and another, which folds the optical axis into a plane perpendicular to the plane of the first bend, compensates for any polarization introduced by the first reflection. All

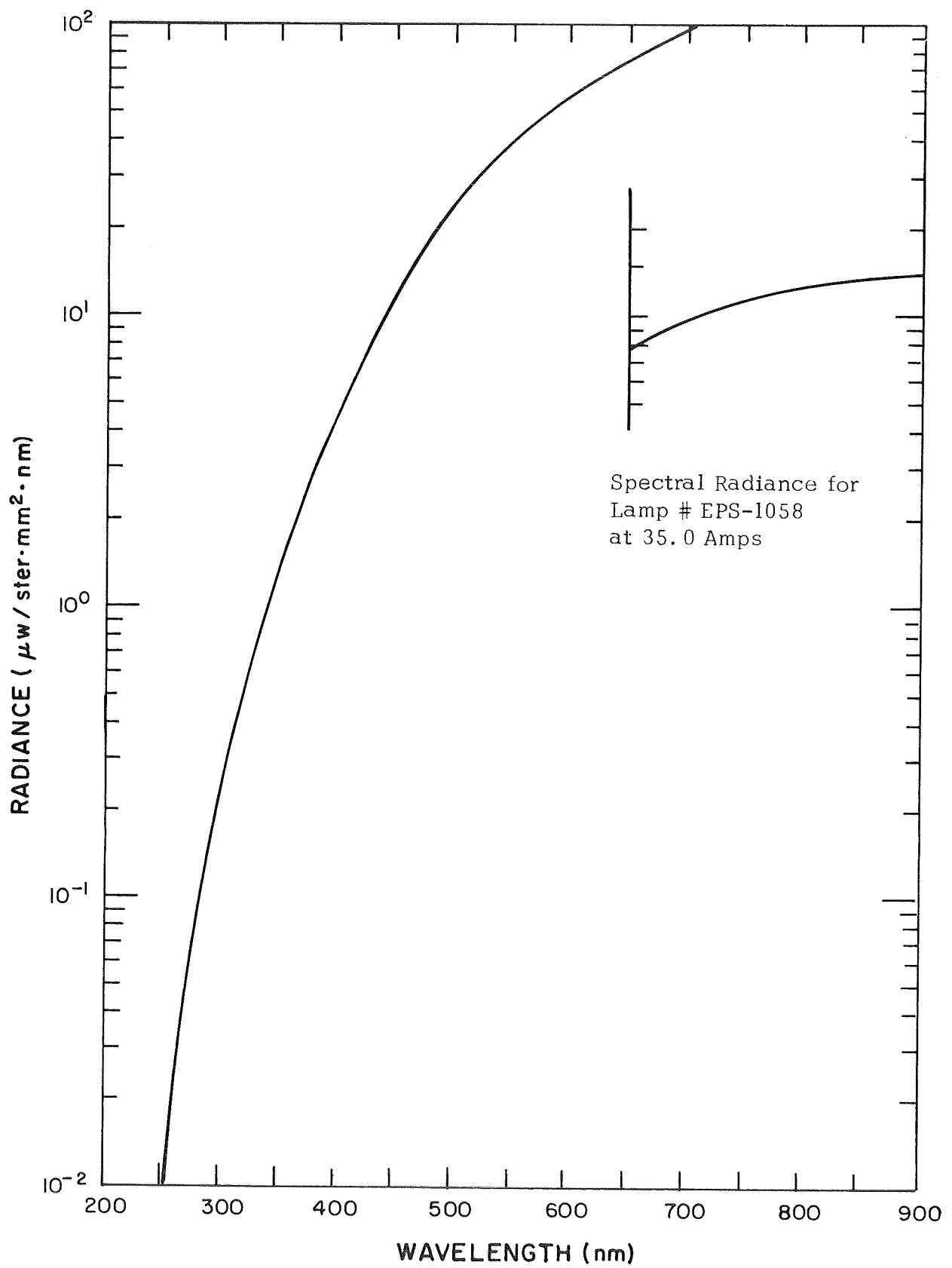


Figure 14 Lamp Output

components are selected so the field of the fore-optics is overfilled. The spectral power radiating into the fore-optics is now given by

$$P_{\lambda} = R_{\lambda} \cdot A \cdot m^2 \cdot \Omega_F \cdot \Delta\lambda \quad (30)$$

where

R_{λ} is the lamp radiance at wavelength λ .

A is the aperture area.

m is the linear magnification of the relay lens.

Ω_F is the solid angle accepted by the fore-optics.

$\Delta\lambda$ is the bandpass of the monochromator.

Power at any wavelength is converted to a photon rate by dividing by the photon energy $h\nu$.

Since the index of refraction of the quartz lenses varies with wavelength, it is necessary to focus the optical system for each wavelength used. The relay lens is fixed (it also serves as a vacuum window), so refocusing is done by moving the aperture, thus changing the object distance u . This also causes the magnification m to change. These quantities are plotted vs. wavelength λ in Figures 15 and 16, and must be referred to when calibrating at any wavelength. The object distance is easily set by reference to a scale on the side of the adjustable aperture carrier.

Equation (30) is not valid unless we apply to it the transfer losses of the calibration optics. These are of three types: (1) There are losses intentionally introduced in the form of neutral density filters in order to reduce the calibration light intensity to a level compatible with photon counting techniques. Filters of nominal densities 1.0, 2.0 and 3.0, with transmission curves, are provided. (2) Since the lamp output of red light

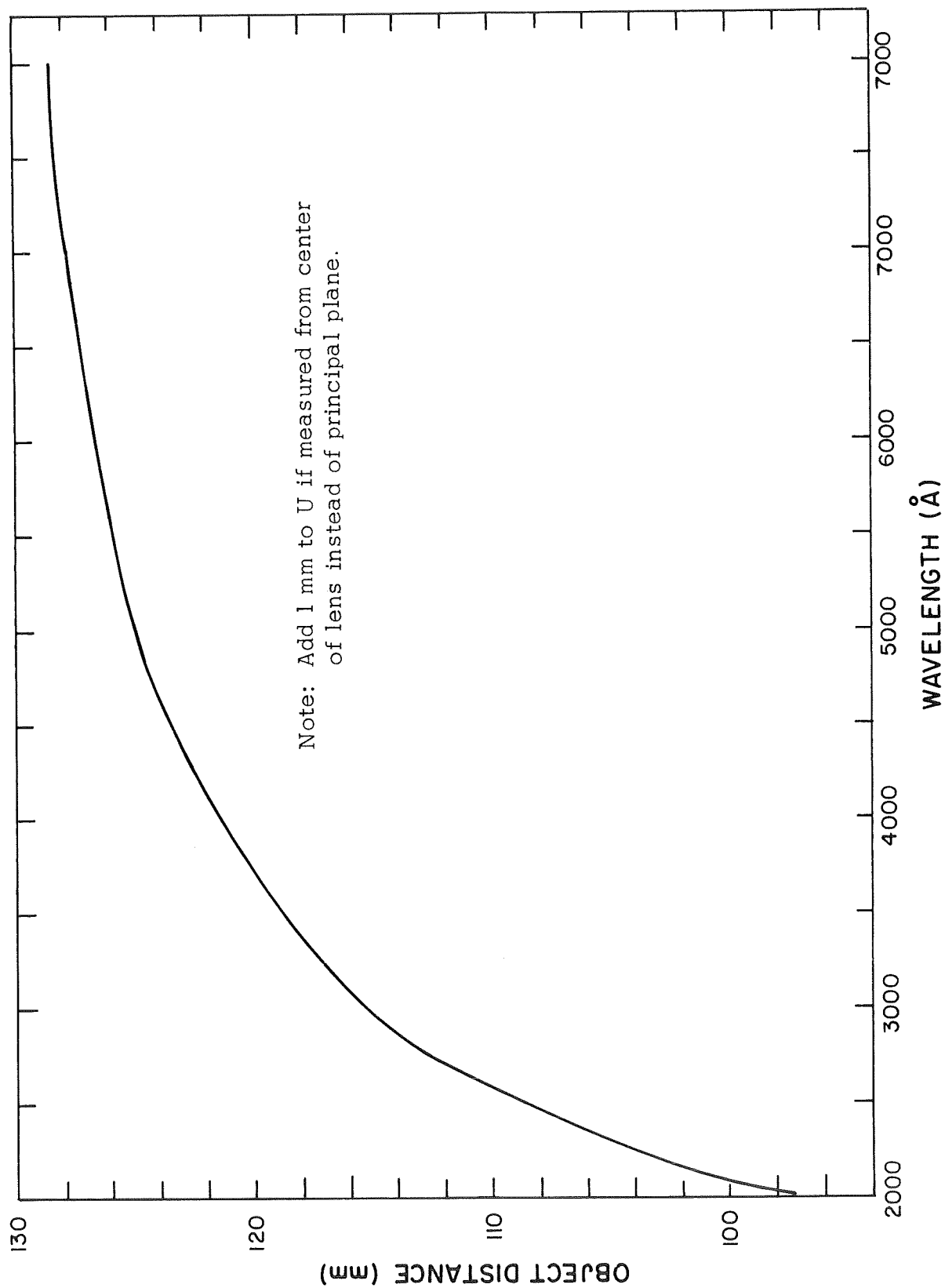


Figure 15 U vs λ

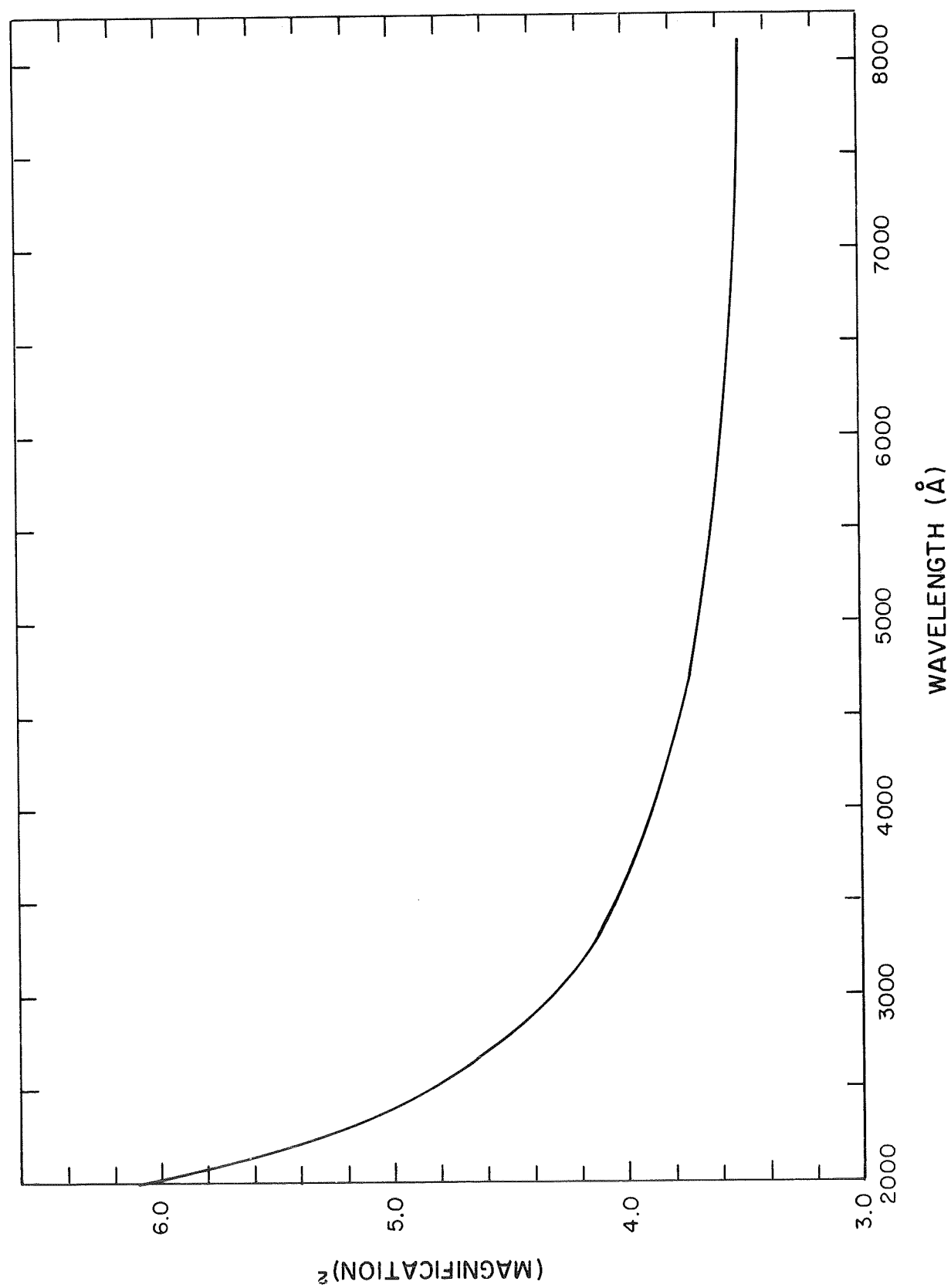


Figure 16 m^2 vs λ

is much higher than the blue, it is necessary to prefilter for calibrations below about 4000 Å in order to reduce excessive scattered light levels inside the monochromator. This is done with a set of UV bandpass filters, for which the transmission at any wavelength must be taken into account. (3) The lenses and mirrors of the relay optics introduce transmission and reflection losses. Lens losses can be accurately computed from the known properties of quartz and the lens dimensions. The mirror losses were determined empirically. Description of the methods follow:

(a) Lens losses:

The light losses due to a glass lens are of two types: (1) reflection losses at both surfaces, and (2) absorption losses in the glass itself. The fractional transmission for normal incidence at a glass-air interface is given by

$$T_R = 1 - \left(\frac{n - 1}{n + 1} \right)^2 \quad (31)$$

where n is the refractive index of the glass. The transmission through a thickness t of glass is

$$T_A = e^{-\alpha t} \quad (32)$$

where α is the absorption coefficient of the glass. Both n and α are wavelength dependent for quartz, and values may be found in optical materials handbooks. The net transmission of a two-lens system (4 glass-air interfaces), if we assume normal incidence, is then given by

$$T = e^{-\alpha (t_1 + t_2)} \left[1 - \left(\frac{n - 1}{n + 1} \right)^2 \right]^4 \quad (33)$$

where t_1 and t_2 are mean thicknesses of the two lenses. This function was evaluated for the two-lens optical relay system used for calibration. The results are plotted vs. wavelength in Figure 17.

The absorption coefficient α is essentially zero above 3000 Å, and even at shorter wavelengths the residual uncertainty due to using an assumed, average optical thickness is completely negligible. Estimates were also made of the errors introduced because the light is not really normally incident at the lens surface. When an average is taken over the whole surface of the lens, the assumption of normal incidence is good to within about 0.1%.

(b) Mirror Losses:

The net reflectivity of the two-mirror system was measured at a number of discrete wavelengths by the method illustrated in Figure 18. The two mirrors were first mounted on a fixture that could be quickly installed on the monochromator entrance port. Mercury and helium discharge lamps were then used to uniformly illuminate (from a comparatively large distance) a diffusely reflecting MgO screen large enough to completely fill the monochromator field at a distance of 2' or 3'. (Since the field is filled with a uniform light source, the distance is unimportant and can be changed without affecting the signal). Next, the monochromator was tuned to select one of the many spectral line outputs and two signal measurements were made: one viewing the MgO screen directly, the other viewing it off

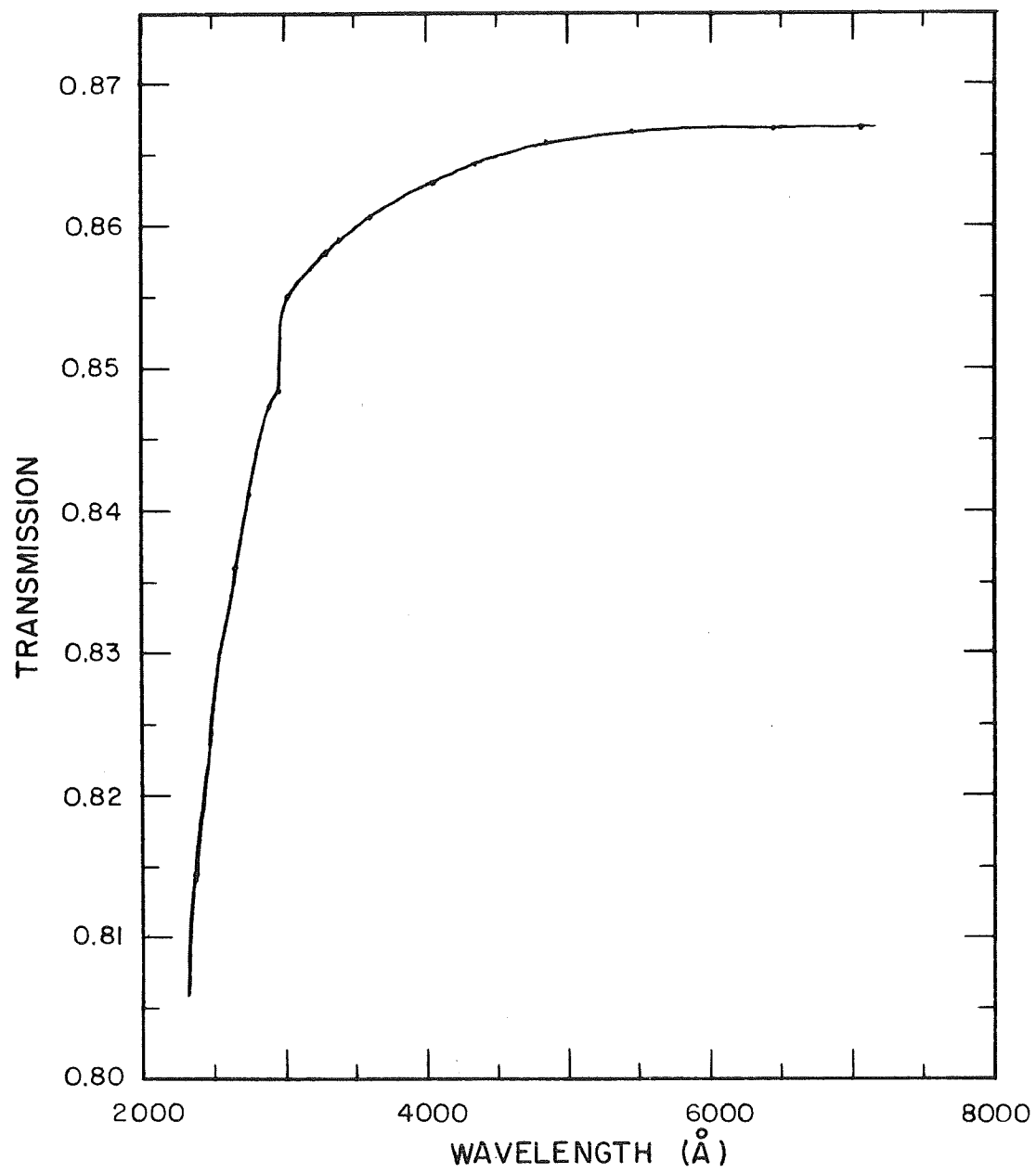


Figure 17 Two-Lens Transmission Function

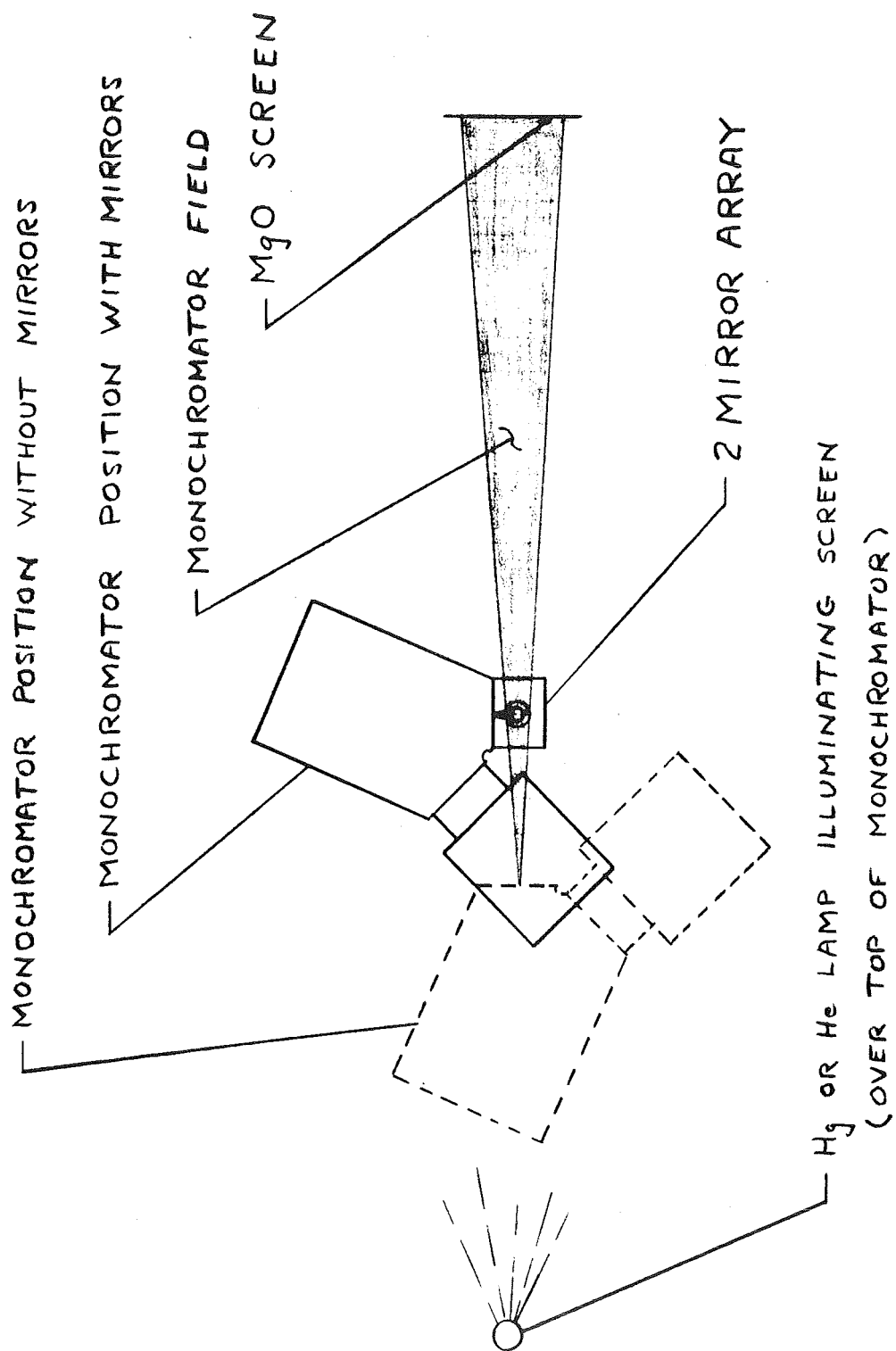


Figure 13. Mirror Reflectance Measurements

the two-mirror system. The ratio of these measurements gives the net reflectivity at that wavelength. Data were taken at spectral lines from 2270 Å to 7280 Å. Results are given in Figure 19, and are substantially in agreement with published data for SiO overcoated aluminum mirrors (Ref. 20).

2.7 Second Optical/Calibration System

The functions of the optical system associated with the second collision region are unchanged, and are performed by the same generalized components: a fore-optics system, a monochromator, and a calibration system. The revised system is illustrated in Figure 20.

2.7.1. Fore-optics.— The basic geometry of the fore-optics system is much the same as that of the optical system described previously (see Figure 13), but the lens and 45° mirror are replaced by an ellipsoidal mirror that performs the functions of both of the former components. The polarizer is also located in a more favorable position, where it can be completely removed from the optical path.

The mirror is a segment of an ellipsoid of revolution, with the interaction region at one focus and the monochromator entrance slit at the other. The geometry of the mirror and the properties of the ellipsoid are given in Drawing SK-120-3005. Reflective focusing completely eliminates the chromatic aberrations associated with the quartz lenses (this is particularly important for calibration), but the ellipsoid introduces severe off-axis effects (coma) which greatly restrict its utility. The interaction region projects into an hourglass figure on the monochromator entrance slit, and is only well

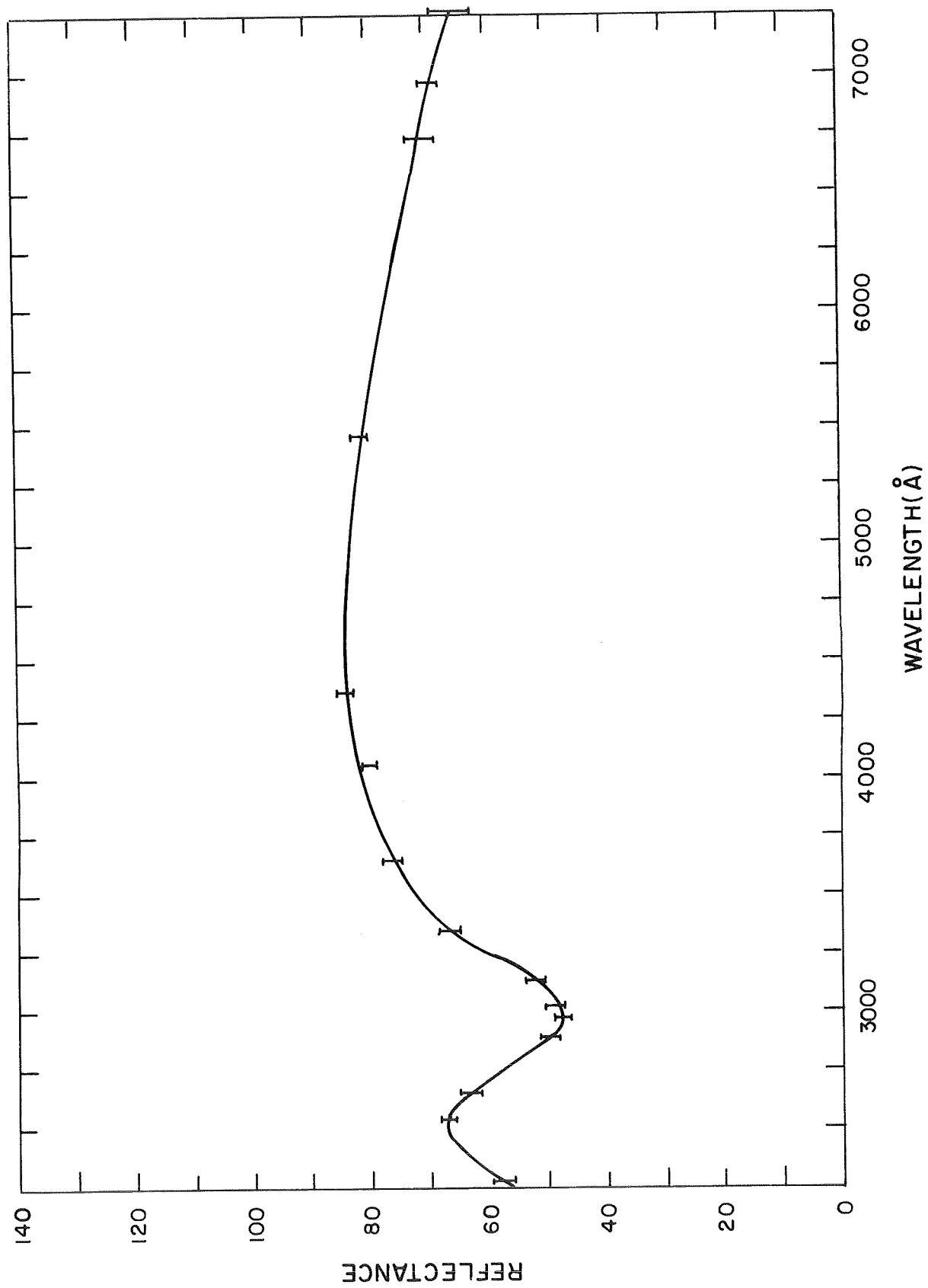


Figure 14 Two-Mirror Reflectance Function

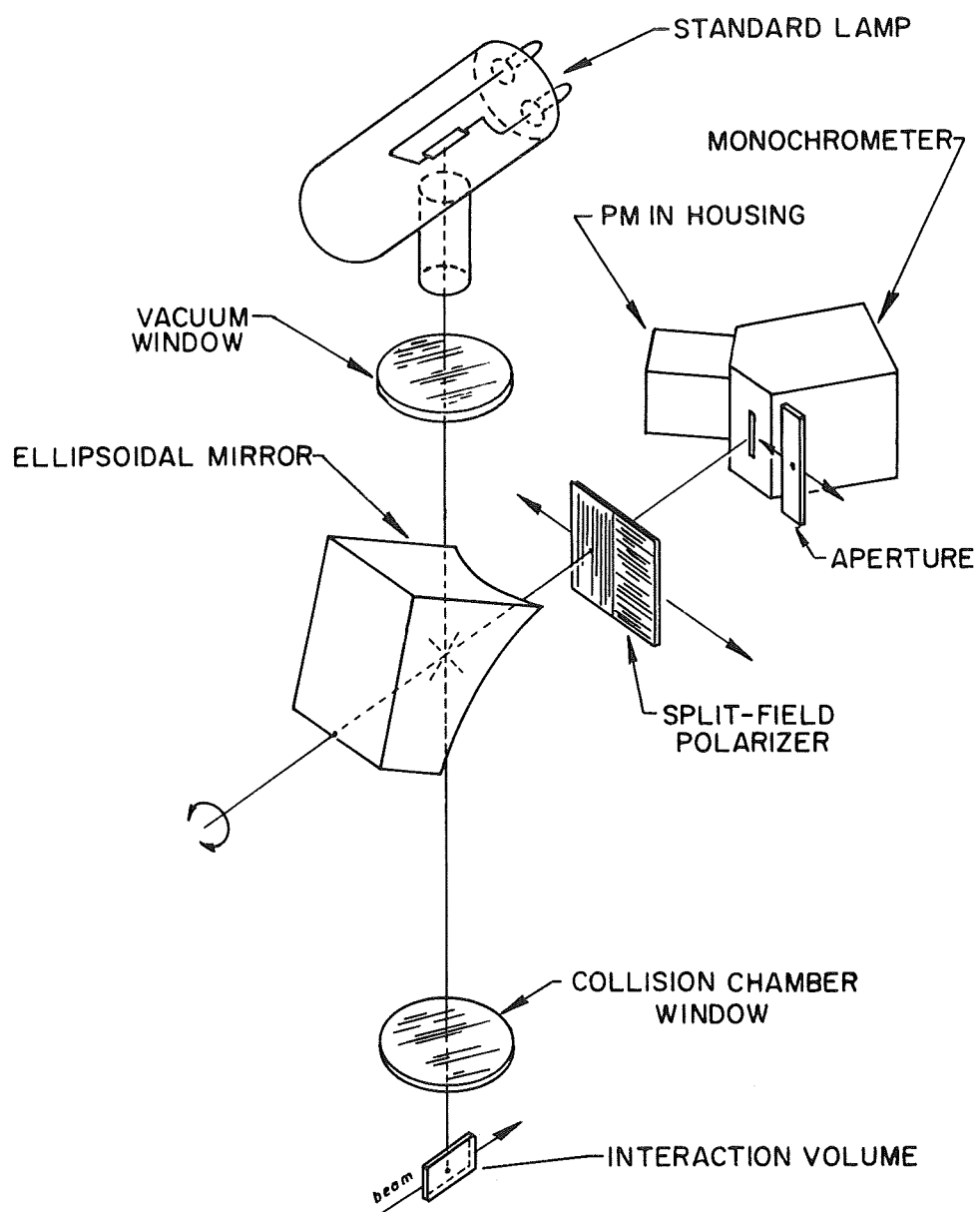


Figure 20. 2nd Optical/Calibration System

focused on a plane tilted at an angle of 30° or more relative to the plane of the slit, as indicated in Figure 20. The magnification of the mirror is not single-valued, but its collection efficiency is approximately $1/3820$ for isotropic radiation.

2.7.2. Monochromator. - No change was made in the monochromator for the second optical system.

2.7.3. Calibration system. - The main difference, in principle, between the two optical systems is the method of calibration. The first system introduced substantial uncertainties into the calibration itself because (1) the transfer losses of an optical relay system had to be determined, (2) there is no way to be sure the calibration light is focused through the center of the interaction region, and (3) the wavelength-dependent magnification factor m^2 that is applied to the aperture size is subject to much error due to small uncertainties in lens dimensions and optical path distance. The system described here has none of these shortcomings. The lamp filament itself is precisely positioned at the same optical distance from the monochromator slit as is the interaction region, and is focused onto the slit by the same ellipsoidal mirror (rotated 180° from its normal position). The windows in both optical paths are identical. The only corrections to be applied are the transmission factors for the bandpass and neutral density filters. Note that the latter can be precisely measured at any wavelength by the light detection system itself.

The limiting aperture for the filament is located nearly in the plane of the monochromator entrance slit, and its area enters directly (i.e., with-

out a magnification factor) into the calculation of the calibration photon rate. The aperture can be scanned across the slit, its position shown by a dial indicator (.001" on the dial indicator = .02 mm at the slit), and vertically along the slit by a micrometer drive. It can be moved completely out of the optical path for collision light measurements.

2.8 Photon Counting

Since the collision experiments to be performed were expected to produce very low light levels, photon counting techniques seemed to hold more promise than more conventional methods which measure some time-average output of a radiation detector. One primary reason for this is that counts can be accumulated for as long a time as necessary, thereby giving longer integration times than are practical for other phase-locked systems. It is also worth noting that counting methods are less susceptible to noise pick-up and instabilities than some other electronic processing techniques. References 21 through 24 discuss in detail the principles and methods applicable to photon counting.

2.8.1 Detector. - An Amperex 56TUV^P photomultiplier tube is used as the photon detector. It has an S20 cathode which responds to wavelengths between the cutoff of the quartz window at 1800 Å and about 8000 Å where the photoemissivity falls to zero. It has a fast, linear-focused dynode structure, giving transit times and pulse widths of about 2 to 4 nanoseconds. The gain at normal operating voltages may be as high as 10^8 , and dark counts (at dry-ice temperature) are about 10 to 20 per second. It is located several inches away from the monochromator exit slit so the emerging light nearly fills the 2" diameter photocathode.

The photomultiplier housing is cooled to -68°C by a dry-ice and alcohol slurry. The interior of the housing is sealed to the exit flange of the evacuated monochromator housing. A quartz window completes the optical path. The housing includes a tube-base assembly wired specifically for this tube. The cathode operates at negative high-voltage, as does a surrounding electromagnetic shield built into the housing. The output is taken directly from the anode, which is shunted by an external $50\ \Omega$ resistor. The output pulse is transmitted through a $50\ \Omega$ coaxial line to the amplifier circuit.

It should be noted that a photomultiplier intended for photon counting, where statistical methods of analysis are used, should not only have high quantum efficiency, low dark current and short pulse width, but should also obey Poisson statistics (or at least the statistical distribution should be well-known). The 56TUVP tube is known to deviate from Poisson statistics (Ref. 21), particularly when cooled. This is in agreement with our observations. Fast bursts of pulses are occasionally seen on a time scale of several seconds, and may be the source of the deviation. Their cause is not known. Numerous checks, made at different count rates and for different total count accumulations, indicate that the uncertainty computed on the basis of the Poisson distribution must be increased by a nearly constant, additional uncertainty of about ± 300 counts.

2.8.2. Electronic processing. - The photomultiplier output produces a voltage pulse of approximate amplitude

$$V = \frac{Q}{C} \approx 0.1\ \text{V} \quad (34)$$

where Q is the charge (in Coulombs) contained in the burst of electrons, and C is the net capacitance of the anode circuit, including the coaxial cable. This voltage pulse has a trailing edge with a time constant

$$\tau = RC \approx 10 \text{ nsec} \quad (35)$$

R being the 50Ω anode resistor.

Pulses of this description are transmitted through about 7 feet of 50Ω coaxial cable to the input (also internally terminated in 50Ω) of a two-stage, fast (2 nsec rise time) pulse amplifier (E.G. & G. model AN101). Each stage has a fixed gain $\times 4$, and the two stages are normally cascaded, giving a total gain $\times 16$. Typical output pulses therefore have amplitudes in the vicinity of 1 or 2 volts.

The amplified pulses are applied to the input of a threshold discriminator (E.G. & G. model T101), which determines the minimum amplitude of pulses that will be counted. All input pulses that exceed the threshold cause shaped, uni-amplitude pulses to appear at the discriminator outputs. The discriminator is normally used in a "dead-time" mode that prevents the circuit from responding to a second pulse occurring within a time established by the length of an external delay cable. All input pulses occurring within the dead-time produce only a single output. It is important that a sufficiently long dead-time be used in order to inhibit certain types of pulse correlation that can be traced to the photomultiplier. These correlation effects are discussed thoroughly in Reference 21.

Two identical discriminator outputs are connected through short lengths of 50Ω coaxial cable to the two inputs of a fast dual scaler (SEN Model

312). Each scaler channel has provision for external gating, which is very important for the synchronous detection system to be discussed in Section 2.9. Thus, the ability of each channel to count the pulses depends on whether the corresponding gate signal is in the "permit" or "inhibit" mode.

Something must be said about the determinations of dead-time, discriminator setting, and optimum photomultiplier high voltage. The methods described in Reference 21 were used, and are based on the premise that pulse correlations lead to inaccuracies in interpretation of results and should be eliminated as much as possible.

Two types of pulse correlation can be eliminated by the use of adequate dead-times. These are (1) correlated after-pulse, and (2) abnormal pulse shapes, due to imperfections in the dynode structure for instance, that may trigger the discriminator more than once. The 56TUV is a particularly good tube in this respect, and a dead-time of 20 nsec can be shown (by statistical methods) to remove most such correlations. RG 58/U cable has a delay time of 5 nsec/meter, so about 13' are required to give a 20 nsec dead-time. Cables 7' long and 4' long exhibited strong correlation that was largely eliminated by using cables 18' and 28' long. The last two gave almost identical results, so 18' apparently produces an adequate dead-time.

For any discriminator trigger level (we use the minimum setting), curves related to integral and differential pulse height distributions can be obtained by plotting counting rate vs. photomultiplier high voltage. If the shapes of curves so obtained are compared to their counterparts computed on the basis of Poisson statistics, the voltage where they begin to diverge,

indicating strong correlation effects, is easily identified.

Data taken to establish an operating high voltage and to determine the necessary dead-time cable length are given in the laboratory notebooks. Reference 21 must be consulted for their interpretation. The recommended values are:

Dead-time \geq 30 nsec (18' of RG 58/U cable).

Discriminator setting = 1.0 (minimum setting).

Photomultiplier high voltage = 1800 V.

2.9 Modulation and Synchronous Detection

The primary ion beam intensity at the collision region may be rather low in some cases, particularly when low energy collisions of heavy, low vapor-pressure materials such as iron are being studied. The situation with neutral beams may be even worse, because of additional losses during the charge-exchange process. Furthermore, since interpretation of the data requires that only single collision processes take place, the total number of photons produced at any wavelength must be relatively small compared to the number of incident ions. We collect these photons with a low geometric efficiency, and with a quantum efficiency that is less than 1% at some wavelengths. For these reasons we must utilize the superior ability of lock-in, or synchronous, detection methods to extract low level signals from noise and background, if we are to realize the maximum sensitivity of the apparatus.

A block diagram of the entire detector system for ions, neutral molecules and atoms, and photons is shown in Figure 21. Many of the individual units and their functions have already been discussed. We now describe their

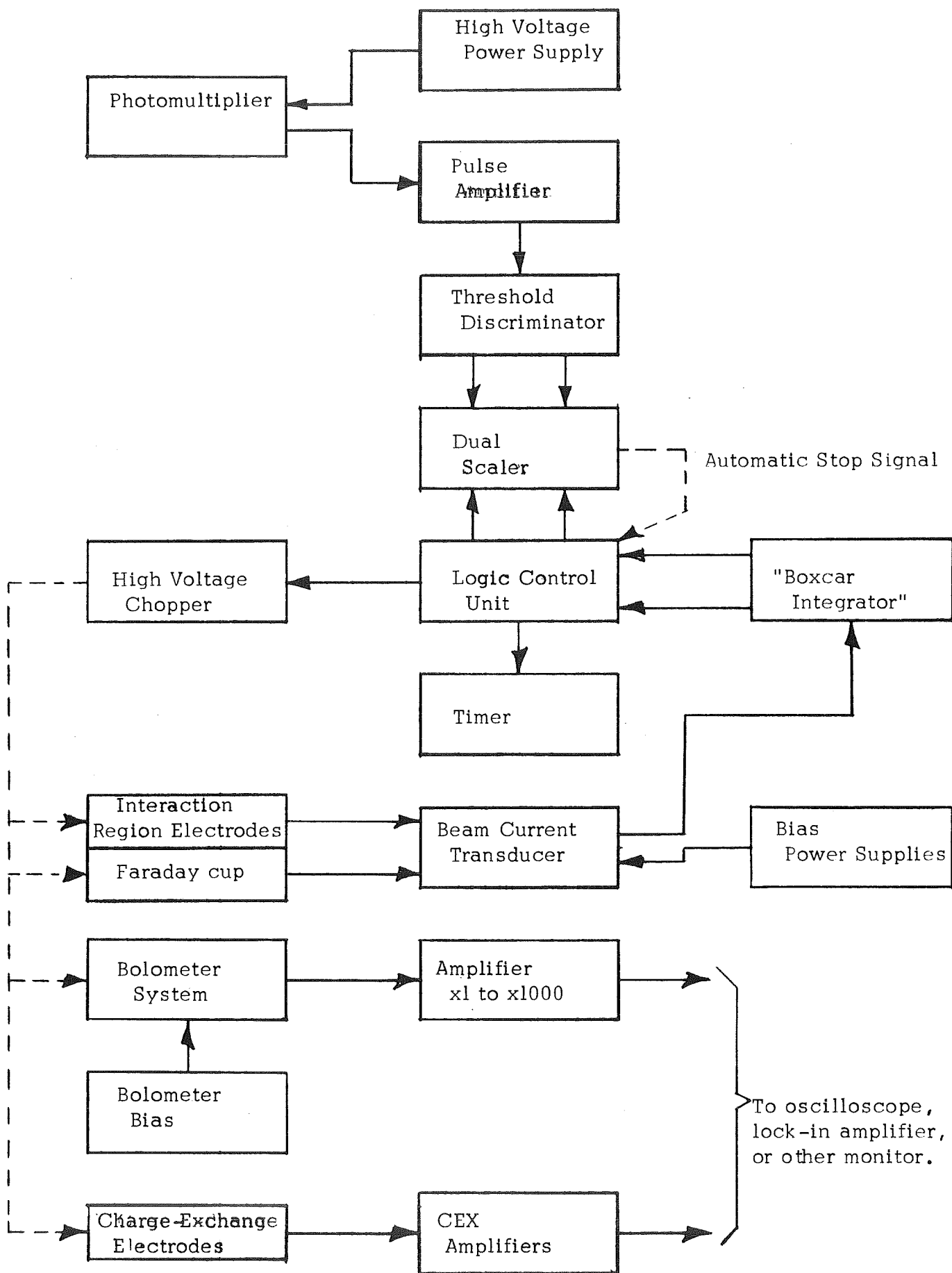


Figure 21. Detector Electronics Block Diagram

logic relationship to each other and, in particular, the equipment required to put synchronous detection into effect.

2.9.1. Boxcar integrator. - The source of control in the time domain, which is our concern here, is the boxcar integrator. This device has two sub-systems that are nearly independent functionally. One is a gated amplifier channel that responds (with an RC time set by a front panel control) to an input signal only when the gate is "open," and holds its last attained output level when the gate is "closed." Thus, it samples and averages only that fraction of a repetitive signal that comes within the duration of the (also repetitive) gate. The other function, more important for our system, is a circuit for multi-mode generation of timing signals, among which are a time-base ramp and a gate (see Figure 22 for the waveforms). The latter controls the amplifier through an internal connection; both are available at panel BNC connectors. The "recurrent" mode is the only one used with this apparatus. In this mode the time-base, or repetition period, is generated within the boxcar integrator, its duration being set by a switch. The gate signal is generated once during each period, with its width and position in the cycle determined by front panel controls.

2.9.2. Logic control unit. - The boxcar integrator determines the timing sequences for the rest of the system via the logic control unit. This device processes the "time-base" and "gate" outputs of the boxcar integrator and produces the waveform shown in Figure 22 to control the other system components.

The positive slope portion of the time-base signal triggers a bi-stable

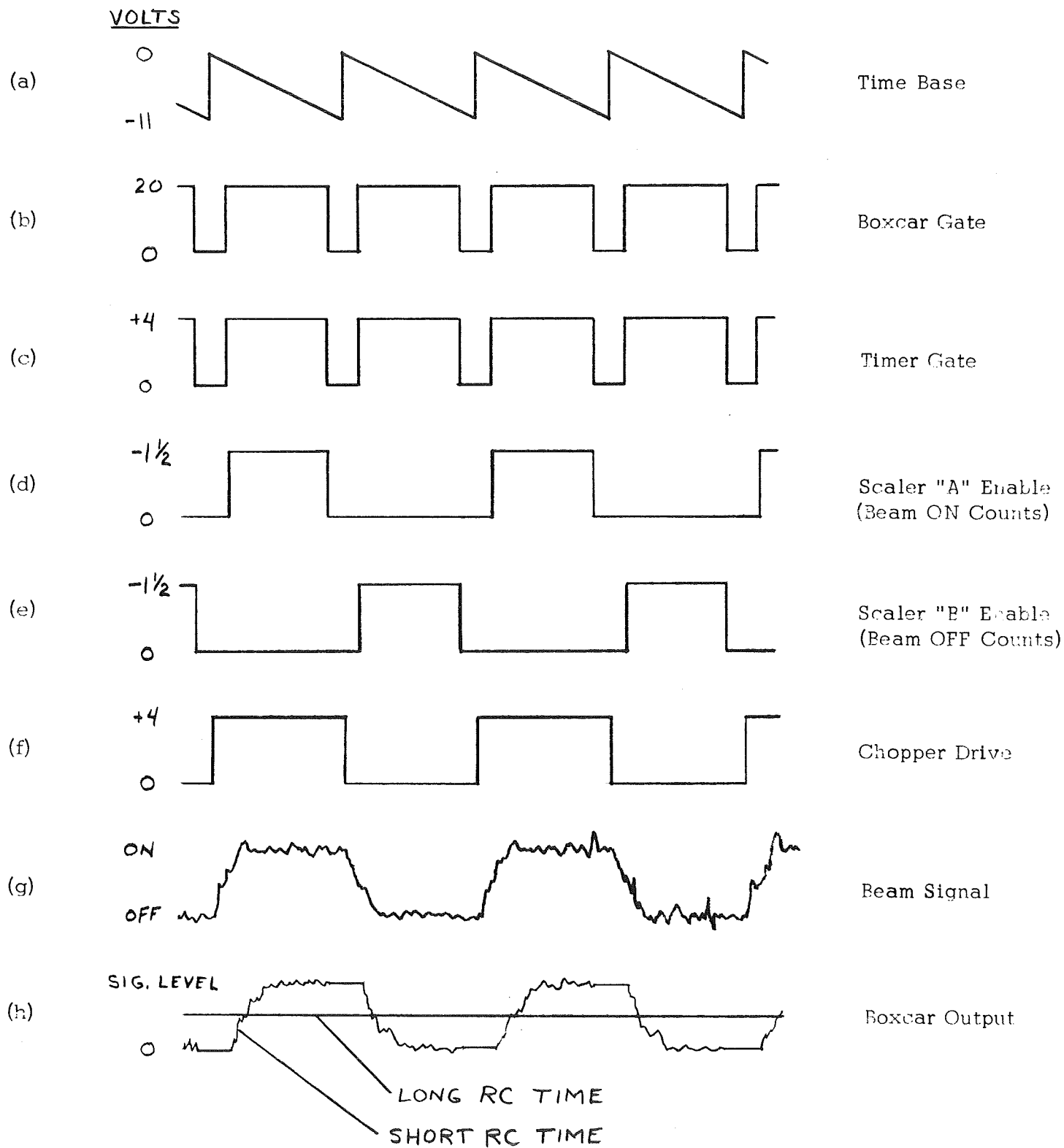


Figure 22. Timing Logic

multivibrator and produces the waveform shown in (f), which is a square wave at half the original frequency. This is the signal used to drive the beam chopper, producing current modulation as shown in (g). Waveform (h) shows this beam current as it might appear (after processing) on the output of the boxcar integrator, for time constants shorter than and longer than the chopping period.

Waveform (c) has the same periodicity as the boxcar gate, but has been processed to give a different signal level suitable to gate a timer (see Figure 21) which then records the total time during which the gates were open. Waveforms (d) and (e) are produced from (c), in turn, by passing it through appropriate electronic gates controlled by (f) or its conjugate. These signals (d and e) are the gate signals for the dual scaler channels. Thus, one channel can record counts when the beam is in the "on" mode, the other records background and noise when the beam is "off".

It should be noted that the boxcar integrator gate causes the beam signal to be sampled during both "on" and "off" phases, thereby indicating only half the true value of the beam on current. The timer, on the other hand, measures the total duration of all gates, thus recording twice the time actually used to accumulate the counts in the "on" channel scaler. These two factors of 2 cancel when the number of ions is computed.

A gate signal would not be required at all if it were not for unsharp rise-and-fall times of the ion beam, as indicated in waveform (g). The ambiguous regions are excluded by setting the gate for the central part of each phase.

Several other features of the logic control unit should also be mentioned. First, it has a mode switch that enables the time-base to be established by an external oscillator (the boxcar integrator), an adjustable frequency internal oscillator, or a manual on-off switch. The beam phase is indicated for all modes by "on" and "off" panel lights. It also has provision to automatically stop any data recording period when a predetermined number of counts appears on either scaler. The control signal is obtained from the appropriate "address" connection at the back of the scaler, and is fed into the logic control unit through a rear panel BNC connector. There is a manual override for this feature.

A description of the logic control unit circuitry is given in Appendix C.

2.9.3. Beam chopper. - Although the beam chopper is functionally part of the ion beam control system, it is logically associated with the synchronous detection system and is discussed here. Its purpose is to turn the beam on and off in phase with the time-base output of the logic control unit. It does this by processing the time-base signal to control the voltage applied to the 1st and 3rd einzel lens electrodes.

The heart of the chopping circuit is shown in Figure 23. The lens control power supply output (refer to Figure 2) is attached to terminals 1 and 2. Its output, minus 400 V (dropped by two 1N3105A zener diodes), is applied to the voltage divider input, terminals 3 and 5. The 0.8 tap from the divider is brought into the chopper circuit at terminal 4. The function of the chopper is to provide an output which alternates in potential between

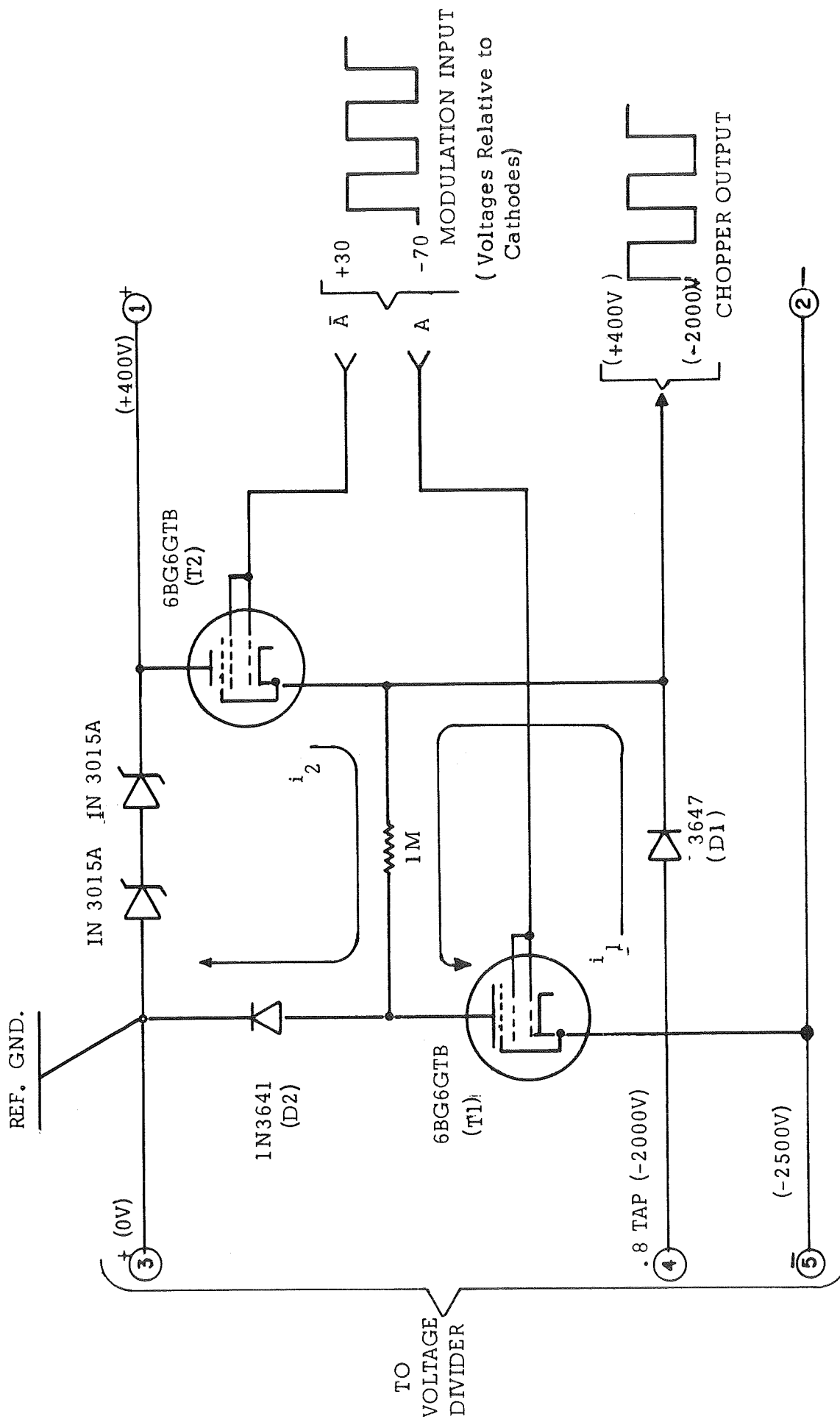


Figure 23. High Voltage Modulator

those of terminals 1 and 4, which are reflecting and focusing potentials respectively. This is done by applying a modulation signal A and its complement \bar{A} to the grids of the two tubes T_1 and T_2 , so they alternately conduct and turn off. When T_1 conducts, high voltage diode D_1 is forward biased and the output is at the potential of terminal 4. When T_2 is conducting, it drops only a small voltage and the output rises close to terminal 1. In this case D_2 is forward biased and D_1 is cut off. The currents through the tubes are i_1 and i_2 respectively. Typical operating voltages are indicated, measured relative to the plasma potential. The circuit shown floats with respect to earth ground at a voltage determined by the beam potential power supply. A description of the chopper circuit is given in Appendix D.

3.0 PROCEDURES AND ANALYSIS

In this section we review the procedures that must be followed to measure the necessary quantities, and the computations by which absolute cross-sections are determined from them. The time required for a complete experiment depends strongly on the obtainable beam intensity, the cross-section for the process, and the desired precision of measurement. In general, eight hours of operation is adequate to start up the apparatus, perform the necessary measurements at several (perhaps 10) beam energies, and calibrate the optical system. Several days of operation may be necessary to complete a set of measurements with a sufficient number of energies to observe any structure that may occur.

3.1 Operational Procedures

Because any particular experiment will introduce its own complexities into the operating procedure, it is not possible to describe all procedures in detail. Instead, we shall list the principal steps that must be followed for most experiments. These procedures are intended to be supplemented by reference to the instruction manuals for all pertinent components. It is assumed that the system is evacuated and that all preliminary work for a particular experiment has been done.

3.1.1 Obtain ion source plasma. -

- (a) Turn on water to ion source and magnet.
- (b) Switch ion source rack to "interlock" position.
- (c) Switch the beam potential supply to some low voltage (1V) so the plasma chamber has a defined reference level.

- (d) Apply 100V to 150V anode potential.
- (e) Increase filament current until emission is observed by current drawn from the anode power supply (several ma.).
- (f) Turn up plasma chamber vapor pressure (either with the heater or the gas leak valve) until the pressure is $\approx 1 \times 10^{-5}$ torr in the source chamber.
- (g) Turn the solenoid current to about 1 ampere.
- (h) If no plasma is obtained at this time, it is probable that the pressure or the filament current is too low. Adjust accordingly.
- (i) Reduce the anode potential to its desired operating value.
- (j) Adjust the ion source controls for a stable plasma, using a low filament current and plasma pressure if possible.

3.1.2 Obtain an ion beam at the Faraday cup. -

- (a) Turn the lens power supply to give the desired analyzer voltage (recall that the chopper drops 400V, and the analyzer energy is 0.8 times the input potential at the voltage divider).
- (b) Adjust the beam potential power supply to give the desired beam energy.
- (c) Make sure the chopper is in either a dc beam "on" or a chopped mode (this requires that the units in the detector electronics rack be switched on).
- (d) Observe the output of the beam current transducer on an oscilloscope.
- (e) Turn up the analyzer field until a signal is observed. Check the magnetic field and Figure 7 to be sure it is the desired mass.

- (f) Adjust all plasma, ion lens and beam alignment parameters for the best collimated beam. This step requires patience and a certain degree of acquired skill.
- (g) Check the beam collimation by measuring currents at various electrodes of the interaction region assembly. Correct, if necessary, by adjusting the retarding lens.
- (h) Apply the signal to the boxcar integrator and record its output. Check the zero level when any gain or sensitivity levels are changed.

3.1.3 Obtain a neutral beam (bypass this item if ion-neutral collisions are to be studied). -

- (a) Turn on the CEX amplifiers, including bias and deflection voltages. Do not remove the deflection voltage when the bolometer is in position and an ion beam is running.
- (b) Check to see that there is no residual ion current at the Faraday cup or entering the collision region.
- (c) Turn on the bolometer amplifier power and slowly turn up the bolometer bias to - 550V in steps not exceeding 100V each.
- (d) Rotate the bolometer into position.
- (e) Open the exchange gas leak valve until the best neutral beam intensity is obtained, as determined by the bolometer signal.
- (f) Calibrate the bolometer by measuring CEX currents i_1 , i_2 , and i_3 as described in Section 2.4.2.

3.1.4 Prepare the counting system. -

- (a) Fill the photomultiplier housing with crushed dry ice.
- (b) Turn the photomultiplier high-voltage to 1800V. Check the output current of the photomultiplier to see that it does not exceed 1 mA.
- (c) Using a two (or more) trace oscilloscope, adjust the position and width of the gate to correspond to the well-defined "on" and "off" portions of the ion beam.
- (d) If spectrum scans are to be done, the photomultiplier output should be observed with an appropriately tuned phase-sensitive detector, instead of the counting electronics.

3.1.5 Prepare interaction region. -

- (a) Adjust bias voltages to suppress secondary electrons.
- (b) Open target gas leak valve until some attenuation of the incident beam is observed.

3.1.6 Prepare the monochromator. -

- (a) Using zero order, align the optical system for peak signal.
- (b) If spectra are to be measured, adjust slits for required resolution and scan the desired range. Scan speed, slit width and detector integrating time must all be compatible (e.g., if the integrating time is 10 sec and the slits are set for 5 \AA^0 resolution, a scan speed of 50 \AA per minute is too fast).
- (c) Tune the monochromator to the wavelength for which a cross-section is to be measured.

- (d) Increase the slit widths until no further increase of signal is seen. If there is another spectral line nearby, it is necessary to use narrower slits and absolute cross-section measurements are difficult.

3.1.7 Record the necessary data (quantities and parameters to be recorded are summarized in Section 3.2). -

3.1.8 Calibrate. -

- (a) Everything except the detector electronics may be turned off during calibration.
- (b) Referring to Figure 15, set the image distance using the scale on the side of the aperture carrier.
- (c) Turn up the lamp current until the filament is incandescent and focus it on the aperture.
- (d) Open the shutter and use the signal to verify that the optical system is aligned for calibration and that the entrance slit is large enough to transmit the whole calibration image.
- (e) Install the necessary amount of neutral density attenuation, and band pass filters if required.
- (f) Increase the lamp current to the value for which it was calibrated (Figure 7).
- (g) Count long enough to obtain good statistics, and record both time and number of counts.
- (h) Without changing the slit widths, replace the tungsten ribbon lamp by a line source and scan a spectral line of a wavelength near that measured. The bandwidth can be determined from the area under the curve.

3.2 Evaluation of Cross-Sections

This section summarizes the quantities which must be measured to determine an emission cross-section under any set of experimental conditions, and the computational procedures that are used to evaluate the cross-sections from the data.

3.2.1 Required data. - There are four types of information which should be recorded to document any experiment. They are (1) the experimental conditions more-or-less incidental in relation to the measurements being made, (2) the experimental parameters which are changed in a systematic way from one set of measurements to another, (3) the actual data from which an unknown quantity (in this case a cross-section) may be computed via a theoretical relationship and (4) calibration data. The quantities falling into each of these four categories are listed below:

1. Experimental conditions:

- (a) ion source operating conditions
- (b) ion lens operating conditions
- (c) vacuum chamber pressure
- (d) analyzer field (and current)
- (e) monochrometer slit sizes and grating
- (f) photomultiplier high voltage
- (g) detector system operating conditions (e.g., discriminator level, time-base period, gate width, amplifier gain)
- (h) collision region bias voltages

2. Experimental parameters:

- (a) system (e.g., $\text{Fe}^+ + \text{N}_2$)
- (b) transition/wavelength
- (c) beam energy
- (d) polarization axis

3. Experimental data:

- (a) incident beam current (i.e., with no target gas)
- (b) beam current stability (monitored during run with target gas)
- (c) target gas pressure (also monitored for stability)
- (d) target gas temperature
- (e) "beam on" counts (C)
- (f) "beam off" counts (C_0)
- (g) counting time (t)

4. Calibration:

- (a) lamp current
- (b) lamp radiance at tuned wavelength
- (c) aperture area
- (d) magnification factor m^2
- (e) transmission factors of lenses, mirrors and filters
- (f) slit widths during calibration
- (g) calibration counting time (t_c)
- (h) calibration counts (C_c)

3.2.2 Computations. - Since the optical systems of the apparatus were designed to have the same transfer efficiency for both interaction and calibration light, the interaction photon flux at right angles to the beam (the

polar angle of observed light is $\theta = 90^\circ$ is given by

$$\varphi_{\lambda}^{\parallel, \perp} (90^\circ) = \frac{S^{\parallel, \perp}}{S_c} K_{\lambda \sigma} \frac{R_{\lambda}}{2} A \left[\frac{\int_0^\infty \tau(\lambda) d\lambda}{\tau(\lambda_0)} \right] \frac{\text{photons/sec}}{\text{ster}}, \quad (36)$$

where S = interaction light count rate

S_c = calibration light count rate

A = calibration aperture area

R_{λ_0} = calibration lamp spectral radiance at wavelength λ_0

K_{λ_0} includes all the transfer functions of the calibration optics, including conversion of units for R_{λ} from $\mu \text{ watts/mm}^2 \cdot \text{ster} \cdot \text{nm}$ to $\text{photons/sec} \cdot \text{mm}^2 \cdot \text{ster} \cdot \text{\AA}$.

The factor in brackets has the dimensions of wavelength (\AA) and is, by definition, the system bandwidth. It is simply the area (in arbitrary units) under the transfer function curve for the light detection system normalized to $\tau(\lambda_0)$ (in the same arbitrary units). The transfer curve may be obtained by scanning the monochromator across a spectral line at or near λ_0 . This factor is discussed in detail in the laboratory notebooks. The symbols \parallel and \perp indicate that the observed polarization direction is parallel to or perpendicular to the beam axis, respectively. Only half the lamp output R_{λ} is applicable to each polarization, since the calibration light is assumed to be unpolarized and half its output is therefore removed by the polarizer in each case. The two polarization components of course must obey the relation

$$\varphi(90^\circ) = \varphi^{\parallel}(90^\circ) + \varphi^{\perp}(90^\circ). \quad (37)$$

Equation (36) gives us a means to determine the photon flux per unit solid angle in a particular direction ($\theta = 90^\circ$) relative to the beam axis. If we are to measure the total cross-section for emission of light at wavelength λ_0 , we must have the total photon flux in all directions. This is given by

$$\Phi_{\lambda_0} = \int \varphi_{\lambda_0} d\Omega. \quad (38)$$

We must have an expression for φ_{λ_0} in order to evaluate the integral. Since a collision has azimuthal symmetry about the beam axis, we assume a dipole radiation pattern (see Refs. 25 through 27), where φ_{λ_0} depends only on the polar angle θ and is given by

$$\varphi_{\lambda_0}(\theta) = \varphi_{\lambda_0}(90^\circ) (1 - \Pi \cos^2 \theta). \quad (39)$$

The quantity Π is the polarization, defined by

$$\Pi = \frac{\varphi_{\lambda_0}^{\parallel}(90^\circ) - \varphi_{\lambda_0}^{\perp}(90^\circ)}{\varphi_{\lambda_0}^{\parallel}(90^\circ) + \varphi_{\lambda_0}^{\perp}(90^\circ)}. \quad (40)$$

We now substitute equation (39) into equation (38) and perform the integral, obtaining

$$\Phi_{\lambda_0} = 4\pi \left(1 - \frac{\Pi}{3}\right) (\varphi_{\lambda_0}^{\parallel} + \varphi_{\lambda_0}^{\perp}). \quad (41)$$

Note that if the radiation is unpolarized, $\Pi = 0$ and we have just that total flux we would obtain by assuming isotropic radiation.

It is now necessary to relate the total photon flux to the cross-section for emission of radiation at wavelength λ_0 . We have from Neff (Refs. 13, 28),

$$\Phi_{\lambda_0} = I_0 \frac{\sigma}{\sigma_c} (1 - e^{-\sigma_c nL}) + I_0 \sigma' \left[nL - \frac{(1 - e^{-\sigma_c nL})}{\sigma_c} \right], \quad (42)$$

where Φ_{λ_0} = photons/sec at λ_0

I_0 = incident beam flux (in particles/sec)

σ = emission cross-section for primary collisions

σ' = emission cross-section for secondary collisions

σ_c = charge exchange cross-section

n = particle density of target gas

L = observed path length

The target particle density n is obtained from the perfect gas law, and is

$$n = 0.9657 \times 10^{16} P/T, \quad (43)$$

where P is the pressure (in microns of Hg) and T is the absolute temperature. The effect of secondary processes can be removed by a study of the pressure dependence of Φ_{λ_0} . If we assume that this has been done (or that secondary processes are negligible), the second term of (42) may be set to zero and the remaining expression solved for σ in terms of measured or known quantities.

The result, where we replace the parameter K_{λ_0} by its explicit factors, is then

$$\sigma = 0.507 \times 10^{-8} A m^2 B T_L T_M T_F \lambda_o R_{\lambda_o} \left[\left(\frac{t_c}{C_c} \right)^{\parallel} \left(\frac{C - C_o}{t} \right)^{\parallel} + \left(\frac{t_c}{C_c} \right)^{\perp} \left(\frac{C - C_o}{t} \right)^{\perp} \right] \left(1 - \frac{\pi}{3} \right) \frac{1}{i} \left[\frac{\sigma_c}{1 - \exp \left(- \frac{\sigma_c P L}{T} \times 0.9657 \times 10^{16} \right)} \right] \quad (44)$$

where

A = aperture area (mm²)

m = aperture linear magnification

B = monochromator bandwidth (Å)

$T_{L,M,F}$ = transmission factors for calibration

lenses, mirrors and filters

λ = wavelength (Å)

R_{λ} = lamp radiance (μ watts/ster \cdot nm \cdot mm²)

t_c = calibration count time (sec)

C_c = calibration counts

C = beam on counts

C_o = beam off (background) counts

t = signal counting time (sec)
 i = incident beam current (amperes)
 P = target gas pressure (microns of Hg)
 T = target gas temperature ($^{\circ}\text{K}$)
 L = interaction region length (cm)
 σ_C = charge-exchange cross-section (cm^2)
 Π = signal polarization as defined by
 equation (40)

Note that if the charge exchange cross-section is not large, the second bracketed term reduces to $\frac{1.036 \times 10^{-16} T}{PL}$ and the exact value of σ_C is not required.

4.0 EXPERIMENTS

At several stages of the apparatus development, experiments were done to check its performance and to obtain preliminary information about certain potentially interesting areas of research for which more detailed measurements should follow. The experiments included measurement of the spectral lines produced by Fe^+ + gas target collisions, spectral and cross-section measurements for Ar^+ + Ar collisions, and likewise for He^+ + Ar. Some of these measurements were of sufficient interest to be published. Only brief summaries of the results will be given in this Section, and the publications will be referenced.

4.1 Fe^+ + Gas Target Experiments

Spectra were recorded for the case of iron ions impinging on N_2 , O_2 , air and Ar at several energies. N_2 and O_2 are, of course, present during meteoric collisions, and air was included to verify that its effect under single collision conditions is simply a weighted sum of the results for N_2 and O_2 . Ar was also used as a target gas in order to obtain comparison spectra without molecular bands. The spectra could be interpreted to indicate relative amplitudes and to give a rough indication of the absolute cross-sections involved. They were analyzed to determine what spectral transitions were involved. The results were published in Ref. 29. It is interesting to note that the spectra observed were almost entirely in the UV (2200 \AA to 4000 \AA), and that some of the upper levels are the same as those leading to lines present in meteor spectra between 4000 \AA and 6500 \AA , although none of the latter were detected. Most of the measurements were made at an ion energy of 900 eV, which corresponds to a velocity of 56 km/sec for Fe^+ .

4.2 $\text{Ar}^+ + \text{Ar}$ Experiments

Collisions of $\text{Ar}^+ + \text{Ar}$ were done for two reasons: (1) to check the sensitivity of the apparatus over its whole spectral range and (2) to evaluate a cross-section for a process that had been measured by other workers.

The $\text{Ar}^+ + \text{Ar}$ system produces many spectral lines. In all, over 80 lines were observed and identified at wavelengths between 3000 Å and 8000 Å. The strongest features (after correcting for instrument function) are several Ar I lines above 6000 Å. They belong to multiplets extending into the IR above the detector sensitivity cutoff. Lines of neutral Ar were also observed between 3000 Å and 5000 Å. The great majority of lines were those of Ar II, however, and these were compared with the spectra reported by Neff (Ref. 28) and by Sluyters and Kistemaker (Ref. 30). Although we operate at the same energy as Neff, and with a very similar apparatus, there are many discrepancies between the results. We see many more lines than were reported by him, including several strong lines which he points out are notably missing from his spectra. In general, our results are more nearly comparable with those of Reference 30, which are for energies of 5 keV and above.

The absolute emission cross-section of the 4806 Å line of Ar^+ was measured over the energy range 100 eV to 3000 eV, at a target gas pressure of about 0.8×10^{-3} torr. The results are plotted in Figure 24, where they are compared with the data published in Refs. 28 and 30. The differences may be within experimental uncertainties in this case. It should be noted that Neff's data was calibrated by matching to the extrapolated results of Sluyters and Kistemaker.

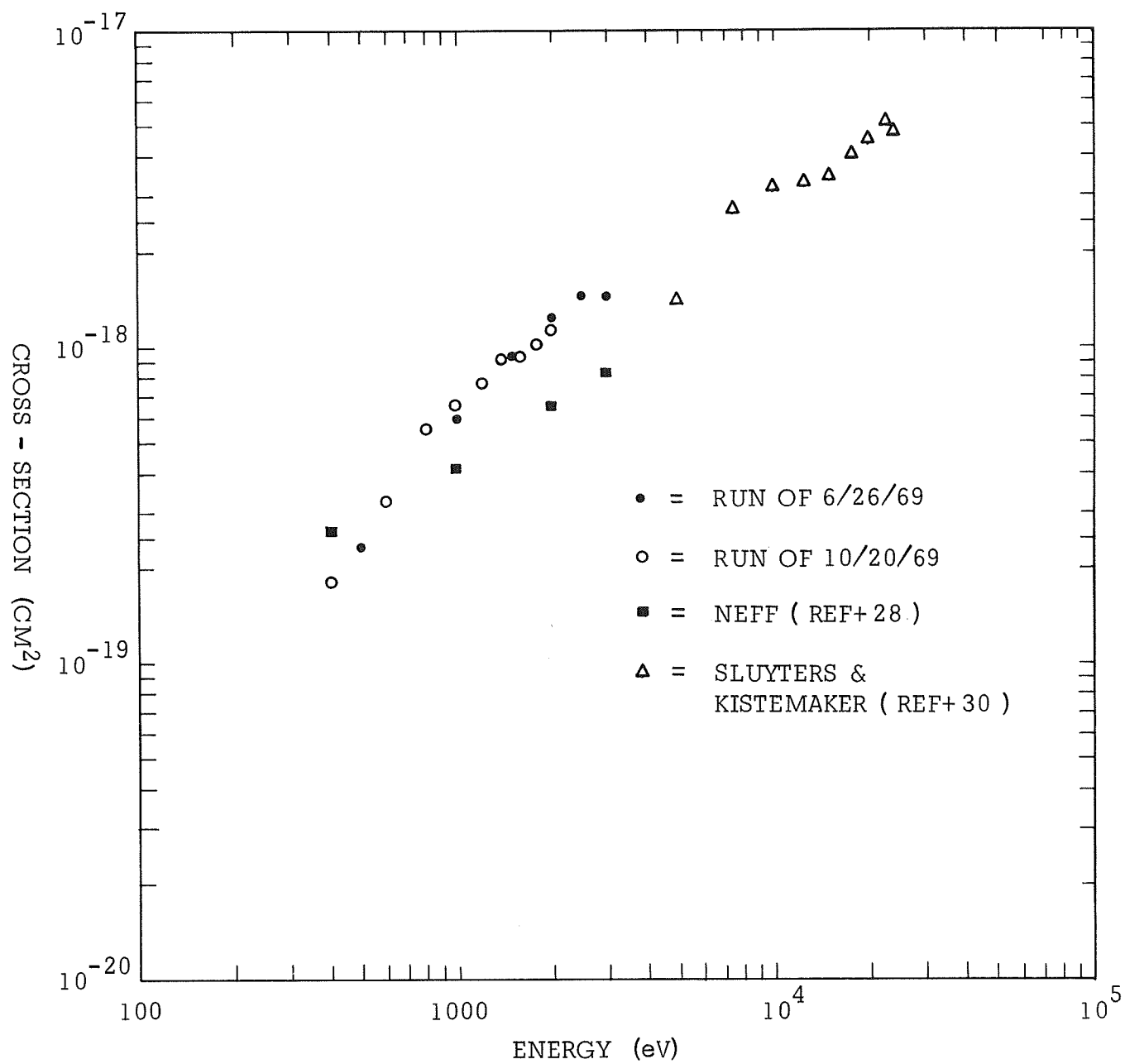


Figure 24. Ar⁺ + Ar Cross-Sections, 4806 Å

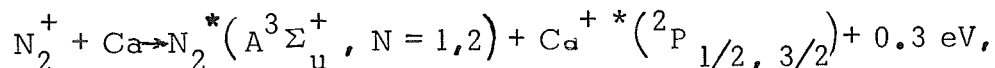
4.3 He^+ + Ar Experiments

A number of experimental runs were made to measure the energy dependence of the cross-section for production of the 4610 \AA and 4765 \AA lines of Ar^+ by He^+ + Ar collisions. The He^+ ion energy ranged from 20 eV (the approximate threshold value for the excitation) to 2000 eV. Data were taken every 5 eV or 10 eV at low energies (to 100 eV), and at 50 eV to 100 eV increments at higher energies. The energy spread of the beam was measured to be ≈ 3 eV at 100 eV beam energy.

The cross-section vs. energy curves show considerable structure, indicating complexities in the collision mechanism that are of theoretical interest (e.g., see Refs. 31 through 33). The results of measurements from 20 eV to 700 eV have been published (Ref. 34). Above 700 eV there is less structure apparent. In the case of the 4610 \AA line, the cross-section reaches a peak at about 900 eV, then decreases monotonically (except for a possible small rise near 1800 eV). The 4765 \AA line cross-section peaks at about 400 eV, then decreases monotonically to 2000 eV where the data terminates.

5.0 $N_2^+ + Ca$ COLLISIONS

There is a possibility that the H and K lines of Ca^+ observed in meteor spectra may be due to reactions of the type (Ref. 35)



if the cross-section for this process is of the order of 10^{-16} cm^2 . It is therefore of interest to measure the cross-section for the production of the H and K lines by $N_2^+ + Ca$ collisions over the range of meteoric energies. The conceptual design of a collision chamber for such measurements is the subject of this Section.

Two methods were considered to obtain the Ca vapor and to determine its concentration. The first, much the simpler in principle, is to place a crucible of Ca in a chamber that can be heated enough to produce the required vapor pressure (about 800°K to obtain 10^{-3} torr Ca vapor pressure). The density of the Ca vapor would be determined by measuring the equilibrium temperature of the chamber, since its vapor pressure is well known (Ref. 36). The chamber would have entrance and exit apertures for the ion beam, similar to the entrance slits of the gaseous target collision chambers, and a quartz window to allow the radiated light to be projected into the optical system. The chamber might be slightly incandescent, due to the elevated temperature, but the dc background so produced would be easily removed by the gated counting technique. Condensation of Ca on the window could be prevented by proper thermal design, but the hot vapor might attack the window chemically.

The other method to provide the Ca vapor for the collisions is by means of a crossed-beam obtained from a high temperature Ca oven. In this case the problems of chemical attack and background light can be avoided,

but they are replaced by problems of determining the Ca density and distribution across the beam. The proposed experimental configuration is shown in Figure 25. The Ca beam would be obtained from a multi-channel oven source surrounded by heat shields. A final collimation aperture is shown in the outermost heat shield adjacent to the N_2^+ beam. Mass flow would be measured by a microbalance, and oven temperature measured by a thermocouple. These two quantities are sufficient to determine the Ca beam particle density, provided the beam velocity can be computed for a multi-channel source (for sample calculations, see Refs. 37 and 38). A shutter in front of the microbalance collector would be opened only when mass measurements were to be made. The interaction volume is indicated. Since neither the ion beam nor the Ca beam would be expected to be uniform, it would be necessary to measure the distributions of each. Preliminary drawings of a Ca oven design are included in the Drawing List.

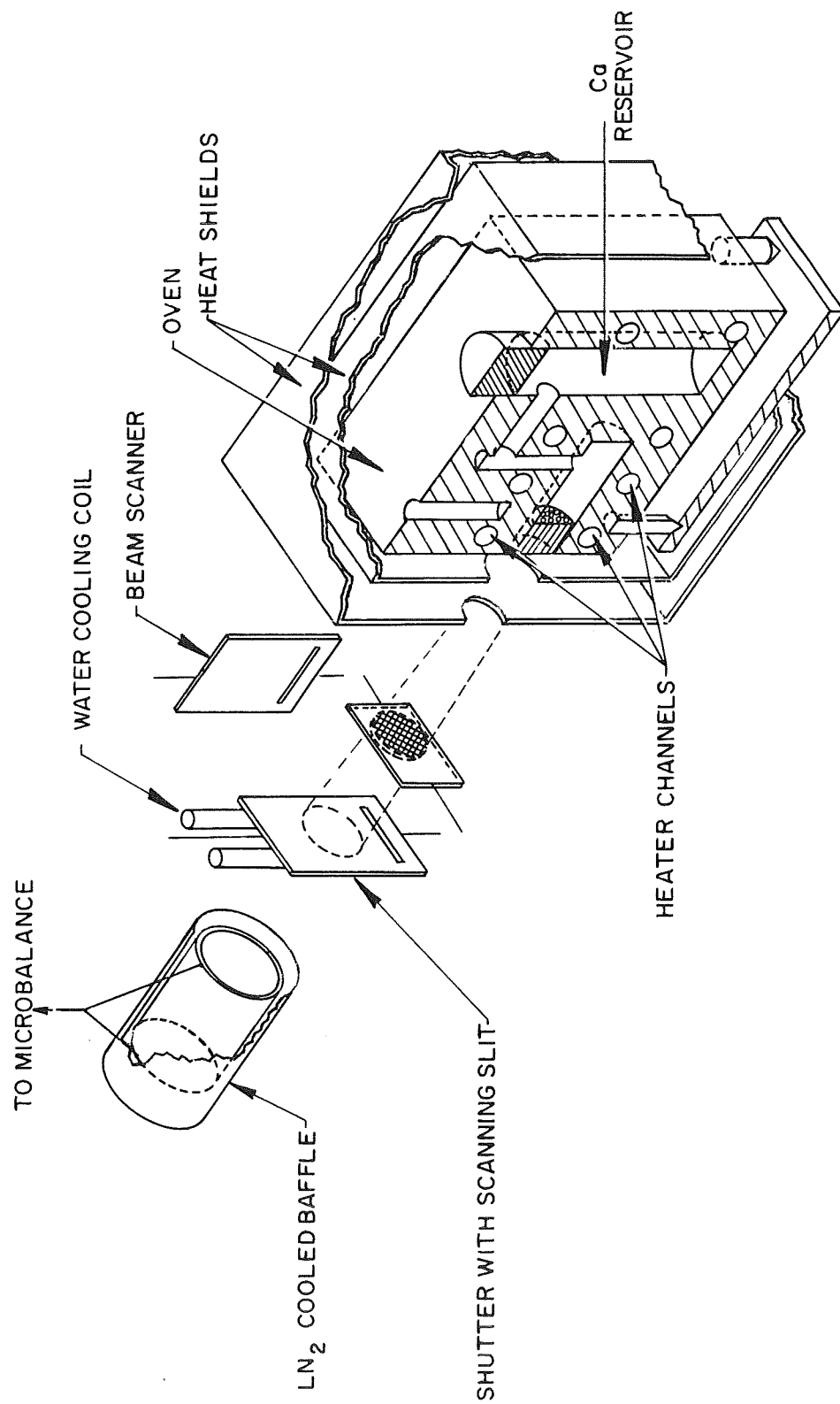


Figure 25. $\text{N}_2^+ + \text{Ca}$ Crossed-Beam Experiment

REFERENCES

1. A.F. Cook, The Nature of Meteoric Radiation, in T.R. Kaiser, ed., Meteors, Spec. Suppl. Journ. Atmosph. and Terr. Phys., Vol 2, Pergamon Press (New York, 1955).
2. K.O. Nielsen, Nucl. Inst. 1, 289 (1957).
3. O. Almen and K.O. Nielsen, Nucl, Inst. 1, 302 (1957).
4. G. Sidenius and O. Skilbreid, E.M. Separation of Radioactive Isotopes, p. 243, Springer-Verlag (Vienna, 1961).
5. I. Chavet and R. Bernas, Nucl. Inst. and Meth. 47, 77 (1967).
6. J.R. Pierce, Theory and Design of Electron Beams, D. Van Nostrand Company, Inc. (New York, 1954).
7. M.D. Gabovich, Plasma Ion Sources (translation), Foreign Technology Division, Air Force Systems Command, Wright-Patterson Air Force Base, Ohio; Document #FTD-MT-65-229.
8. C.F. Giese, Rev. Sci. Inst. 30, 260 (1959).
9. J. Kistemaker, P.K. Rol and J. Politiek, Nucl. Inst. and Meth. 38, 1 (1965).
10. P. Grivet, Electron Optics, Pergamon Press (1965).
11. A. von Engel, Ionized Gases, Clarendon Press (Oxford, 1965).
12. J.E. Jordan and I. Amdur, Jour. Chem. Phys. 46, 165 (1967).
13. S.H. Neff, Thesis, Harvard University (1963).
14. Anon., Design, Development and Experimental Verification of Atomic Beam Apparatus, Interim Scientific Report for Contract NAS 12-143, American Science & Engineering, Inc., Cambridge, Mass., Report No. ASE-1946.
15. H.S.W. Massey and E.H.S. Burhop, Electronic and Ionic Impact Phenomena, Clarendon Press (Oxford, 1952).

16. N.G. Utterback and G.H. Miller, Rev. Sci. Inst. 32, 1101 (1961).
17. J.E. Jordan and I. Amdur, in Molecular Beams, J. Ross editor, Interscience (New York, 1966).
18. F.A. Jenkins and H.E. White, Fundamentals of Optics, McGraw-Hill (New York, 1957).
19. G.R. Harrison, R.C. Lord, and J.R. Loofbourow, Practical Spectroscopy, Prentice-Hall (New York, 1948).
20. G. Haas, Mirror Coatings, in Appl. Optics and Optical Engineering, Vol. 3, Academic Press (New York, 1957).
21. R. Foord, R. Jones, C.J. Oliver, and E.R. Pike, Applied Optics 8, 1975 (1969).
22. G.A. Morton, Applied Optics 7, 1 (1968).
23. R.R. Alfano and N. Ockman, Jour. Opt. Soc. 58, 90 (1968).
24. J.K. Nakamura and S.E. Schwarz, Applied Optics 7, 1073 (1968).
25. J. Van Eck, et. al., Physica 30, 1171 (1964).
26. W.L. Fite and R.T. Brackmann, Phys. Rev. 112, 1151 (1958).
27. I.C. Percival and M.J. Seaton, Phil. Trans. Roy. Soc. London 251, 113 (1958).
28. S.H. Neff, Astrophys. Jour. 140, 348 (1964).
29. M.S. Longmire, H.S. Hoffman, and R.D. Swift, Bull. Am. Phys. Soc. 14, 610 (1969).
30. Th. J.M. Sluyters and J. Kistemaker, Physica 25, 1389 (1959).
31. H. Rosenthal and H.M. Foley, Phys. Rev. Lett. 23, 1480 (1969).
32. S.H. Dworesky and R. Novick, Phys. Rev. Lett. 23, 1484 (1969).
33. S.H. Dworesky, R. Novick, W.W. Smith, and N. Tolk, Phys. Rev. Lett. 18, 939 (1967).

34. M. Lipeles, R.D. Swift, M.S. Longmire, and M.P. Weinreb, Phys. Rev. Lett. 24, 799 (1970).
35. H.S. Hoffman and M.S. Longmire, Nature 218, 858 (1968).
36. A.N. Nesmeyanov, Vapor Pressure of the Chemical Elements (trans.), Elsevier (New York, 1963).
37. N.F. Ramsey, Molecular Beams, Clarendon Press (Oxford, 1956).
38. P. Kusch and V.W. Hughes, Handbuch der Physik 37/1, J. Springer (Berlin, 1959).

APPENDIX A: DRAWING LIST

| | |
|----------|--------------------------------------|
| 120-3005 | ELLIPSOIDAL MIRROR GEOMETRY |
| 120-3011 | PLAN VIEW UPPER |
| 120-3012 | PLAN VIEW LOWER |
| 120-3014 | JACK LEG |
| 120-3015 | VALVE SHAFT EXTENSION |
| 120-3016 | MTG. BRACKET 4" PUMP |
| 120-3017 | COVER 4 " PUMP |
| 120-3018 | ASSY. SOURCE LINE |
| 120-3019 | FLANGE SOURCE LINE |
| 120-3020 | ADAPTER BLOCK |
| 120-3023 | GAS HANDLING MON SYS. (SCHEMATIC) |
| 120-3024 | SUPPORT RODS |
| 120-3025 | MC LEOD GAUGE SHELF |
| 120-3026 | MC LEOD GAGUE SUPPORT RODS |
| 120-3031 | ASSEMBLY HIGH TEMP ION SOURCE |
| 120-3032 | CATHODE CAP GRAPHITE |
| 120-3033 | ANTI-CATHODE CAP GRAPHITE |
| 120-3034 | ANODE GRAPHITE |
| 120-3035 | CATHODE CAP MOLYBDENUM |
| 120-3036 | ANTI-CATHODE CAP MOLYBDENUM |
| 120-3037 | ANODE MOLYBDENUM |
| 120-3038 | HEATHER SPOOL |
| 120-3039 | INSULATOR ANTI-CATHODE |

APPENDIX A:

DRAWING LIST

| | |
|----------|-----------------------------|
| 120-3040 | INSULATOR CATHODE |
| 120-3041 | CATHODE SPACER |
| 120-3042 | INSULATING BUSHING HTR. |
| 120-3043 | INSULATING BUSHING FILAMENT |
| 120-3044 | FILAMENT SUPPORT |
| 120-3045 | SPECIAL HARDWARE |
| 120-3046 | RETAINING NUT |
| 120-3047 | HEAT SHIELD SPACER |
| 120-3048 | HEAT SHIELD DISC, CATHODE |
| 120-3049 | HEAT SHIELD DISC, OUTER |
| 120-3050 | HEAT SHIELDS CYLINDRICAL |
| 120-3056 | POSITIONER ASSEMBLY |
| 120-3057 | POSITIONER DETAILS |
| 120-3058 | BRACKET |
| 120-3059 | P1 REPLACEMENT |
| 120-3061 | JACK SCREW MOUNT |
| 120-3062 | BELLOWS FLANGE |
| 120-3063 | BELLOWS ASSEMBLY |
| 120-3064 | MTG. HOLES SOURCE FLANGE |
| 120-3066 | ASSEMBLY ION LENS |
| 120-3067 | CRADLE FOR LENS ASSEMBLY |
| 120-3068 | EXTRACTION ELECTRODE |
| 120-3069 | ELECTRODE MOUNT |
| 120-3070 | TIE ROD |

APPENDIX A: DRAWING LIST

| | |
|----------|--------------------------------|
| 120-3071 | EINZEL LENS ELEMENTS |
| 120-3072 | SUPPORT RING |
| 120-3073 | SPACER SUPPORTING RING |
| 120-3074 | QUADRUPOLE FIRST SET ELEMENT A |
| 120-3075 | QUADRUPOLE INSULATING RING |
| 120-3076 | QUADRUPOLE ELEMENT 2nd SET |
| 120-3077 | INSULATING SLEEVE |
| 120-3078 | SPRING GUIDE |
| 120-3079 | RETAINING RING |
| 120-3080 | RING GEAR |
| 120-3086 | LENS HOUSING TEE |
| 120-3087 | BNC FEED THRU PLATE |
| 120-3088 | ION LENS FEED THRU PORT COVER |
| 120-3089 | MTG. PLATE ION LENS CONNECTOR |
| 120-3090 | PROTECTIVE COVER ION LENS FEED |
| 120-3091 | THRU PINION GEAR |
| 120-3092 | PINION SHAFT SEAL |
| 120-3093 | PINION RETAINER |
| 120-3095 | TOP PORT COVER |
| 120-3098 | DRIFT TUBE MANDRILL ASSEMBLY |
| 120-3102 | BLANK OFF PLUGS |
| 120-3103 | INSULATING SPACERS |
| 120-3104 | INSULATING ALIGNMENT SLEEVE |

APPENDIX A: DRAWING LIST

| | |
|----------|---------------------------|
| 120-3106 | SLIT RETAINER |
| 120-3108 | ASSEMBLY ADJUSTABLE MOUNT |
| 120-3109 | STANDOFF WITH SLOT |
| 120-3110 | THREADED STANDOFF LONG |
| 120-3111 | THREADED STANDOFF SHORT |
| 120-3112 | THREADED ROD "X" ADJUST |
| 120-3113 | THREADED ROD "Y" ADJUST |
| 120-3114 | HANDLE |
| 120-3115 | "X" ADJ. GUIDE FRONT |
| 120-3116 | "X" ADJ. GUIDE REAR |
| 120-3117 | STOP PIVOT PLATE |
| 120-3118 | STOP MAGNET PLATE |
| 120-3119 | SHAFT WHEEL |
| 120-3121 | PIVOT PLATE |
| 120-3122 | "Y" ADJUST PLATE |
| 120-3123 | RETRACTILE PLATE |
| 120-3124 | "Z" ADJ. TRACK NEAR SIDE |
| 120-3125 | "Z" ADJ. TRACK FAR SIDE |
| 120-3126 | ANGLE STANDOFF "Z" ADJUST |
| 120-3127 | MAGNETIC SHIELD FRONT |
| 120-3128 | MAGNETIC SHIELD REAR |
| 120-3133 | ASSEMBLY RETARDING LENS |
| 120-3134 | MTG. PLATE |

APPENDIX A: DRAWING LIST

| | |
|----------|------------------------------|
| 120-3135 | DOVETAIL SLIDE |
| 120-3136 | DOVETAIL RAIL |
| 120-3137 | SLIDE DRIVER |
| 120-3138 | SLIDE BEARING INSULATING |
| 120-3140 | BUSHING CONTROL ELECTRODE |
| 120-3141 | SLIT SUPPORT INSULATOR |
| 120-3143 | SLITS |
| 120-3150 | BELLOWS VACUUM HOUSING |
| 120-3151 | VACUUM HOUSING |
| 120-3152 | TARGET CHAMBER |
| 120-3153 | PORT COVER |
| 120-3154 | WINDOW RETAINER |
| 120-3155 | BEAM ENTRANCE PORT |
| 120-3156 | DOVETAIL TRACK |
| 120-3158 | SOVETAIL SLIDE |
| 120-3159 | SLIT GASKET |
| 120-3160 | ENTRANCE SLIT BACKING |
| 120-3161 | SIDE ELECTRODE |
| 120-3162 | SIDE ELECTRODE MODIFIED |
| 120-3163 | CUP SLIT BACKING |
| 120-3164 | SECONDARY SUPPRESSOR |
| 120-3165 | FARADAY CUP |
| 120-3166 | SLITS |

APPENDIX A: DRAWING LIST

| | |
|----------|--------------------------------------|
| 120-3167 | INSULATING BUSHINGS |
| 120-3168 | MIRROR BRACKET |
| 120-3169 | MIRROR MOUNT |
| 120-3170 | MIRROR RETAINER WITH HINGE |
| 120-3176 | POLARIZER HOUSING |
| 120-3177 | POLARIZER HOLDER |
| 120-3178 | POLARIZER SHAFT |
| 120-3179 | POLARIZER SHAFT BEARING & BUSHING |
| 120-3181 | MONOCHROMATOR SHELF |
| 120-3182 | SHELF SUPPORT |
| 120-3183 | FOOT PADS MONOCHROMATOR |
| 120-3184 | PUMPING LINE |
| 120-3187 | TOP PORT COVER |
| 120-3188 | ADJUSTABLE SHAFT MIRROR |
| 120-3189 | MOUNT BRACKET MIRROR |
| 120-3190 | MIRROR MOUNT |
| 120-3191 | ALIGNMENT HINGE MIRROR |
| 120-3192 | MIRROR RETAINER |
| 120-3193 | FOCUS HUT LENS |
| 120-3194 | FOCUS SCREW LENS |
| 120-3195 | CLAMP NUT, MIRROR ADJUST SHAFT |
| 120-3196 | CLAMP RING LENS FOCUS SCREW |
| 120-3197 | CONDENSER LENS HOLDER |

APPENDIX A: DRAWING LIST

| | |
|----------|--------------------------------|
| 120-3201 | MTG. PLATE PORT COVER |
| 120-3202 | HOUSING |
| 120-3203 | COVER |
| 120-3204 | SHUTTER HOLDER |
| 120-3205 | SHUTTER RETAINER |
| 120-3206 | SHUTTER |
| 120-3207 | SHUTTER SHAFT |
| 120-3208 | RETAINER SHAFT SEAL |
| 120-3209 | POSITIONING BRACKET, MIRROR |
| 120-3210 | MIRROR MOUNT |
| 120-3211 | MIRROR HINGE & RETAINER |
| 120-3212 | ND FILTER HOLDER |
| 120-3213 | ND FILTER RETAINER |
| 120-3214 | SPACER |
| 120-3215 | BRACKET APERTURE & LENS MOUNTS |
| 120-3216 | APERTURE HOLDER |
| 120-3217 | LENS HOLDER |
| 120-3218 | LENS SLIDE |
| 120-3227 | CYLINDER CEX |
| 120-3228 | GRID ASSEMBLY |
| 120-3229 | GASKET |
| 120-3230 | SLITS |
| 120-3231 | SLIT SPACER |

APPENDIX A: DRAWING LIST

| | |
|----------|-----------------------|
| 120-3232 | MOUNTING PLATE CEX |
| 120-3233 | RETAINER EXIT SLIT |
| 120-3234 | ION REMOVER |
| 120-3235 | INSULATING BUSHINGS |
| 120-3236 | DRIVE TUBE BUSHING |
| 120-3237 | DRIVE TUBE CLAMPS |
| 120-3238 | POSITIONER ASSEMBLY |
| 120-3239 | DRIVE TUBE |
| 120-3240 | MTG. PLATE POSITIONER |
| 120-3241 | DRIVE NUT |
| 120-3242 | THRUST PLATE |
| 120-3243 | SPACER THRUST PLATE |
| 120-3244 | PLUG DRIVE TUBE |
| 120-3251 | VACUUM/TARGET CHAMBER |
| 120-3252 | PUMPING SPOOL |
| 120-3253 | BLANKOFF PLATE |
| 120-3254 | ACCESS PORT COVER |
| 120-3255 | PARTITION |
| 120-3256 | DOVETAIL TRACK |
| 120-3257 | INSULATION BEARINGS |
| 120-3259 | DOVETAIL SLIDE |
| 120-3260 | SLIT GASKET |
| 120-3261 | PUSHROD CLAMP |

APPENDIX A: DRAWING LIST

| | |
|----------|--------------------------|
| 120-3262 | PUSHROD INSULATED |
| 120-3263 | BELLOWS DETAILS/ASSEMBLY |
| 120-3264 | POSITIONER PORT COVER |
| 120-3265 | DRIVE NUT |
| 120-3266 | THRUST PLATE |
| 120-3267 | SPACER THRUST PLATE |
| 120-3268 | MOUNT DIAL INDICATOR |
| 120-3270 | PORT COVER DETECTOR |
| 120-3271 | SLIDING PLATE, VERTICAL |
| 120-3272 | SLIDING PLATE HORIZONTAL |
| 120-3273 | RAIL |
| 120-3274 | STAMDOFF |
| 120-3275 | ELEVATED PLATE |
| 120-3276 | DRIVE SCREW ASSEMBLY |
| 120-3277 | THRUST NUT |
| 120-3278 | CLAMP, DIAL INDICATOR |
| 120-3279 | PAD, DIAL INDICATOR |
| 120-3280 | BELLOWS RING ASSEMBLY |
| 120-3281 | TURNTABLE |
| 120-3282 | DETENT/RETAINER |
| 120-3283 | SPACER ROD |
| 120-3284 | DETECTOR MOUNT |
| 120-3285 | FARADAY CUP |

APPENDIX A: DRAWING LIST

| | |
|----------|-----------------------------|
| 120-3286 | BUSHING |
| 120-3287 | SLIT & RETAINER |
| 120-3288 | AMPLIFIER BRACKET |
| 120-3296 | OPTICS HOUSING |
| 120-3298 | APERTURE MOUNT |
| 120-3299 | POSITIONER SLIDING SHAFT |
| 120-3300 | POSITIONER LEVER |
| 120-3301 | GUIDE SLEEVE |
| 120-3302 | CLAMP MICROMETER HEAD |
| 120-3303 | DRIVE SCREW |
| 120-3304 | BRACKET DRIVE SCREW |
| 120-3305 | BRACKET DIAL INDICATOR |
| 120-3306 | POLARIZER TRACK |
| 120-3307 | PUSHROD POLARIZER |
| 120-3308 | PUSHROD PORT POLARIZER |
| 120-3309 | WINDOW/SHUTTER RETAINER |
| 120-3310 | SHUTTER HOLDER |
| 120-3311 | KEEPER ND FILTER |
| 120-3312 | MODIFICATION DIAL INDICATOR |
| 120-3313 | SPLIT FIELD POLARIZER |
| 120-3325 | CHOPPER SCHEMATIC |
| 120-3326 | CURRENT AMPL. WIRING LAYOUT |
| 120-3327 | CURRENT AMPL. LOGIC DIAGRAM |

APPENDIX A: DRAWING LIST

| | |
|----------|----------------------------|
| 120-3328 | LOGIC CONTROL UNIT |
| 120-3329 | CEX AMPL. SYSTEM SCHEMATIC |
| 120-3330 | BOLOMETER SYSTEM SCHEMATIC |
| 120-3331 | VACUUM SYSTEM CONTROL |
| 120-3332 | TRAP BAKEOUT CONTROL |
| 120-3314 | MIRROR BRACKET |
| 120-3315 | MIRROR PIVOT |
| 120-3316 | MIRROR MOUNT YOKE |
| 120-3317 | PORT COVER, MIRROR |
| 120-3318 | ROTATION KNOB & SHAFT |
| 120-3319 | MIRROR WORKING DIMENSIONS |
| 120-3320 | ASSEMBLY, MIRROR MOUNT |
| 120-3340 | LAYOUT, Ca OVEN |
| 120-3341 | 12.2 cc Ca OVEN |
| 120-3342 | CONICAL RESERVOIR PLUG |
| 120-3343 | CRADLE, Ca OVEN |

APPENDIX B: CURRENT-VOLTAGE TRANSDUCER

The purpose of this unit is to provide very fast current to voltage conversion and gain for the interaction region electrodes and Faraday cup. It consists of an operational amplifier used in the current to voltage mode, an input protection circuit to protect the amplifier from high voltage charges on the electrodes, gain switching, an output limiter to avoid saturation, a current buffer to maintain high bandwidth, a double-ended window detector to sense voltage excursions greater than ± 10 V and drive an overload indicator lamp, and a $\times 10$ amplifier with provision for adjustable offset. An input switching network is self-evident from the schematic (SK 120-3327).

The current converter consists of the closed loop containing the op amp, a buffer, and the variable gain network. The latter contains two gain switching modes. The first (outer control knob, S_1) controls the feedback resistor R_f . This is the most stable mode for use with high gains, but is accompanied by reduced bandwidth as determined by the RC time constant of the feedback resistor and stray capacitance. The second gain switching mode (inner knob, S_2) selects a voltage divider tap that multiplies the effective value of R_f by the factor $(R_1 + R_2)/R_2$. This mode doesn't affect bandwidth, but thermal drifts and offset voltages increase proportionally to the gain setting of S_2 .

The buffer is provided to drive the parallel loads of the voltage divider tap networks, which would otherwise limit the bandwidth of the operational amplifier because of the increased current drain.

The time required for the current conversion circuit to recover from saturation is excessive, so an output overload limiter consisting of zener diodes and low leakage diodes is included to prevent this from occurring.

The output of the current converter has been arranged so that it is no more than 1 V. The reasons for this are (1) lower power dissipation to reduce thermal drifts, (2) high slew rate for higher bandwidth, and (3) lower offset drift. This is followed by a high impedance, gain-of-ten amplifier as the

last stage. An output overload light, driven by a double-ended window comparator, comes on when the output exceeds ± 10 V.

The ± 12 V power for this unit is taken from the NIM-bin ± 24 V bus through two 723C regulators. The voltage may be trimmed by adjusting two potentiometers. The $10^9 \Omega$ resistors should not be touched, as this would induce gross errors due to leakage currents.

APPENDIX C: LOGIC CONTROL UNIT

An explanation of the operation of this circuit is best begun by a discussion of the SYNC MODE switch S_1 (see SK 120-3328). In the "OSC" position, beam phasing is controlled either by the logic unit's internal clock or by a signal derived from the time-base signal of the boxcar integrator. Oscillator selection is made by switch S_2 , which provides a signal to the appropriate one of two AND gates in module I_4 . Both AND outputs are applied to an OR gate in I_3 , which in turn controls the time-base flip-flop in I_5 . (The other flip-flop in I_5 is used as a latch in the data accumulate system.)

In the "MAN" mode position, both I_4 gates are held low (closed) through 500Ω resistors, and hence there is no toggling of the time-base flip-flop. In this mode, switch S_3 controls the two remaining AND gates in I_4 , which in turn either $\overline{\text{SET}}$ or $\overline{\text{RESET}}$ the direct input terminals of the I_5 flip-flop. Both of the latter two gates are open in the OSC mode, causing a common "high" to appear at the $\overline{\text{SET}}$ and $\overline{\text{RESET}}$ of I_5 . Since only a "low" state overrides the flip-flop toggle function, the manual control is inoperative under these conditions.

The internal clock consists of transistors T_1 , T_2 and T_3 and the one-shot multivibrator I_{11} . T_1 is a current source whose amplitude is controlled by a "trimpot" in its emitter circuit. This serves to control the clock period. The current charges a capacitor, causing a ramp to appear at the emitter of unijunction T_2 . When the unijunction fires, it turns on T_3 , causing a fast, negative spike from its collector to couple (through 330 pf) to the input of I_{11} . The one-shot, thus triggered, produces a 500 nsec clock pulse (duration determined by its external timing capacitor), which is the signal applied to the AND gate of I_4 .

The external oscillator signal is derived from a 10 V negative ramp produced by the boxcar integrator. The ramp is shaped into a clock pulse as follows: The ramp (suitably attenuated by a divider pair) is applied to the positive input of a fast comparator I_8 . The I_8 output is clamped "low" except when the ramp voltage level is positive. This occurs during a small portion of the boxcar ramp, and during that time the comparator produces a "high" output which is the clock signal for the external oscillator AND gate in I_4 . Since the time-base flip-flop in I_5 switches state with every clock pulse, its output has half the periodicity of the boxcar integrator time-base ramp. The $3k\Omega$ resistor at I_8 inhibits oscillation and false triggering of the comparator.

The beam phase, as determined by the conjugate outputs Q and \overline{Q} of the time-base flip-flop in I_5 , is indicated by panel lights. These are driven by modules I_1 and I_2 . The chopper itself (see Appendix D) is driven by \overline{Q} via an AND gate in I_7 .

Scaler and timer gating signals are derived as follows: The 20 V boxcar integrator gate signal, attenuated to logic levels by a voltage divider, is applied to both channels of dual AND gate module I_6 . One of these gates is controlled by Q , the other by \overline{Q} . Hence, the gate signals are transmitted alternately through the two gates. These alternate gate signals are applied to the two scaler channels. Transistors T_6 and T_7 are inverters to convert the signals to the fast, negative logic levels used in the SEN 312 scaler. The attenuated boxcar gate is also applied to the NIM-module timer via the other AND gate of I_7 . This gate is part of a "data accumulate" system which is discussed next.

The "data accumulate" system is provided to assure that the scalers and timer are started and stopped simultaneously. System starting is triggered by a push-button switch S_4 , and stopping is triggered either by a second actuation of the same switch or upon acquisition of a predetermined

number of counts in either scaler channel. These last are applied to the EXT stop connector. The second flip-flop of I_5 controls the data accumulate functions, and is triggered, through an OR gate in I_3 , by one of the above methods.

When the Q output of the data accumulate flip-flop is "high", T_5 turns on and drives the indicating lamp. Q also opens the AND gate in I_7 , allowing gate pulses to be transmitted to the timer for accumulation. In this state, \overline{Q} is "low" and T_4 is off. When the flip-flop in I_5 is triggered to the other state, Q becomes "low", so the lamp goes off and the timer gate closes. In this state, \overline{Q} is "high" and T_4 conducts. This causes its collector circuit to be shunted to near ground potential. This circuit is connected to the standard "gate" channel of NIM systems (pin 36) and serves to inhibit the T101 discriminator. (It must be in the GATED mode.)

The logic Control Unit also incorporates a dual operational amplifier, I_9 , wired to give X 10 gain for general use. The first half is used in the "follower" configuration to obtain extremely high input impedance ($\approx 10^8 \Omega$). The second half is used in the inverting configuration, with gain determined by the $1k \Omega$ and $10k \Omega$ feedback resistors. The rise time is 10^{-9} sec, and the output impedance 1Ω . Output offset is adjustable by a trimpot.

Power to drive the logic system is derived from the ± 12 V supply of the NIM-bin. A Helipot regulator provides 5 V (adjusted by a trimpot) for logic level control. A 1.9Ω resistor causes crossover to current limited operation at 300 mA. This protects against excessive load (e.g., accidental short circuits).

APPENDIX D: HIGH VOLTAGE CHOPPER

The heart of the high voltage modulating circuit consists of a two tube circuit wherein the tubes are made to conduct alternately by suitable control grid signals (see Section 2.9.3 and Figure 23 of the text). The high voltage signal is obtained from the cathode of one of the tubes. What remains to be described is the production of the properly phased grid wave-forms.

The two grid wave-forms are conjugate ac signals, so only one system will be described. The wave-form potentials are derived, in each case, from floating +30 V and -50 V power supplies which are alternately applied to the control grid by a two-transistor switch circuit. The switching signal is provided by either a Q or \bar{Q} output of a flip-flop via a driver module. The flip-flop, in turn, is controlled by "direct set" and "direct reset" signals derived from the Logic Control Unit and coupled to the high voltage circuitry through pulse transformers.

A prototype of this unit had problems due to spurious trigger signals induced by high-voltage arcs. This caused the chopper phase to shift by 180° at random intervals. To avoid this problem, a 10 MHz oscillator was incorporated into the control circuitry in such a way that it continuously "sets" or "resets" the flip-flop to its desired operating mode. The oscillator pulses are gated to the "set" connection during half the time-base wave-form, and to the "reset" connection during the other half. In this way spurious triggering of the flip-flop is corrected within one period of the high frequency oscillator, and the tubes are forced to conduct and shut off in the desired alternating sequence. The oscillator is a one-shot multivibrator with an inverter feedback loop, and its frequency is set by a trimpot. The frequency has been adjusted for optimum coupling to the pulse transformers and should not be changed.

Circuit operation is as follows: A clock signal K is received from the Logic Control Unit. A conjugate signal \bar{K} is produced by an inverting OR

gate. These two signals are applied to the inputs of a dual AND gate, each of which also receives the oscillator signal. The oscillator signal therefore appears alternately at each gate output, and these in turn are connected to a pair of pulse isolation transformers that couple to the "set" and "reset" flip-flop connections mentioned above. Thus, when K is "high" one pulse transformer couples the oscillator signal to the "set" connection and causes the flip-flop output to go "high". When K is "low", \bar{K} is "high" and its pulse transformer couples the oscillator signal to the "reset" connection, causing the flip-flop output to go "low". The conjugate timing is used for the other tube grid wave-form.

There are seven dc voltage supplies and regulators within the chopper. Two groups of three are identical, and provide potentials, referenced to the voltage divider taps, for the grid wave-form and integrated circuit power. The seventh provides +5 V power for those integrated circuits that operate at ground potential instead of floating. Filament power and ac power for all the voltage supplies is provided by a multiply tapped isolation transformer.

NEW TECHNOLOGY APPENDIX

An Apparatus to Study Collisions of Ionized and Neutral Particles with Gases at Meteoric Velocities

The apparatus is described on pp. 6-82 of this report. Its main features are as follows:

1. Beams of mass-analyzed ions and neutral particles can be produced from any gas and most elements.
2. Beam energy is variable from 10eV to 3000eV corresponding to particle velocities from about 10^6 to 10^7 cm/sec.
3. Means are provided for colliding the beams with low pressure (~ 1 torr) gas targets.
4. Collision induced spectra can be recorded from 2200 Å to 8000 Å.
5. Positive and negative charge produced by the collisions can be measured.
6. Emission cross-sections can be determined from measurements of:
 - (a) target gas pressure and temperature,
 - (b) ion or neutral beam flux, and
 - (c) absolute intensities of spectral lines with wavelengths from 2500 Å to 8000 Å.
7. With ion beams the smallest measurable emission cross-sections are about 10^{-19} cm² at the lowest beam energy and about 10^{-21} cm² at the highest beam energy.

This combination of features is thought to be unique and to represent an improvement over similar apparatus of this type.